Tip enhanced Raman spectroscopy and cantilever sensors for studying Li-ion battery materials

Thesis by

Connor Aiken

Department of Physics
McGill University
Montreal, Canada

August 2017

A thesis submitted to McGill University in partial fulfillment of the requirements of the degree of

Master of Science

©Connor Aiken 2017

Acknowledgements

I would like to thank my supervisor, Prof. Peter Grutter for all of the guidance and support throughout the entirety of my M.Sc. project. Prof. Grutter's depth and breadth of knowledge were invaluable over the course of my research, as well as his assistance in facilitating the collaborations that enabled this project.

The assistance of Yoichi Miyhara, Robert Gagnon and John Smeros was critical in understanding, operating and maintaining the instrumentation used throughout this research, as well as providing many options to the solve the problems that were encountered. To David Speller, for allowing the use of the McGill Architecture Department's laser cutter.

I would like to acknowledge the collaboration with Dr. Andreas Ruediger, Dr. Gitanjali Kolhatkar and Clarick Jiawei Zhang at Institut national de la recherche scientifique - Énergie, Matériaux et Télécommunications. I must convey thanks for allowing me the use of their tip enhanced Raman microscope and displaying patience to complete long experiments with me. I would also like to acknowledge the collaboration with the Energy Storage and Conversion research group at the Institut de Recherche d'Hydro Québec. They provided both valuable advice on the direction of the project, as well as the entirety of the battery sample materials.

All members of the scanning probe research group deserve thanks for their support, assistance and input throughout the project. Even when the trials of research seem overwhelming, having positive and helpful individuals working around you can give you the extra push to keep moving forward. In particular, special thanks to Tyler Enright and Aaron Mascaro for providing valuable advice and feedback during weekly subgroup meetings. Also, thanks to Antoine Roy-Gobeil for his services in translating my abstract.

I would like acknowledge the funding received from Prof. Grutter's research funds and from NSERC through the Canada Graduate Scholarships - Masters program.

Finally, I would like to thank my girlfriend, Patricia Oliver, for providing support and encouragement throughout my M.Sc. work.

Contribution of Co-authors

Chapters 1, 2 and 3 provide an introduction into the motivation, physics and experimental methods of this thesis. All information in these sections was compiled by Connor Aiken.

Chapter 4 details studies using Raman spectroscopy. Connor Aiken prepared the polished $LiFePO_4$ sample and the nanoplatelets on gold sample. Aaron Mascaro, of McGill University prepared the polished, partially delithiated $LiFePO_4$ sample. Synthesis of these materials was completed by Andrea Paolella and Vincent Gariepy at Institut de Recherche d'Hydro Québec. The Raman microscope was operated by Gitanjali Kolhatkar of Institut national de la recherche scientifique - Énergie, Matériaux et Télécommunications, under the direction of Connor Aiken. When tip enhanced Raman experiments were conducted, Clarick Jiawei Zhang, also of Institut national de la recherche scientifique - Énergie, Matériaux et Télécommunications, fabricated the tips. Characterization of nanoplatelet samples was performed by Connor Aiken. All data analysis was performed by Connor Aiken

Chapter 5 details the development of cantilever sensors. Andrea Paolella, of Institut de Recherche d'Hydro Québec, synthesized the $Li[Ni_{1/3}Mn_{1/3}Co_{1/3}]O_2$ and $LiFePO_4$ powders used during sample preparation. Robert Gagnon, of McGill University, operated the sputtering system. Tyler Enright, of McGill University, operated the aluminum evaporator. All other sample preparation, including cutting, battery slurry mixing, and coating with battery material was done by Connor Aiken. All deflection, electrochemical and spring constant experiments were performed by Connor Aiken. All data analysis was performed by Connor Aiken.

Chapter 6 is the concluding remarks of the work. Conclusion was assembled by Connor Aiken.

Abstract

Current battery technologies must be improved if they are to be used as the energy storage solution that enables the transition to renewable global energy production. The study of batteries, in particular, lithium ion batteries, requires new or previously unutilized techniques that can provide fundamental understanding of the phenomena that affect performance. Among these phenomena, a solid electrolyte interphase (SEI) develops on the surface of the battery electrodes that can result in reduced energy storage capacity and power delivery, and increased degradation. Understanding the SEI requires a dynamic understanding of its chemistry and structure, and how those affect battery performance.

Combined tip-enhanced Raman spectroscopy (TERS) and atomic force microscopy (AFM), as well as cantilever sensing were investigated as new measurement techniques for the study of the solid electrolyte interphase formation in lithium ion batteries. Confocal Raman microscopy on $LiFePO_4$ and partially delithiated Li_xFePO_4 was able to reproduce literature results and detect spatial variation on the delithiated sample with $0.5\,\mu m$ resolution. The presence of two distinct phases were observed, with spectra suggesting that the phases possibly contained different lithium concentrations. Despite success with confocal Raman microscopy experiments, advancement to TERS experiments did not prove successful. The gold tips required for field enhancement cannot currently be fabricated and utilized for AFM while still providing reliable excitation of a localized surface plasmon resonance and reliable Raman scattering.

Cantilever sensors were designed to mimic a commercial battery electrode; that is a battery electrode cantilever. The design implemented a mica substrate, a metal thin film current collector and an active material layer. An electrochemical chamber was designed, with optical access to enable combined electrochemical-surface stress measurements on the battery electrode cantilevers. The chamber was made air-tight to enable use of air-sensitive battery materials for future tests. Tests in aqueous electrolytes showed that reaction and/or delamination of the metallic current collector layer compromised the conductivity of the cantilevers before lithium could be removed from the active materials.

Résumé

La transition vers une production globale d'énergie par des sources renouvelables, plutôt que par la combustion de matières fossiles, est nécessaire pour prévenir des dommages irréparables l'environnement. La production d'énergie à partir de sources renouvelables nécessite un système de stockage d'énergie pour pallier aux intermittences de service. Les technologies de batterie actuelles doivent toutefois être améliorées si elles veulent devenir cette solution de stockage d'énergie qui permet la transition vers une production globale d'énergie renouvelable. Les recherches sur les batteries, en particulier sur les batteries lithium-ion, nécessitent de nouvelles techniques de mesures pour fournir une compréhension fondamentale des phénomènes qui affectent leur performance.

La combinaison de la spectroscopie Raman exaltée par effet de pointe (TERS) et la microscopie à force atomique (MFA), ainsi que la détection par cantilever ont été utilisées comme techniques de mesure pour l'étude de l'interphase solide électrolyte formée dans les batteries lithium-ion. La microscopie Raman confocale sur du $LiFePO_4$ et du partiellement délithié Li_xFePO_4 a permis de reproduire des résultats de la littérature et de détecter une variation spatiale sur l'échantillon délithié avec une résolution de $0.5\,\mu m$. La présence de deux phases distinctes a été observée, avec des spectres suggérant que ces phases contiennent des concentrations différentes de lithium. Malgré le succès des expériences de microscopie Raman confocale, nos expériences de TERS ne sont pas avérées aussi fructueuses. Les pointes d'or nécessaires pour exalter le champ proche ne peuvent présentement pas être fabriquées et utilisées pour la MFA. Celles-ci ne peuvent pas garantir simultanément une excitation des résonances locales des plasmons de surfaces ainsi qu'une diffusion Raman fiable.

La détection par cantilever a été conçue pour imiter une électrode de batterie commerciale. Le système consiste d'un substrat de mica, d'une couche métallique mince comme collecteur, d'une couche de matériel actif et du cantilever comme électrode. Une cellule électrochimique a été conçue avec un accès optique pour permettre de combiner des mesures d'électrochimies et des mesures de tension de surface sur le canitlever. La chambre a été conçue pour être hermétique à l'air permettant ainsi l'étude de matériaux sensibles à l'atmosphère. Des tests dans un électrolyte aqueux montrent que la réaction et/ou la délamination de la couche métallique compromet la conductivité du cantilever avant que le lithium ne puisse être retiré de la couche de matériel actif.

Contents

Chapter 1

Introduction

1.1 Motivation

The goal of this work is to investigate new characterization techniques that will produce fundamental understanding of and subsequent improvement to the active materials that comprise lithium ion batteries. Energy storage in batteries, along with energy production by renewable, sustainable means, is part of a solution proposed to halt the environmental and socio-economic problems with current energy production from combustible, fossil fuel sources.

Growing concentrations of atmospheric CO_2 contribute to global warming, causing the destruction of the planetary ecosystem. Estimates predict that to meet the energy demands of the global community, while maintaining atmospheric CO_2 levels below acceptable levels, 15 TW and 30 TW of power will be required from carbon neutral sources, by deadlines of the years 2050 and 2100, respectively [1]. Failure to meet these targets will only increase the demand on renewable energy production and the urgency of the shift to sustainable energy practices [1]. As mentioned above, batteries are an energy storage solution that can enable the production of energy by renewable means. Development of a high performing battery is therefore essential and urgent.

1.1.1 Renewable energy production

Energy production that does not contribute to the growing atmospheric concentration of CO_2 and other so-called greenhouse gases has been given a number of terms. These include sustainable, renewable, carbon neutral and environmentally friendly. These terms tend to apply directly to the processes in which energy is captured and converted a usable form, typically electricity. Generally, this is the collection of energy from a natural phenomenon, such as radiant solar energy or kinetic energy of air (wind) and water (rivers, waterfalls, tides). Collection of such energy does not immediately harm the environment with dangerous emissions. One of the challenges, however, with using renewable energy sources is inconsistent, or at the very least periodic availability of power.

Figure 1.1 shows the variation in the availability of a few renewable energy sources. Figure 1.1A shows that solar intensity, a limiting factor in the magnitude of

solar power that can produced, fluctuates seasonally. On the time scale of days, the availability of sunlight is easily understood. Approximately half of the day is spent in light, while the other half is spent in darkness, due to the rotation of the Earth about its geographical axis. Furthermore, cloudy weather, possible on any day, can also restrict the incident solar intensity that reaches the planet surface. When the sun is unable to deliver full radiant intensity to the surface, the potential for producing solar energy suffers, whether it be due to seasonal, daily or weather constraints.

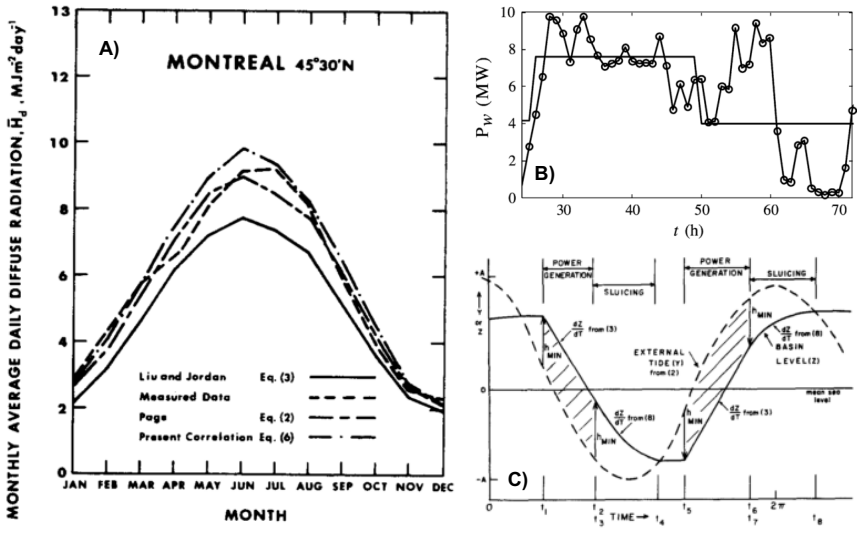

FIGURE 1.1: Typical variation of power delivered by a variety of renewable sources. A) Variation in solar radiation intensity in Montreal based on averages from 1964 – 1975, from Ref. [2], which is a limiting factor in solar power production. B) Actual wind power production in Norway, over a 72 hour interval, shown by open circles, from Ref. [3]. C) Schematic of two-way tidal power generation over a single tidal cycle, from Ref. [4]

Figure 1.1B shows a sample of wind power produced over a 72-hour interval. It is unclear if this is a day with a particularly large amount of wind, but again, this is a weather-related phenomenon, and some unpredictability should be expected. Small scale fluctuations of 10-20% in power output occur over 2-4 hours, while changes of $\tilde{1}00\%$ occur in intervals as fast as 10 hours. Power collected from the wind is therefore very intermittent and unreliable. Figure 1.1C shows a schematic of tidal flow over one cycle, indicating regimes of power generation in dashed regions. The flow of the tides is predictable, as there are two ebb/flow cycles every day. However, even if both the ebb and flow are used to generate power (two-way tidal power), there are many points in the tidal cycle where power is not being generated. Thus, despite being reliable, tidal power production is intermittent like solar and wind based power sources. This intermittent characteristic is common to many means of renewable power production.

1.1.2 Grid energy storage

Given that the production of renewable power is intermittent and often unpredictable, the challenge is how to integrate sources of renewable power with energy consumers such that the demands of the consumers are adequately met by the supply from renewable sources. Figure 1.2 shows a graph of the typical load on an electrical grid during a 24-hour period. Normally, larger demands are placed on the grid during waking hours, peaking in the evening, and power demands are increased during the winter compared to summer [5]. From the previous section, it was discussed that the greatest solar power is produced in the summer months during the day time. Clearly this is a challenge when trying to meet the highest demands shown in Figure 1.2, of a winter evening. Furthermore, the intermittent nature of tidal power and the unpredictability of wind power make it difficult to supply the steady-state demand placed on the grid during the majority of the waking hours. The solution is to collect energy when it is available and store any excess that is not needed by the grid. When the grid demands exceed the capacity of the renewable supply, for whatever reason, the energy stores can be drawn upon to supply power to make up the difference. This storage is referred to as grid energy storage, which enables the process of load leveling or smoothing.

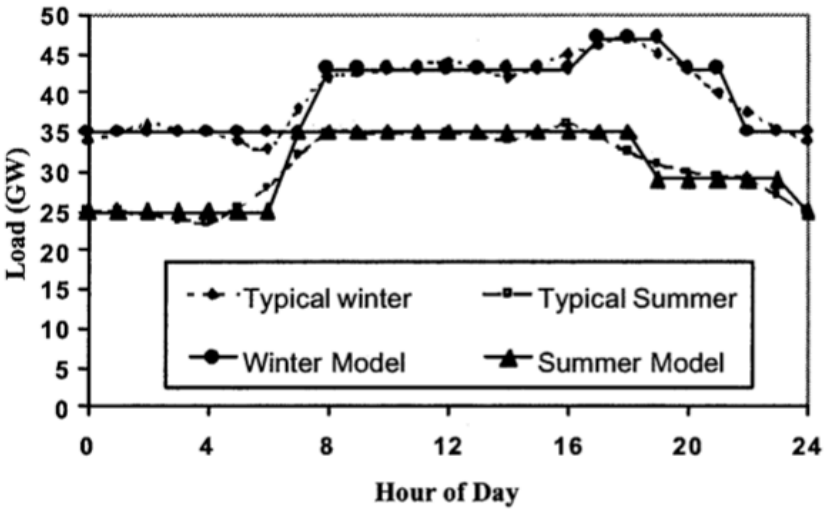

FIGURE 1.2: Schematic of typical electrical grid load over a day in both summer and winter seasons [5].

Figure 1.3 shows a possible scheme for the integration of solar energy production into the existing grid, with storage capacity for excess solar energy [6]. The two curves indicate electricity generated and the consumption from users. During the night hours, electricity from solar production cannot occur, therefore, the demands of the users must be met by the traditional sources (nuclear, fossil fuels, etc.). As the sun dawns, solar electricity production increases, reducing the draw from the grid. Eventually the solar electricity production exceeds the consumer demand. At this

point, region (2) in Figure 1.3, consumers are being completely supplied by solar energy. Any excess energy produced can be stored for later consumption, up to the maximum capacity of the storage system. As the sun sets, the amount of solar energy produced can no longer entirely supply the consumer demands. The energy that was previously stored can be delivered to make up this difference, until the storage capacity is depleted. Electricity draw then switches back to the grid and the cycle repeats the next day. In this hypothetical scheme, there is a glaring, two-fold problem caused by the limited storage capacity: there is wasted solar energy that cannot be stored (region (3) in Figure 1.3) and the energy that is stored cannot meet the demands of consumers during the entire time that solar energy production is off-line (the night time). The problem is exacerbated during periods when availability of renewable energy is reduced, as discussed in the previous section.

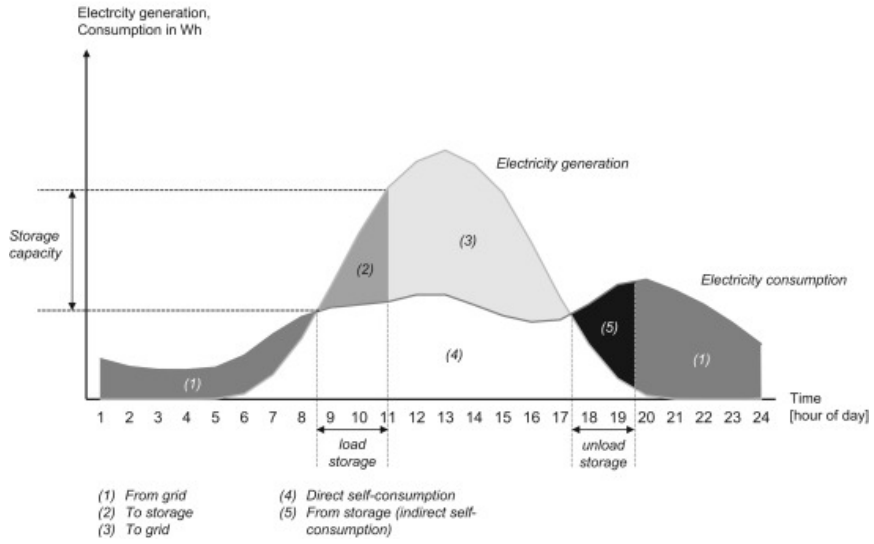

FIGURE 1.3: Schematic of production and consumption of renewably sourced electricity with a storage system. The amount of solar generated electricity is indicated in the light grey line, while consumption is shown with a darker grey line. The meaning of each shaded region is indicated in the legend, and explained in greater detail in the text, from Ref. [6].

Figure 1.4 compares a variety of energy storage technologies based on their rated power and how long that power can be delivered. The duration over which the rated power can be delivered is essentially a capacity. The technologies that have the highest power densities and largest capacities are pumped hydro and compressed air storage. These are related in that they are mechanical means of storage. Water is pumped to elevated heights in a reservoir, and air is pumped to greater pressure in a compression vessel. Release of the water or compressed air is used to operate a turbine and generate electricity. Due to the simplicity of these technologies and the large, sustained power that can be provided, they account for almost the entirety of

the global storage capacity [7]. They do, however, require considerable infrastructure and space. They are also less useful in applications that require less power but faster response times, such as load shifting, peak shaving, voltage and frequency control [5, 7].

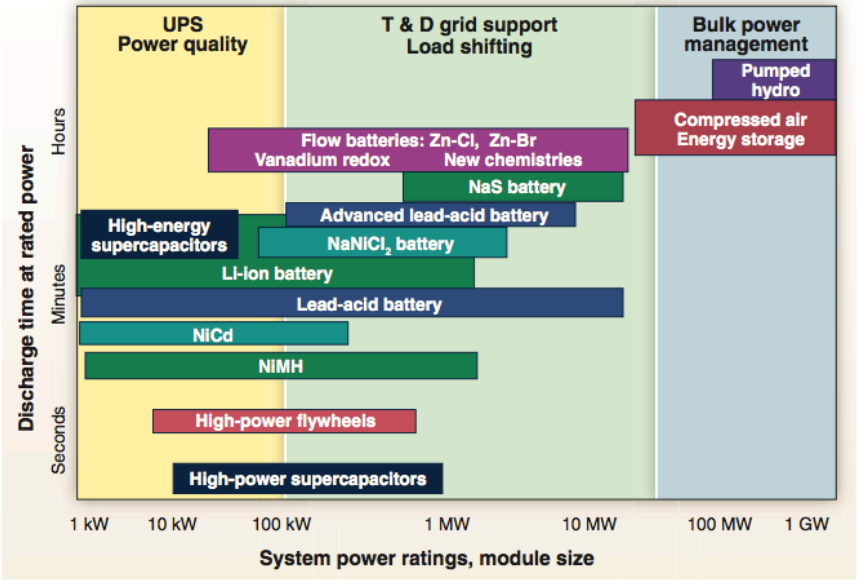

FIGURE 1.4: Comparison of rated power and duration for which that power can be delivered, for a variety of energy storage solutions. The plot is divided into three regions, based on rated power, indicating the role of the technology in a grid storage system, from Ref. [7].

As mentioned in section 1.1.1, power provided by renewable sources is unreliable and intermittent. The mechanical means of energy storage discussed above can accommodate the absence of power from a renewable source, if the absence is predictable. Other technologies, however, are required to provide faster responses to accommodate the unpredictable nature of renewable power production. The middle of Figure 1.4 is populated by various battery technologies. These can provide modest powers and capacities, with much faster response times than pumped hydro or compressed air [7]. Amongst these battery technologies, Li-ion battery technology is a very good candidate to provide storage for a renewable power production scheme. It is a mature enough technology that can be implemented on a time scale that aligns with the proposed deadlines by which renewable energy production must become the global norm. Li-ion batteries are compact and modular, which means a large, wide-spread capacity can be achieved by extensive distribution, possibly on the consumer end of the power grid. They are also quite high efficiency [7]. The main drawbacks, however, are that the discharge power of Li-ion batteries still cannot compare to that of mechanical means of energy storage. They also suffer from a finite lifetime. After a given number of charge-discharge cycles, their capacity is eventually reduced below a threshold where they must be replaced [7]. This adds cost and reduces performance of a potential storage system. If Li-ion batteries are to

be the energy storage technology that facilitates the transition to renewable energy production, these shortcomings must be improved.

1.1.3 Portable energy storage for electric vehicles

As has been discussed, energy production that supplies the electricity to the world's population can fully transition from fossil fuels to renewable sources given a suitable energy storage system. Another major application of fossil fuel combustion is in the engines that power vehicles and machinery throughout the world. Electrifying vehicles (and machinery) will act to sustain the environment in a similar manner as switching to renewable energy generation. An electrified vehicle is one with an electric motor and an electrical energy storage device (a battery) that can be recharged from the grid. Obviously, this is only a positive, long-term solution if the electrical grid is sourced from renewable energy.

A current paradigm shift in the automotive industry is underway, but only in its infancy. As of 2017, battery electric vehicles (BEVs) are in production by major North American, European and Asian automotive manufacturers, including Chevrolet, Ford, Nissan, Toyota and Volkswagen. Tesla Motors has even gained recognition for only offering electric vehicles, from performance cars to pickup trucks. BEVs do not produce motor/exhaust noise or any emissions, and offer smoother acceleration compared to a typical vehicle. However, they are expensive, have limited range and take considerable time to recharge [8]. The main cause of these drawbacks is the battery that powers the BEV. Specifically, it's energy and power densities are limitations on capacity and charging/discharging rate respectively. Figure 1.5 shows a Ragone plot of a variety of battery technologies, comparing their energy and power per unit mass. Lithium ion batteries currently constitute the highest performing battery technology across both of these metrics, while also possessing strong performance in safety and lifetime. Consumer behaviour is often dictated by convenience and cost, rather than ethics regarding the environment.

1.2 Outline

This thesis is comprised of content from two separate projects, both with the same goal of utilizing new techniques for studying lithium ion batteries. The first technique is combined tip-enhanced Raman spectroscopy and atomic force microscopy, while the second is cantilever sensors. Chapter 2 will discuss the operation of lithium ion batteries and review the body of work that has been done already by the research community. The principles behind Raman spectroscopy, atomic force microscopy and cantilever sensing, and any previous application to lithium ion batteries is also presented. Chapter 3 contains details of the experimental methods and instrumentation used throughout this thesis. Chapter 4 presents the work done towards achieving tip-enhanced Raman spectroscopy on battery materials. Chapter 5 presents the

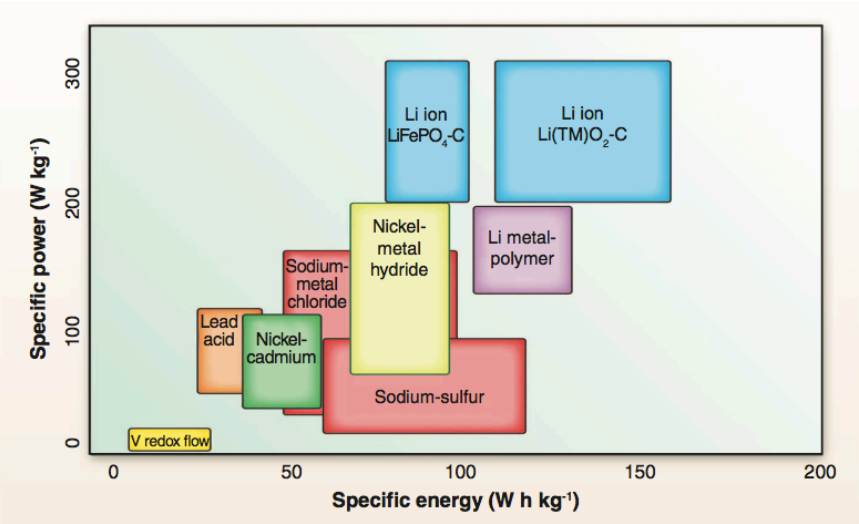

FIGURE 1.5: Ragone chart comparing various rechargeable battery technologies with potential application for grid and vehicular energy storage, from Ref. [7].

work done in developing cantilever sensors that incorporate lithium ion battery active material. Chapter 6 contains the conclusions of this work and the outlook for future work.

Chapter 2

Background information and theory

2.1 Li-ion batteries

2.1.1 Basic operation

A battery is a device that stores energy electrochemically. A pair of electrodes serve as hosts for a charged species while the difference in the electrochemical potential of the charged species in each electrode is used to establish an electrical potential difference across the battery. When the battery is connected across a load, positively charged ions can move from the high potential electrode to the low potential electrode, thus producing an ionic current internally, and a corresponding electrical current through the load. In a lithium ion (Li-ion) battery, the charged species that enables energy storage is the lithium ion, Li^+. Li-ion batteries typically operate with intercalation electrodes. Intercalation compounds are layered structures that can reversibly accept small molecules and ions between their layers with minimal or no change to the host structure. The process of inserting and removing species between the layers is known as intercalation and deintercalation respectively [9]. An easily understood intercalation compound is graphite. Graphite can intercalate many species between its graphene layers, including lithium ions. For this reason, graphite is one of the most common electrode materials used in Li-ion batteries.

The electrochemical potential of lithium in graphite approaches that of metallic lithium as it stores lithium ions at increasing concentration [9]. This means that graphite is suited to accept Li-ions from a compound where they exist in a lower energy state. Such intercalation compounds exist, the most common in use and one of the earliest in discovery is $LiCoO_2$ [10]. In $LiCoO_2$ (LCO), lithium ions reside between layers of cobalt-oxygen octahedra. Lithium ions exist in a lower energy state when in LCO than in graphite [9, 10], which establishes a means of energy storage. Energy is invested to move the lithium ions from a low energy electrode to a high energy electrode. That energy is returned when the ions move back to the low energy electrode.

Because batteries are used, measured and controlled by electrical potentials and currents, it is useful to consider the operation of a Li-ion battery from the perspective

of both ions and electrons. Electrical potential is essentially proportional to the electrochemical potential, with the proportionality constant being the charge. Because electrons and lithium ions carry opposite charges, the electrode discussed above as a low energy electrode for lithium ions is actually the electrode with higher, or more positive, electrical potential. Similarly, the high energy electrode is the electrode with the lower, or more negative electrical potential. The convention is to refer to these as the positive and negative electrodes respectively. The canonical example of a Li-ion battery, as introduced above, is LCO as the positive electrode and graphite as the negative electrode.

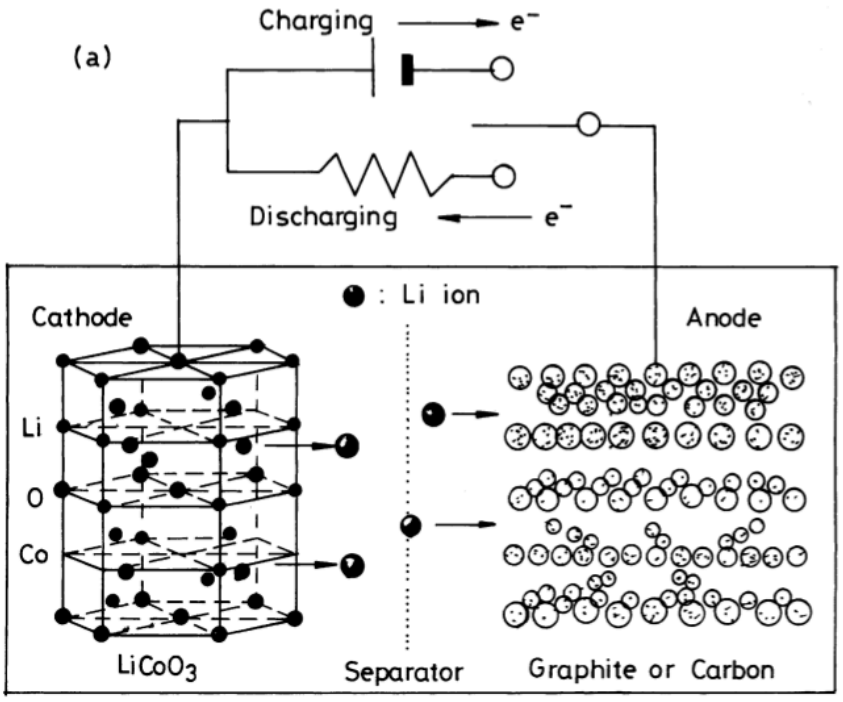

FIGURE 2.1: A simplified schematic of the charging and discharging processes in a lithium ion battery. The canonical example of $LiCoO_2$ positive electrode and graphite negative electrode is used. Taken from Ref. [9].

Figure 2.1 shows a schematic of the operation of a Li-ion battery. Initially, in the discharged state, the positive electrode is full of lithium. Every possible site between the Co-O layers is occupied by lithium. A charging potential is applied across the battery. The electrons that bond the lithium ions to the surrounding lattice flow from the positive electrode in response to this potential, through the external circuitry and into the negative electrode. Without the electronic bond to the lattice, lithium ions deintercalate from the positive electrode, flow through the lithium ion conducting electrolyte, intercalate in the negative electrode, and recombine with the electrons. Assuming the capacity to store lithium ions is the same in both the positive and negative electrode, the charging current will continue to flow and the potential of the battery will increase until the positive electrode is completely void of lithium,

or conversely the negative electrode is full. Next, if a load is connected to the battery, the flow of electrons and Li-ions will reverse. Li-ions will deintercalate from the negative electrode and return to the positive electrode, while electrons will flow through the load, performing work as they also return to the positive electrode.

2.1.2 Solid electrolyte interphase

In the previous section, the operation of a lithium ion battery is presented as an idealized process. In practice, there are a number of inefficiencies and limitations that prevent operation exactly as described above. Of particular interest is the development of what is referred to as a solid electrolyte interphase (SEI) [11]. During charging, both the positive and negative electrodes can experience rather extreme potentials. At these high and low potentials, respectively, the electrolyte is thermodynamically unstable [12] and both the salt and solvents will irreversibly react on the electrode surfaces. The products of these reactions form a solid film that resides on the electrode surface, referred to as the solid electrolyte interphase. Figure 2.2 shows a schematic, in a similar design to Figure 2.1, that depicts SEI formation on the negative electrode of a Li-ion battery. This SEI serves as a passivating layer, which prevents continual decomposition of the electrolyte [12].

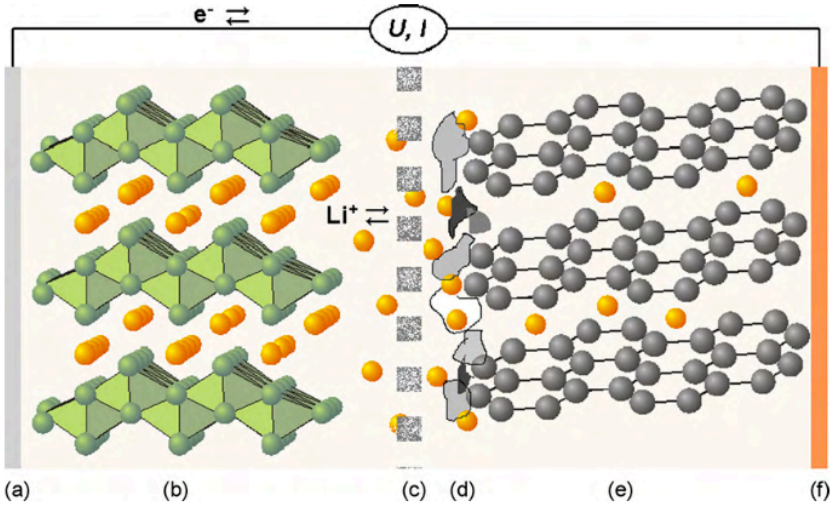

FIGURE 2.2: Schematic of the operation of a lithium ion battery, where a solid electrolyte interphase is present on the negative electrode. Labels are: (a) aluminum current collector for positive electrode; (b) positive electrode material; (c) separator; (d) solid electrolyte interphase; (e) negative electrode material; (f) negative electrode current collector. Taken from Ref. [12].

To be very clear, the formation of the SEI is essential for the function of a lithium ion battery. Otherwise, portions of the electrolyte would be consumed every time the battery is charged and discharged. The reactions that consume the electrolyte and form the SEI also irreversibly consume the charge in the battery, in the form of lithium ions [13–15]. If the passivation of the SEI was not present, the battery would

quickly run out of electrolyte and would no longer have any charge to facilitate energy storage.

However, to quote Verma *et al.*, "Every parameter and property of the SEI significantly affects battery performance. The composition, thickness, morphology, and compactness are a few to name [12]." Many of the ways that the SEI affects battery performance are detrimental. As mentioned above, the reactions that form the SEI consume charge. Because these reactions are irreversible, such charge consumption that is spent during the first charge to form the SEI is referred to as irreversible capacity loss [14]. Furthermore, imperfections or damage to the SEI will expose unpassivated electrode surfaces to the electrolyte, causing further reactions to passivate the exposed areas. These reactions only consume a tiny amount of charge, when compared to the irreversible capacity loss that occurs during initial formation, but this small amount can add up after many charge-discharge cycles. Thus, the SEI can also consume charge in what is referred to as capacity fade [13, 15]. The passivation from the SEI, again if imperfect or damaged, can also cause charge consumption that occurs over time, leading to self-discharge of the battery [15, 16]. To summarize, the SEI can impact the amount of energy that a Li-ion battery can store because its formation consumes lithium during the first cycle. Furthermore, it can contribute to decreased lifetimes over which the battery can store a reasonable amount of charge because it can slowly consume lithium with every cycle and over time.

In addition to consuming charge, the SEI forms a barrier to lithium ion transfer that has been shown to be resistive in nature [17–19]. When a battery has a large internal resistance, such as resistance attributed to the SEI, there is an ohmic potential drop whenever current is being drawn. This reduced potential will cause an apparent decrease in the amount of energy that the battery can store, which can be especially troublesome when operating at large currents. Limitations on the current mean longer charging times and less power that can be supplied. The nature of the SEI has been shown to change at higher temperature, and even become unstable [20–22].

2.1.3 Methods of study

Despite the SEI playing such an incredibly important role in determining Li-ion battery performance it is not particularly well understood, despite receiving a considerable amount of scholarship. This lack of thorough understanding can be attributed to a variety of sources. Firstly, Li-ion battery research has always been driven by industry, while simultaneously competing to keep up with it. John Goodenough discovered LCO as a viable cathode material in 1980 [10], which was the primary discovery unlocking lithium and Li-ion batteries. In little more than a decade, in 1992, Sony had commercialized Li-ion batteries in their portable electronics. Given that products have been on the market that contain Li-ion batteries, there has been strong incentive over the last 25 years to find new electrode materials, electrolyte formulations, coatings, and the like, that improve performance. The challenge of

finding fundamental understanding of how each of these components works, how they interact and why performance improvements occur is much more difficult and is less relevant to businesses trying to sell products with better batteries. Furthermore, the cutting edge of the technology is moving fast enough that any system that is fully studied and understood will inevitably be outdated.

The second reason complete understanding of the SEI is not understood is hinted at in the previous section. The pursuit of high performing batteries has led to increasingly complicated cell chemistries. Modern lithium ion batteries use electrodes with different active materials and different formulations for the active and inactive (binder, conductive diluent) components [23], electrode materials are modified to substitute various atoms [24] and electrodes particles are modified with surface coatings [25]. Electrolytes use a variety of possibly salts, utilize multiple solvents [26] and contain many additives, that despite being added at very small amounts, have profound effects on battery performance [13, 26, 27]. Furthermore, the understanding of the SEI that exists currently indicates that both its morphology and chemistry play a role in cell performance [12, 19] and it is a dynamic structure [28]. Essentially, the phase space that must be studied within a single battery formulation is massive, given the number of variables in play. Furthermore, the response is typically two steps: a change in battery formulation cause a change in SEI structure or chemistry, which in turn affects cell performance. For reasons that will become clear below, it can be much simpler to simply see how the change affects cell performance, omitting the middle step but sacrificing understanding. On top of all this, commercial battery manufacturers and research groups use their own unique combination of electrodes and electrolyte, so it is difficult to compare results and develop collective understanding.

The final reason that SEI understanding is incomplete is that instrumentation and methodology used for studying the SEI is often not capable of directly probing it under *in situ* or *in operando* conditions. Verma *et al*. describe the challenges of SEI characterization in their review. The SEI is very thin and adhered to the surface of the active material, meaning it is difficult to locate the boundary of the film and it cannot be precisely removed from the active material [12]. Figure 2.3 shows an scanning electron micrograph of a graphite electrode before and after SEI formation. The SEI is so thin that the shape and details of the graphite particles are still discernible and clear after the SEI has formed; the only difference is that the surfaces of the particles have a different texture. The SEI is considered to be dynamic and is truly an interphase, in that it behaves in a liquid-like fashion or has liquid components in the region adjacent to the electrolyte [12, 28], meaning it is difficult probe this solid-liquid continuum and any *ex situ* testing tends to lose these liquid phases [12]. Verma et al. also describe how the liquid phases of the SEI and the electrolyte are chemically very similar and can undergo slightly different reaction mechanisms to arrive at the same products, making chemical differentiation difficult [12]. Finally, nearly every component within a Li-ion battery is oxygen and moisture sensitive. This

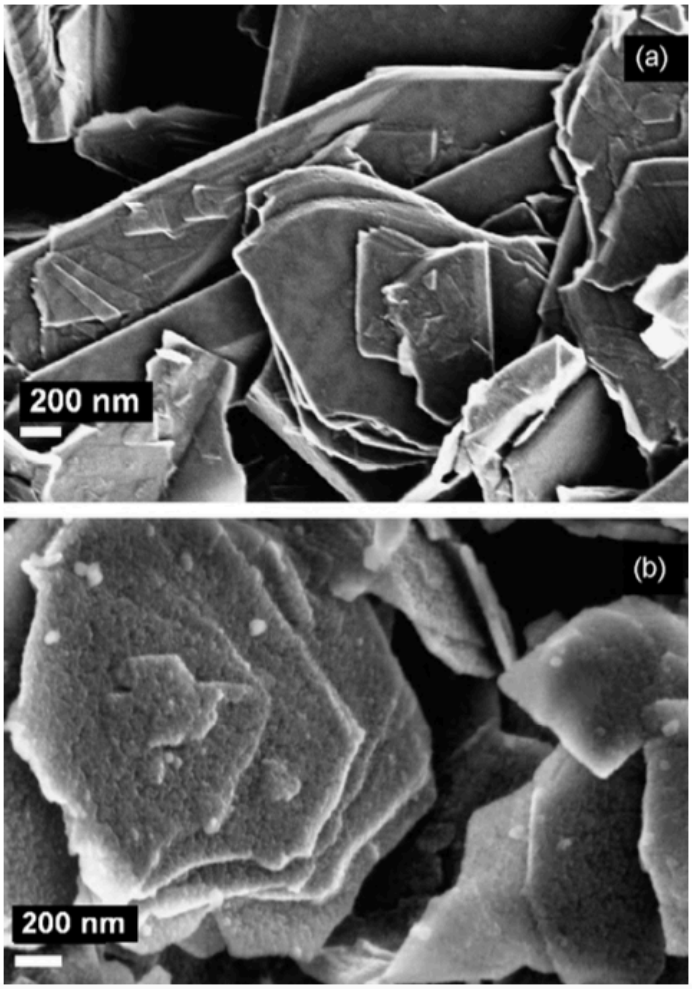

FIGURE 2.3: A scanning electron micrograph of graphite particles (a) before cycling, in pristine condition, without a solid electrolyte interphase and (b) after one cycle, after a solid electrolyte interphase has been formed. Note that the two images are taken at different locations on the electrode. Taken from Ref. [12].

means that any *ex situ* testing requires transfer devices to ensure an electrode from a disassembled battery can travel from the inert atmosphere of a glove box, to the characterization equipment (i.e. scanning electron microscopy, Fourier transform infrared spectrometer) without contamination by atmosphere [12]. A comparison of photoelectron spectroscopy experiments performed on graphite electrodes showed that the resultant spectra are highly dependent on the handling conditions. Accidental exposure to air and even exposure to cleaning solvents can have significant impact on the spectra and thus the chemical species identified [29]. This illustrates the sensitivity of the SEI to external factors and the difficulty in performing *ex situ* analysis on it.

An extensive number of techniques are currently employed to study the SEI. It is difficult to discuss them all and their contribution to the field's understanding of the topic for the reason that is mentioned above: every researcher will measure

differences, whether by choosing a different battery formulation, having slightly different handling procedures or having their batteries undergo different histories. Techniques can be broadly categorized whether they determine composition, morphology, ionic properties, etc., and has been done so clearly and concisely in the review by Verma *et al* [12]. The reader is directed there for the comprehensive list and references.

2.2 Combined tip enhanced Raman spectroscopy and atomic force microscopy

Among the comprehensive techniques listed in the review by Verma *et al*., some are of particular interest because they can be performed *in situ* and therefore accurately probe the SEI. Amalraj and Aurbach review the use *in situ* techniques for the study of Li-ion batteries and classify techniques as either probing surface or bulk properties and utilizing one of spectroscopy, microscopy or diffractometry [30]. Spectroscopy techniques can be used to determine chemical composition; microscopy can image structures on the nano and micro scale; diffraction techniques can determine crystalline order and structuring. The SEI is a surface phenomenon with its function determined by both its composition and structure.

Among the spectroscopy techniques, Amalraj and Aurbach review both Fourier transform infrared (FTIR) spectroscopy and Raman spectroscopy [30]. Examining the FTIR spectra of typical Li-ion battery electrolyte, it is shown to be strongly absorbing at a number of peaks throughout the infrared (IR) spectrum [31]. To perform *in situ* studies, the IR signal must travel through the electrolyte to reach the electrode surface. It is for this very reason that in Amalraj and Aurbach's review, their discussion of FTIR is limited to the attenuated total reflection, internal reflectance, external reflectance and other modes that require highly specialized equipment and battery parts to avoid the IR beam passing through the electrolyte [30]. Raman techniques do not suffer from this strong absorption, because Raman is a weak scattering effect, utilizes visible light to which the electrolyte is mostly transparent and the incident Raman source can be strongly localized.

Among the microscopy techniques, atomic force microscopy (AFM), scanning tunneling microscopy (STM) and scanning electron microscopy (SEM) are listed. AFM does not require electronically conducting samples and is easier to operate in liquid, unlike STM. AFM also does not require vacuum conditions and corresponding solid electrolytes, unlike SEM. The SEI is known to be resistive and best imaged in a liquid environment, lending favour to the use of AFM. Furthermore, AFM with electrochemical cell integration (EC-AFM) is already well established [30, 32–37]. It is also incredibly powerful when combined with complimentary techniques as shown by all the advent of many scanning probe microscopies (SPM) based off of AFM. To *in situ* probe the surface of the Li-ion electrodes and the SEI itself with the

goal of determining morphology and composition of the SEI, it is therefore logical to use combined EC-AFM and Raman spectroscopy.

2.2.1 Raman spectroscopy

Raman scattering was first hypothesized in 1923 by Smekal [38]. In a trio of publications in the first half of 1928, it was experimentally confirmed by C. V. Raman [39–41]. The work would result in Raman receiving the 1930 Nobel Prize in Physics and the phenomenon being identified by his name.

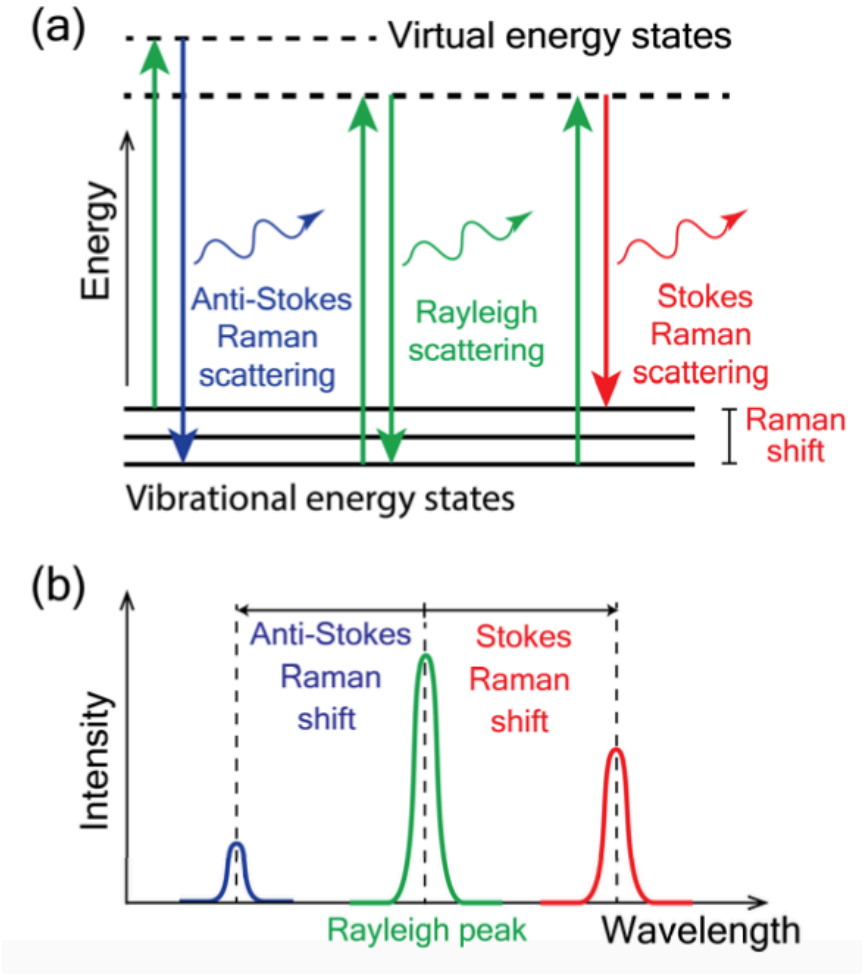

FIGURE 2.4: (a) Jablonski diagram of a two-level vibrational system indicating the energy pathways for both Stokes and anti-Stokes Raman scattered photons, as well as Rayleigh scattered photons. (b) Schematic of spectrum of scattered light for the two-level system described in (a). Taken from Ref. [42].

Raman scattering, or the Raman effect, is a light-matter interaction where optical wavelength light excites a vibrational mode in matter. The transition to the excited vibrational mode requires energy, which is absorbed from the incident photon. To satisfy energy conservation the scattered photon will have less energy, equal to the

incident energy minus what was invested into the vibrational mode. If the photon is incident with energy, E_i, and the excited vibrational mode has energy, E_k, the resultant energy of the Raman scattered photon, E_R, will be $E_R = E_i - E_k$. Just as a vibrational mode can be excited by the incident light, if excited states already exist in the matter, they can be destroyed as well. In this case, assuming the same vibrational state, the energy of the Raman scattered photon, E'_R, would be $E'_R = E_i + E_k$. This case is less likely at room temperature and colder, due to the favourable probability to be in the ground state. Figure 2.4 shows a simple Jablonski diagram and a diagram of the energy spectrum for the scattered photons. As indicated by the intensity peak heights in Figure 2.4b, the probability for Raman scattering is relatively low, or equivalently, the Raman effect has a low scattering cross-section. For every Raman scattered photon, there are about 10^6 Rayleigh scattered photons [42]. Therefore, the measured intensity of Raman scattered photons is much less than that of Rayleigh scattered light. Rayleigh scattering is where the incident light creates or destroys no vibrational modes and therefore scatters with the same energy as the incident photon.

Nicklaus provides a very concise mathematical development of the interaction of light with vibrational modes that is consistent with the wave description of light and material lattice vibrations [42]. Consider a material, lattice or molecule with polarizability, α, in an external electric field, $\mathbf{E}$. The resulting dipole moment, $\mathbf{p}$ is

$$\mathbf{p} = \alpha \mathbf{E} \tag{2.1}$$

If the external field is wavelike, as is the case with light, it can be described as

$$\mathbf{E} = \mathbf{E}_0 \cos(\omega_0 t) \tag{2.2}$$

where , $\mathbf{E}_0$ is the amplitude of the field, ω_0, is the frequency of oscillation and t is the time. If a vibrational mode is excited due to the incident light, there will be a change in the polarizability due to that vibrational mode. The polarizability is therefore written

$$\alpha = \alpha_0 + \alpha_1 \cos(\omega_1 t) \tag{2.3}$$

where the polarizability of the ground state is α_0, the change in the polarizability due to the excited vibrational state is α_1, and the vibrational frequency of the excited mode is ω_1. It is clear from this that the change in polarizability is modulated by the frequency of the vibrational mode that causes the change. Combining these equations, the dipole moment is rewritten as

$$\mathbf{p} = \mathbf{E}_0 \left(\alpha_0 \cos(\omega_0 t) + \alpha_1 \cos(\omega_1 t) \cos(\omega_0 t)\right) \tag{2.4}$$

$$\mathbf{p} = \mathbf{E}_0 \alpha_0 \cos(\omega_0 t) + \frac{\mathbf{E}_0 \alpha_1}{2} \cos((\omega_0 - \omega_1) t) + \frac{\mathbf{E}_0 \alpha_1}{2} \cos((\omega_0 + \omega_1) t) \tag{2.5}$$

This final expression shows three oscillating dipole components at different frequencies. It is well established that an oscillating dipole will radiate light at the same frequency as it oscillates. Therefore, the dipole described by the first term will radiate at the same frequency as the incident light, ω_0. This is simply Rayleigh scattered light. The final two terms describe dipoles that will radiate at $\omega_0 \pm \omega_1$. This frequency shift is identical to the Raman shift described in Figure 2.4 for the Stokes and anti-Stokes Raman lines [42].

The reason that Raman scattering is such a powerful tool, is that the polarizability terms, α_0 and α_1, are highly dependent on the local environment. In reality, there are more than two polarizability terms because the vibrational system will have more than two modes. The collection of Raman scattering lines measured from a sample, over a wide range of wavelengths comprise a spectrum. Unique molecules, crystals and other materials all have their atoms arranged in unique local environments. The bonds between the atoms will be unique in their configuration and therefore generate unique vibrational modes. Measuring a spectrum of Raman lines provides information on which vibrational modes are present in the sample of interest, which in turn can be used to identify the composition of the sample. In modern usage Raman spectroscopy has been developed to perform the task of chemical "fingerprinting" [43, 44] and doing so over a surface to create Raman maps of this fingerprinting information [45].

2.2.2 Raman spectroscopy in Li-ion battery research

The desire to apply the chemical identification capabilities of Raman spectroscopy to Li-ion batteries is not novel. Some of the earliest work was performed by Inaba *et al.*, in 1995, who performed *in situ* Raman spectroscopy to study lithium intercalation into highly oriented pyrolytic graphite [46]. Figure 2.5 shows the spectra they reported. The disappearance and emergence of various peaks in the Raman spectra were determined to be phase transitions of the lithium within the graphite. This confirmed phases that had been previously measured by x-ray diffraction. Similar measurements were made by Itoh *et al*. in 1997, however they chose to study lithium insertion and extraction from a positive electrode, LCO. They were able to conclude that removal of lithium affected the electronic conductivity of the LCO and thus affected the optical skin depth. This change in skin depth lead to the observed shifts in the peaks in the Raman spectra [47]. Similar work was conducted by the research group of Frech who use Raman scattering to confirm Inaba *et al*.'s earlier results [48] and lend support to the two-phase model of lithium extraction from $LiFePO_4$ [49]. Studies of solvation in Li-ion battery electrolyte have been conducted in 1998 by both Morita *et al*. [50] and Wang *et al*. [51]. In both cases, changes in Raman spectra were used to infer a change in local environment within the electrolyte solution and estimate solvation of the electrolyte species.

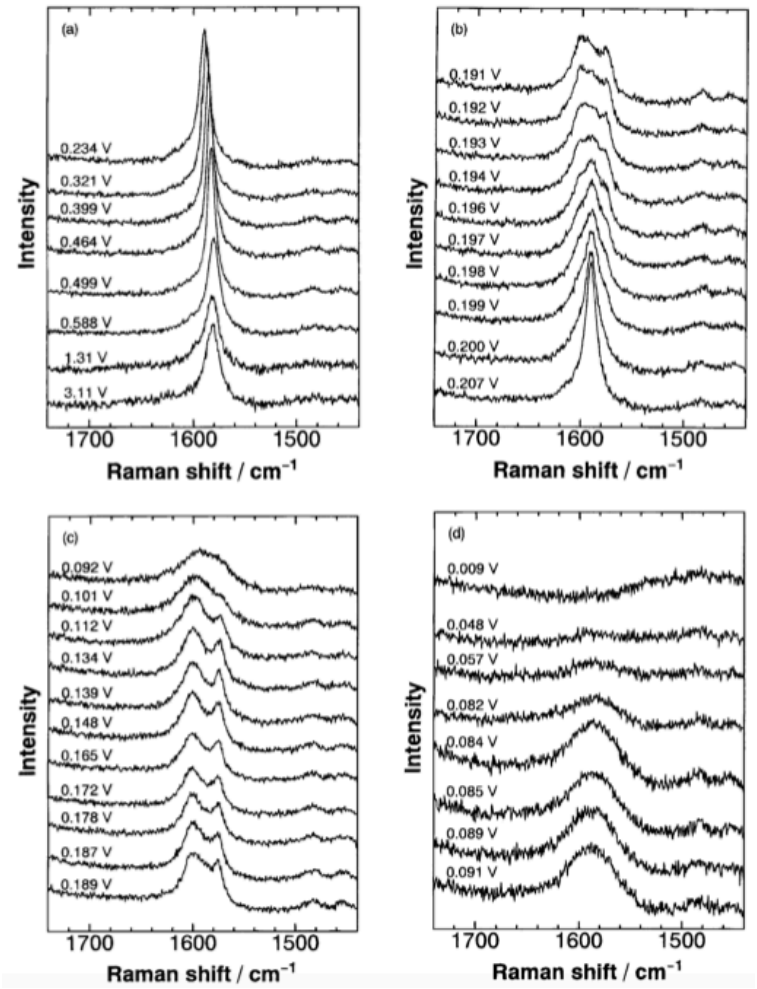

FIGURE 2.5: Raman spectra of highly oriented pyrolytic graphite at various cell voltages as lithium is intercalated. Electrolyte used was 1M $LiClO_4$ in a mixture of ethylene carbonate and diethyl carbonate. The cell was operated with a current of 12 µA. Taken from Ref. [46].

Considerable work has been done by Robert Kostecki and colleagues at Lawrence Berkley National Lab, in the early 2000s, to investigate the SEI and other Li-ion battery phenomena, *in situ*, with Raman spectroscopy. Raman spectroscopy was used, along with complimentary techniques, to measure the growth of a film on the surface of a $Li_2Mn_4O_9$ electrode [52]. Changes in Raman spectra were used as a complimentary technique to study degradation in a $LiNi_{0.8}Co_{0.2}O_2$ electrode [53]. Raman spectroscopy, again being used as a complimentary technique, was used to measure internal disordering in graphite as lithium was intercalated. Furthermore, additional Raman lines that appeared on top of the graphite signal were attributed to scattering from the SEI [54]. In 2004, Kostecki and McLarnon were able to report images constructed from a Raman mapping [55]. Figure 2.6 shows one of these images, indicating how the presence of each electrode component changes as the electrode degrades. The electrodes that lost the most power, Figure 2.6b – 2.6d, all seem to have lost the most graphite and acetylene black. These carbon additives serve to

increase electronic conductivity, indicating the electrodes lost power due to loss of conductivity [55]. Lastly, they have demonstrated charging kinetics that are inconsistent from particle to particle in an electrode, by performing Raman microscopy on individual electrode particles [56].

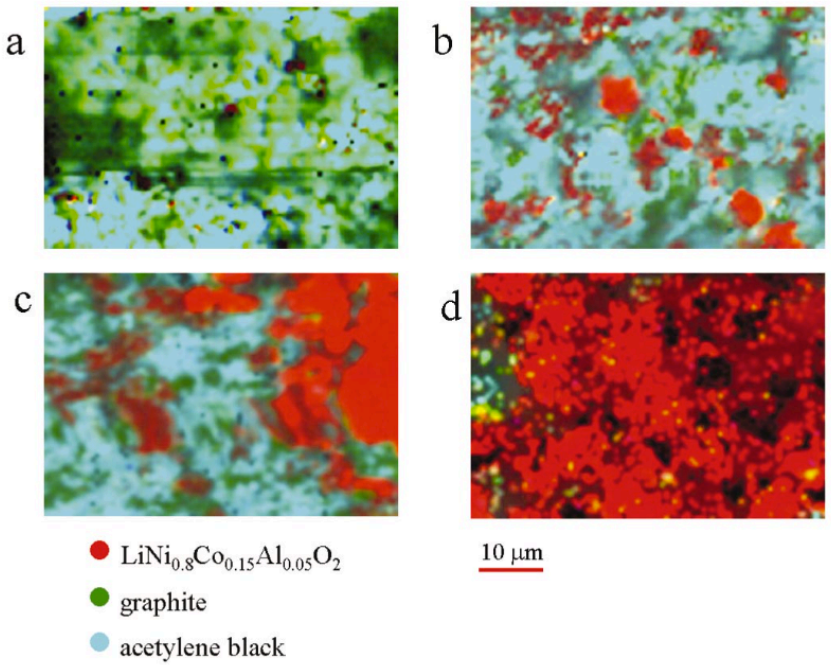

FIGURE 2.6: Raman mappings made by plotting the intensity of characteristic peaks for the components of a composite $LiNi_0.8Co_0.15Al_0.05O_2$ electrode. Colours corresponding to each component are indicated in the legend. Images are taken of (a) fresh, uncycled electrode and of (b-d) cycled electrodes ordered in increasing degrees of degradation. Taken from Ref. [55].

In the last decade, Raman spectroscopy has seen continued use in Li-ion battery research: to determine the configuration of the carbon coating applied to $LiFePO_4$ particles [57]; to *in situ* locate carbon in a silicon-carbon composite electrode and determine the amorphous nature of the silicon [58]; and to simply verify materials synthesis [59–61].

2.2.3 Atomic force microscopy

The atomic force microscope was developed in 1986 [62] as a successor to the scanning tunneling microscope and even older stylus profilers. Figure 2.7 shows a schematic of a typical AFM. A micro-fabricated tip, with nanometer sharpness, is raster scanned over the surface of interest by piezoelectric motors. The tip is mounted at the end of a cantilever, which bends in response to any interaction between the tip and the surface. The deflection of the tip can easily be measured using an optical lever setup. That is, a laser is reflected off the back of the cantilever, onto a quadrant photodiode. As the cantilever bends, the position of the reflected laser spot on the cantilever

changes accordingly. As the tip (or equivalently, the sample) is scanned, measurement of the cantilever deflection coupled with a feedback system allows the piezoelectric motors to keep the tip close to the surface. In this manner, the topographic features of the surface can be mapped [63]. AFM is frequently extended beyond this simple mode of operation, including modes with AC modulation of the cantilever, local probing of work function [64], conductivity [65], magnetic forces [66], lateral forces [67] and many more.

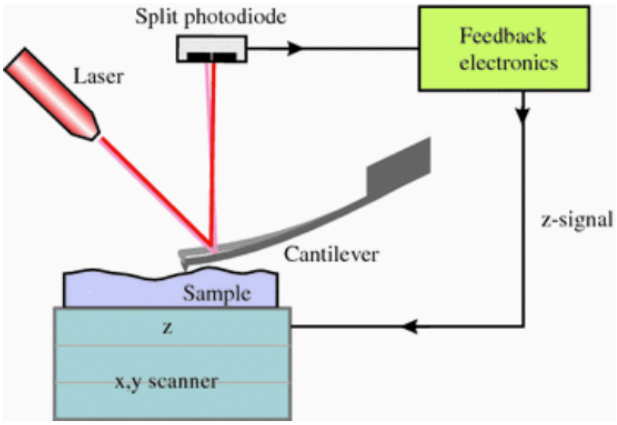

FIGURE 2.7: Schematic a typical AFM, implementing a cantilevered tip and optical lever detection system. In this particular schematic, the AFM is sample scanned, not tip scanned. Taken from Ref. [63].

2.2.4 Atomic force microscopy in Li-ion battery research

AFM has become a popular tool in surface characterization in all fields of science, and, as mentioned above, has spawned many new modalities that only serve to increase its capabilities and usefulness. It is not surprising that it has seen considerable use in Li-ion battery research. Pioneering work was done by Inaba *et al.*, who beginning in 1996, used STM to observe SEI growth, *in situ*, on both positive and negative electrode surfaces in a variety of electrolytes [68–71]. While this work was carried out with STM, it would set the foundation for the future work they and others would perform. Inaba *et al.* would quickly transition to AFM, relaxing the constraint of having a conductive sample. Their work continued in the form of direct, *in situ*, imaging of surface film formation and electrode degradation [32, 33, 72–75].

Over a similar time period, the research group of Doron Aurbach has performed similar work, integrating AFM into traditional battery research. Initially, Aurbach's group used AFM to observe *in situ* lithium metal deposition [36, 37, 76, 77], but would quickly transition to studying Li-ion electrodes. *Ex situ* AFM was used to determine the effect of processing on the roughness and morphology of $LiCoO_2$ electrodes [78]. Similar *ex situ* work was done to assess to morphology of chemical vapour deposition grown carbon electrodes [79]. Lastly, Aurbach's group has used

AFM, like Inaba, to *in situ* study the surface phenomena on a variety of electrode surfaces as they charge/discharge [35, 80, 81].

The work of Kostecki *et al*. in utilizing Raman spectroscopy was mentioned earlier. In many of those studies AFM and Raman were used separately, but as complimentary techniques. In a similar approach to Inaba and Aurbach's work, AFM was used to directly observe *in situ* SEI growth and electrode degradation [52–55, 82–85].

Kötz *et al*. used AFM to observe *in situ* SEI formation on graphite electrodes [86] and structural changes in graphite electrodes upon lithium insertion [87–89]. Similarly, Beaulieu *et al*. used AFM to observe morphological changes in alloying negative electrodes upon reaction with lithium [90–93]. In particular, Beaulieu *et al*.'s observation of volume expansion upon lithiation of alloying materials has been critical in understanding how to use such materials as a negative electrode material. Figure 2.8 shows an AFM image taken during this work. It was realized that upon lithiation of a SiSn sputtered thin film, the material expands vertically. However, when lithium is removed, the material can contract isotropically, eventually leading to cracks [90].

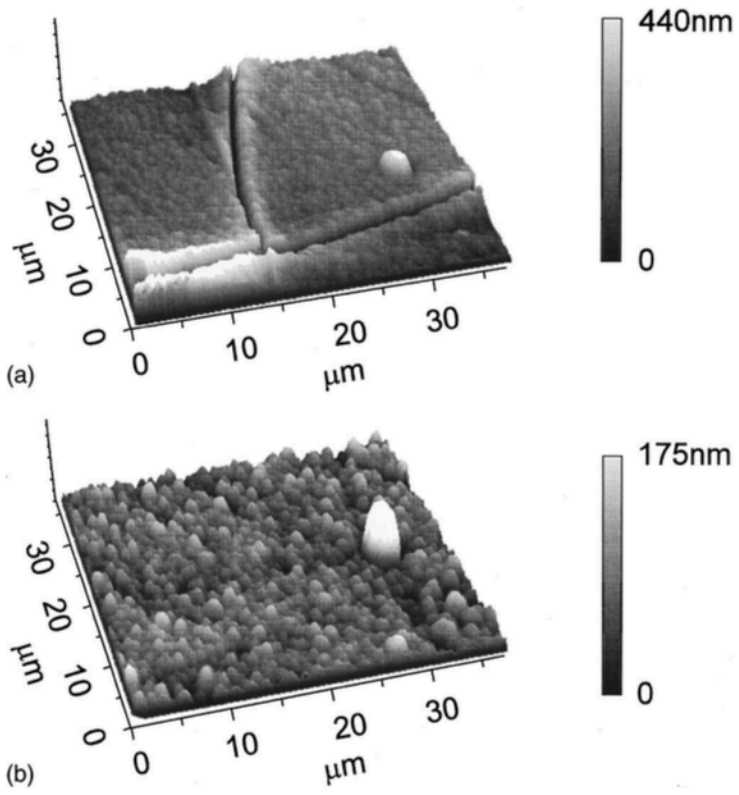

FIGURE 2.8: AFM image of sputtered SiSn thin film electrodes at different states of charge. (a) Electrode is void of lithium, domains have decreased volume, causing micron sized cracking; (b) electrode fully lithiated, volume is increased, filling in cracks. Taken from Ref. [90].

AFM has continued to be used in Li-ion battery research, in this manner. That is,

using an AFM to directly observe a morphology or topography change at the surface of a Li-ion battery electrode. However, in more recent years, researchers have been broadening the scope of their application of AFM. Zhu *et al*. measured lithium diffusion in $LiCoO_2$ nanograins, in response to an AFM tip-applied electric field [94]. Ramdon and Bushan assessed electrode mechanical integrity, at the nanoscale by using an AFM tip to measure hardness, elastic modulus, friction and other mechanical properties [95]. Kitta *et al*. used frequency-modulated AFM in liquids to determine the surface reconstruction of a $Li_4Ti_5O_{12}$ electrode in an aqueous battery electrolyte [96]. Considerable effort has been put into the development of electrochemical strain microscopy, originally by Kalinin *et al*., where the ionic response of an electrode in a tip-applied electric field results in a mechanical strain, which is measured by the AFM tip [97–101][90–94]. Finally, the development of scanning thermo-ionic microscopy, where a thermally induced stress is created by using a heated AFM tip, resulting in a change in local ion concentration. This has been used to map local ion concentrations in $LiFePO_4$ [102].

2.2.5 Tip enhanced Raman spectroscopy

Tip-enhanced Raman spectroscopy (TERS) is the marriage of Raman spectroscopy with the nanoscale imaging capabilities of an AFM. Raman spectroscopic techniques can be used detect chemical contrast, while AFM can be used to simultaneously obtain surface morphology, all with nanometre spatial resolution. Figure 2.9 shows a series of image that is analogous to the capabilities offered by TERS. Colour represents chemical information. The image in Figure 2.9a represents mapping done by typical Raman spectroscopy. Chemical information is present, but the image has low spatial resolution. The image in Figure 2.9b represents image acquisition by AFM. The resolution and sharpness of the image is very high, but as the absence of colour indicates, no chemical information is obtained. TERS is represented by the final image, in Figure 2.9c, where chemical information is present at very high spatial resolution.

Raman spectroscopy is an optical scattering technique, which means that it's spatial resolution is wavelength limited. TERS, however, utilizes the interaction of light with the AFM tip to achieve sub-wavelength resolution. The origin of this technique is in what is referred to as surface- enhanced Raman scattering (SERS). It was discovered that light will interact with localized surface plasmons in noble metal nanoparticles to enhance the Raman signal [103]. This technique was extended beyond metal nanoparticles, to the ends of AFM tips coated in noble metals [104].

The operating principle of TERS, as mentioned, relies on enhancement by the interaction of light with localized plasmons. A localized surface plasmon resonance (LSPR) appears to only be present in metal nanoparticles up to $200\,\mathrm{nm}$ in size [105]. The excitation of a LSPR will have the effect of increasing the magnitude of the electric field up to 10 000 times greater than the excitation field, in a region of $50\,\mathrm{nm}$ or less [105]. As mentioned above, the Raman effect has a low scattering cross section.

FIGURE 2.9: "Photography as an analogy to TERS: (a) Blurry colors: Classic optical microscopy is limited to the micro-scale. (b) Black and white: High topography resolution with SEM or AFM but (almost) no chemical information. (c) Color photography: TERS combines high lateral resolution with chemical information. (Photo: Basilique Notre Dame de Montréal by Harold Stiver, idea: Yason Yeo)." Taken from Ref. [42].

It becomes immediately clear how the field enhancement from a LSPR would simultaneously increase the probability of a Raman scattering event occurring, while ensuring the location of the event is confined to a sub-wavelength spatial region.

If one considers the case of light incident on a spherical metallic nanoparticle, the solution to Maxwell's equations is given by

$$\kappa(\lambda) = \frac{24\pi N_A a^3 \varepsilon_m^{3/2}}{\lambda \ln 10} \left[\frac{\varepsilon_i}{(\varepsilon_r + 2\varepsilon_m)^2 + \varepsilon_i^2} \right] \tag{2.6}$$

where κ is the extinction coefficient, λ is the wavelength of the incident light, N_A is the areal density of the nanoparticles, a is the nanoparticle radius, ε_m is the dielectric constant of the medium surrounding the nanoparticles, and ε_r and ε_i are the real and imaginary parts of the metal dielectric function, respectively [105]. The interpretation of the extinction coefficient is that it quantifies how much light is absorbed and scattered. It is clear that a resonance, or maximum, in extinction occurs when $\varepsilon_r = -2\varepsilon_m$. Using values for ε_r and ε_i , which are of course actually $\varepsilon_r(\lambda)$ and $\varepsilon_i(\lambda)$, measured from the bulk materials, solving Eq. 2.6 for silver and gold yields resonance values for light in the visible portion of the spectrum [105]. The energy transitions of the Raman effect typically require excitation from the visible part of the spectrum, hence the success that researchers have had in achieving enhanced Raman signals with such noble metal nanoparticles.

It is worth noting that Eq. 2.6 is only valid for perfectly spherical nanoparticles. If the nanoparticles are spheroids, the term that determines resonance, $\varepsilon_r + 2\varepsilon_m$, becomes $\varepsilon_r + \chi\varepsilon_m$, where χ is a geometric factor. The resonance is therefore highly sensitive to geometry. Beyond spheres and spheroids, the problem requires Maxwell's Equations be solved numerically [105]. Figure 2.10 shows how the LSPR varies with nanoparticles geometry. Figure 2.10a shows a plot of extinction as a function of wavelength for a variety of geometries. While still confined to the visible region of

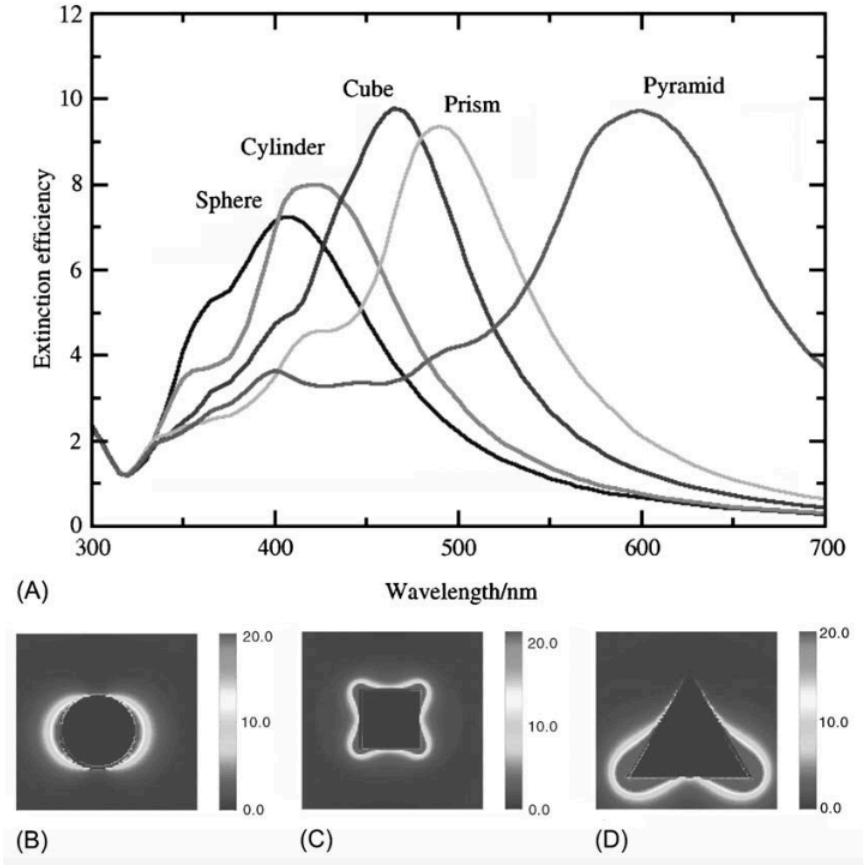

FIGURE 2.10: (a) Extinction spectrum calculated by finite element model for nanoparticles of a few regular geometries. Also shown are spatial maps of $|\mathbf{E}|^2$ for (b) a spherical particle with 50 nm radius, (c) a cubic particle of identical volume to (b), and (d) a pyramidal particle of identical volume to (b). Taken from Ref. [105].

the electromagnetic spectrum, the variation of shape causes the LSPR to span essentially the entire width of the visible spectrum. Furthermore, the shapes listed are all perfect geometries (i.e. no skewed axes, perfect symmetry, etc.). Imperfections that exist in real nanomaterials will cause the resonance wavelength to vary considerably. Figures 2.10b, 2.10c and 2.10d show the spatial variation of the resonant E-field with particle shape. Not only will the wavelength of the resonance change with geometry, but the location of the enhanced E-field will change as well. To utilize a LSPR to enhance a visible spectrum electromagnetic field for the purpose of increased Raman scattering with high and precise spatial resolution, the geometry effects are a significant challenge. To compound this, real geometries require computationally expensive numerical calculations to understand the LSPR.

Despite these complications, TERS has successfully been demonstrated, as referenced earlier in this section. The resonances shown in Figure 2.10a are relatively broad, which means that TERS systems need not match the resonance frequency exactly with the excitation source. Given well designed AFM tips, coated with or

made from noble metals, it should be possible to implement standard AFM techniques along with a Raman spectroscopy system. With development of the technique, AFM in liquid, with simultaneous tip-enhanced Raman spectroscopy *in situ* mapping of the chemistry and morphology along the surface of battery electrodes should be possible.

2.3 Cantilever sensors

An alternative technique to be developed for the study of Li-ion battery materials and the formation of an SEI is utilization of cantilever sensors. Cantilevers are force transducers. In the case of AFM, discussed in section 2.2.3, a cantilever can transduce the force at a nanometer sharp tip to a deflection. In a cantilever sensor, a single surface of the cantilever is typically functionalized, or otherwise responsive towards the species or event of interest. The presence of this species or occurrence of the event causes the functionalized surface to develop a stress. Because only a single side of the cantilever is responsive, the stress is unmatched, and bending, or deflection, occurs.

2.3.1 Operation of a cantilever sensor

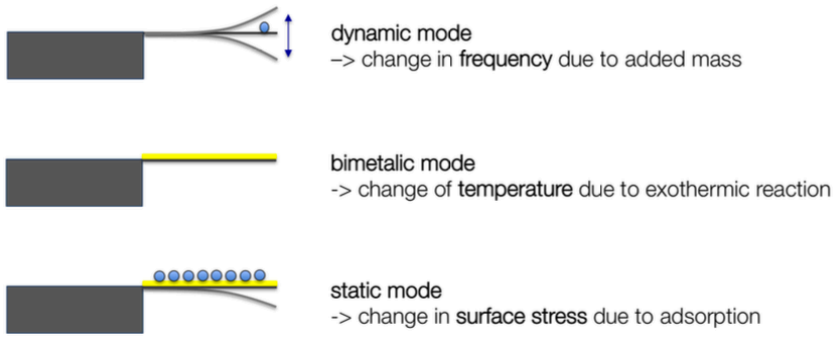

FIGURE 2.11: Schematic of operational modes of a cantilever sensor. Yellow indicates the presence of a metallic layer on the cantilever, such as a gold coating. Blue circles indicate species that interact with the cantilever surface. In dynamic mode, the cantilever is oscillated under an external excitation, such as a piezoelectric shaker. In bimetallic and static modes, the cantilever is not driven externally. Taken from Ref. [106].

A cantilever sensor is typically operated in three different ways. Figure 2.11 shows diagrams of each mode of operation. Dynamic mode utilizes an externally driven cantilever, oscillated on resonance, perhaps by a piezoelectric element, or photo-thermal laser excitation. The resonance frequency of a cantilever will decrease if mass is added. Therefore, as species adsorb/desorb on the surface, the frequency

changes [106]. This mode is not utilized in this thesis and will not be further discussed. The second mode, bimetallic mode, requires a composite cantilever with two different layers. If a change in temperature occurs, the different coefficients of thermal expansion between the two layers will cause different relative expansion. This results in a difference of stress between the two layers, causing the cantilever to bend [106]. While this mode will be present to some extent in any cantilever that is made of two different materials, especially if one of those layers is a metal, this mode is not primarily considered in this thesis. As will be discussed, the cantilevers used in this thesis are submerged in a relatively large liquid bath, which acts as a thermal reservoir. Furthermore, the cantilevers used are metal coated, but the metal coating constitutes approximately 0.2% of the cantilever thickness, and should not contribute to the measurable thermal response. Finally, in the third mode of operation, simply named static mode, adsorption of species and changes to surface chemistry can cause surface stress on the cantilever surface. In the example presented in Figure 2.11, a metal coated cantilever can adsorb ions and the resulting change in charge density produces a surface stress and causes bending [106]. This is the mode that will be utilized in this work, because, as mentioned, it is sensitive to changes in surface chemistry and phenomenon of SEI formation in Li-ion batteries is precisely that.

The basics of cantilever sensors will be reviewed, however only briefly, as much of it will not be directly applicable, due to the unique geometry and chemistry considerations presented later in this thesis. To be as relevant to Li-ion batteries as possible, this will focus on a metallic electrode and/or a cantilever with a metallic layer in an electrolyte. Discussion of this topic typically starts with the Shuttleworth equation, relating surface tension to the surface Helmholtz free energy [107]. As derived originally by Shuttleworth, it is written

$$\gamma = F + A\frac{\partial F}{\partial A} \tag{2.7}$$

where γ is the surface tension, F is the surface Helmholtz free energy and A is the interfacial area. Despite the fact that new interpretations have arisen which question its derivation and validity, it is still one of the most important results in surface physics [108]. By recognizing that $\partial\epsilon = \partial A/A$, Eq. 2.7 can be written in what may be a more familiar form as a function of ϵ, the strain [109]. The surface Helmholtz energy can either be thought of as the energy associated with changing the area of the surface, or equivalently the energy associated with moving a bulk atom to the surface, or vice versa.

Further development of Shuttleworth's equation, where the effect of an applied electric potential is considered, produces the generalized Lipmann equation or the Couchman-Davidson equation [109], written

$$\frac{dF}{dE} = -q - (F - \gamma)\frac{d\epsilon}{dE} \tag{2.8}$$

where E is the applied electric potential and q is the areal charge density. In this discussion, the surface tension, γ, presented by Shuttleworth, is often referred to as the stress, σ. Both the stress and strain terms are properly treated as tensors, σ_{ij} and ϵ_{ij} respectively, but can reduce to scalars in simple geometries. For tensor calculations, Eq. 2.7 and 2.8 need only have stress and strain tensors inserted, as well as the Kronecker delta multiplied by F, where necessary. The above demonstrates that both insertion of a metal into liquid and application of a charging voltage will change the surface energy resulting in a surface stress.

The generation of the surface stress in a metallic film on a substrate has been related to the deflection of the film by Stoney in 1909 [110] as

$$P = \frac{4}{3}\frac{E_s t_s^2}{l^2 t_f} z \tag{2.9}$$

where P is the tension per unit area, E_s is the substrate Young's modulus, t_s is the thickness of the substrate, l is the length of the film or the substrate, t_f is the thickness of the metallic film and z is the vertical deflection. Although Stoney's notation uses tension per unit area, P, this is equivalent to the stress, σ. This system of a thin metallic layer on a thicker substrate correctly describes a metal coated cantilever. Thus, with this formalism, the relationship between stress and deflection for a cantilever can be known. Most cantilevers, however, are described in terms of a spring or force constant, not an elastic modulus. The spring constant, k, of a rectangular beam, fixed at one end is given by [111]

$$k = \frac{E_s w_s t_s^3}{4l^3} \tag{2.10}$$

where w_s is the width of the beam. Note that the notation in Eq. 2.10 has been kept consistent with the notation of Eq. 2.9. Combining the two, under the assumption that the substrate layer is much larger than the thin metallic film and is the primary contributor to the overall spring constant, the stress-deflection relationship is written

$$\sigma = \frac{16}{3}\frac{kl}{w_s t_s t_f} z \tag{2.11}$$

2.3.2 Battery electrode cantilevers

To create a cantilever sensor that is responsive to battery phenomena, it makes sense to make a cantilever that directly incorporates a battery material. The typical formulation of a composite battery electrode is a slurry of active material, conductive diluent and polymeric binder spread on a thin metal foil that serves as the back electrode, or current collector [23]. The discussion in section 2.3.2 has focused on cantilevers constructed from an underlying substrate with metal film on top. The battery electrode and the cantilever can be combined if the metal film on a cantilever is utilized as the current collector for the battery electrode. Figure 2.12 shows a schematic of

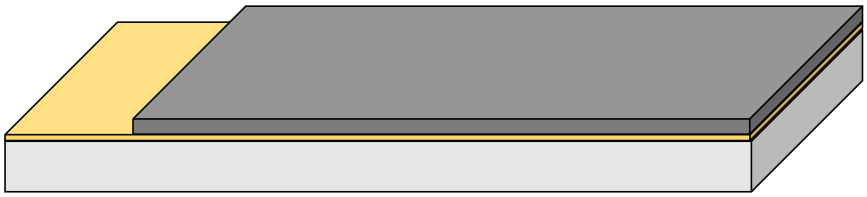

FIGURE 2.12: Schematic of proposed battery electrode cantilever. The bottom layer is an inert substrate that primarily determines the elastic properties of the cantilever. The middle layer is a thin metal film that functions as a current collector for the battery material. The top layer is formed from a slurry of active material, conductive diluent, and binder. Note that cantilever dimensions and relative layer thicknesses are not to scale, but the ordering of thicknesses (substrate layer > active layer > metal layer) is correct. The active layer does not cover the exposed metal layer; the exposed metal area is to clamp the fixed end of the cantilever and make electrical contact.

the proposed battery electrode cantilever. The bottom substrate layer is thickest and as such will primarily determine the elastic properties of the cantilever. It must be inert, so that stress response is determined by only a single surface, that is the active battery layer. The metal layer serves as the current collector for the active layer. A section of the metallic layer is left exposed at the fixed end of the cantilever for the purpose of clamping and establishing electrical contact. On top of the metal layer is the active layer. This is the battery material with binder and conductive additive.

It is known that electrochemical cycling of the battery material will result in both SEI formation on the surface of the active particles and volume change of the active particles that varies with intercalated lithium concentration [35, 112]. The SEI is an alteration of the surface chemistry and surface morphology, which should in turn cause a change in the surface free energy and result in a stress. This should be measurable in the static mode of cantilever sensing discussed in section 2.3.2. Volume change of the active material upon lithium intercalation/deintercalation is equivalent to the different thermal expansion utilized in the bimetallic mode of cantilever sensing. In the case of bimetallic mode as it was presented earlier, differential volume change occurs during a temperature change due to differences in thermal expansion coefficients. When a battery electrode cantilever is charged, only the volume of the active layer should change. This is again differential volume change throughout the cantilever. To measure both SEI formation and active particle volume change, it is experimentally convenient that a battery electrode cantilever can be set up in static mode and deflection will occur from both sources. Decoupling these within the measured deflection, however, may prove challenging.

2.3.3 Electrochemistry of lithium ion batteries

The second most common method of electrochemically testing batteries, after constant current potentiometry, is cyclic voltammetry (CV), which is the test of choice

in this thesis. Current potentiometry, or supplying a constant current and measuring voltage, is typically used for the study of battery electrodes. Due to limitations of electrochemical test system used (see Section 3.4.4), constant current modes were unavailable. During a CV, the potential of a working electrode is varied linearly in time relative to the potential of a reference electrode. The potential is swept between a maximum and a minimum value, with the direction of the potential change switching every time the potential endpoints are reached, hence the cyclic quality of the test. In a battery material, during a CV, lithium will intercalate or deintercalate depending on the direction the potential is swept. Currents will be measured at intercalation potentials and the general shape of the voltammogram can reveal information about the kinetics of the reactions.

Providing a mathematical framework to this, however, is rather difficult. The Butler-Volmer model is typically cited to describe the potential-current behaviour of an electrochemical system, however, its use for a battery electrode is rather limited. A more applicable model is the non- equilibrium porous electrode theory presented by Ferguson and Bazant [113]. As is implied by the name, non-equilibrium thermodynamics are taken into consideration, as are the porous and tortuous nature of a real battery electrode. Furthermore, diffusion in solids, multi-step intercalation kinetics, phase separation during charging and other non-linear dynamics are all considered. The result is a system of equations that describe the current-potential characteristics of a real electrode, but are solvable in three dimensions only by computational means. Due to the degree of complexity the equations are not shown here and are somewhat beyond the scope of the work in this thesis, however, they can be found in Table 1 in Ref. [113].

Chapter 3

Experimental Methods and Instrumentation

3.1 Materials for Raman spectroscopy studies

3.1.1 Samples for confocal Raman microscopy

A molten-state synthesized solid $LiFePO_4$ ingot was donated by Hydro Quebec, through a collaborative research partnership. Figure 3.1 shows an image of the parent ingot from which the ingot used in this work was sourced. Synthesis was performed by researchers at Hydro Quebec, but details of the synthesis can be found in Ref. [14]. Small pieces of the ingot were chipped away using tweezers and mounted to an AFM disk using silver epoxy. The ingot piece was then manually sanded and polished until flat. Aluminum oxide sand paper, all the way down to diamond $0.3\,\mu m$ grit fiber polishing film (Thor Labs) was used. This polishing was done to ensure quality imaging in a confocal Raman microscope, which cannot tolerate large changes in sample topography.

FIGURE 3.1: Photograph of a solid ingot of $LiFePO_4$ synthesized from the molten-state. Taken from Ref. [14].

Another molten-state LFP ingot was obtained from Hydro Quebec, this one being an ingot of Li_xFePO_4. Synthesis was similar as in Ref. [14], except $LiFePO_4$

particles having undergone chemical delithiation by aqueous $K_2(SO_4)_2$ prior to heating to the molten-state [114]. Similar preparation as above was performed with this ingot, by Aaron Mascaro, as part of his work of measuring ionic transport in LFP [115]. Again, imaging by confocal Raman microscopy was performed, in this case to complement the work of Mascaro *et al*. [115] on the same sample.

3.1.2 Samples for tip enhanced Raman spectroscopy

Etched colloidal LFP nanoplatelets (roughly $15\,\mathrm{nm}$ thick) were prepared by Andrea Paolella of Hydro Quebec, synthesized as per Ref. [116]. Paolella then modified the surface of the nanoplatelets with an alkane chain so the platelets could disperse in chloroform. The platelet dispersion was diluted to a variety of concentrations and drop cast on a template stripped gold surface. The varying concentrations were used to search for sub-monolayer coverage of nanocrystals. Template stripped gold was used because it has atomically flat terraces and gold substrates are common in TERS due to the plasmonic nature of gold. It is known that plasmons in a gold TERS tip can interact with a nearby gold. Flat terraces mean finding a nanoplatelet is easier and they are likely to lie flat. These nanoplatelets on a gold substrate were verified as good samples with AFM and then imaged using tip enhanced Raman spectroscopy.

3.2 Instrumentation for Raman spectroscopy studies

3.2.1 Raman microscope with scanning probe and confocal imaging capabilities

All Raman imaging was performed on a modified AIST-NT SmartSPM 1000, located in the research group of Andreas Ruediger at Institut national de la recherche scientifique, Centre Énergie Matériaux Télécommunications (INRS-EMT) in Varennes, Quebec, Canada. Modifications of this particular microscope would become the AIST-NT OmegaScope 1000. Direct operation of the microscope was handled by Gitanjali Kolhatkar, and when TERS experiments were performed, tips were fabricated by Jiawei Zhang, both of INRS-EMT.

Figure 3.2 shows a photograph of the microscope. When being used as a confocal optical microscope, the tuning fork AFM probe is removed, as the beam path from the top objective intersects the probe. The 0.7 numerical aperture (NA) confocal optics can be connected to a charge coupled device (CCD), for top down video monitoring, or to the Raman excitation laser and spectrometer for confocal Raman imaging. Utilization of the sample scanner enables two- dimensional confocal Raman mappings with $0.5\,\mu\mathrm{m}$ resolution.

The side objective is utilized for TERS experiments. It is a 0.42 NA lens with a $20\,\mathrm{mm}$ working distance (Mitutoyo). The lens is inclined at 65° to the normal of the sample stage, or alternatively 65° to the tip axis. The angle and lens size are constrained by the size of the tuning fork assembly [42]. The lens is mounted on a

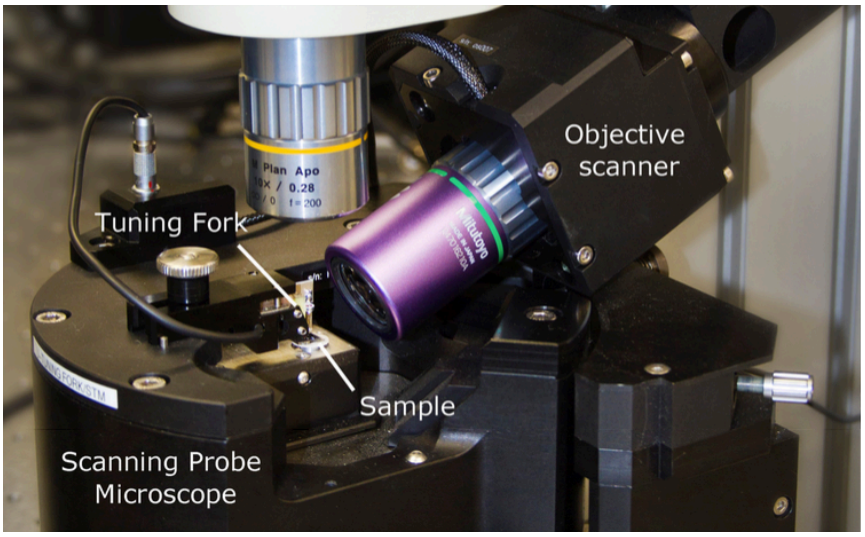

FIGURE 3.2: Photograph of combined AFM-Raman microscope with TERS capabilities at INRS- EMT. The top objective is used for confocal imaging when the AFM probe is removed. A tuning fork with a glued on etched gold wire serves as an AFM tip. The side objective is used to focus a Raman excitation source on the tip for TERS measurements. The base of the microscope contains piezoelectric elements required for sample scanning capabilities. Not pictured are the Raman excitation or spectroscopy optics. Taken from Ref. [42].

piezoelectric scanner with $30\,\mu m$ range in directions perpendicular to the lens optical axis, and $12\,\mu m$ in the direction parallel to the optical axis [42]. The lens is used to focus Raman excitation laser light to a micron-sized elliptical focus, and the objective piezo-scanner can position that focus at the AFM tip apex, where one would hope to excite a LSPR.

The scanning probe unit is based on a tuning fork with etched gold wire tips built in-house at INRS-EMT. A $32\,kHz$ tuning fork is used, which does not require standard optical beam deflection techniques for detection. This simplifies the optics of the microscope which already has optics for Raman excitation and collection of Raman scattered light. The tuning fork is shown in Figure 3.3c, where the gold wire tip is barely visible. The gold wire is glued vertically to one arm of the tuning fork and the tuning fork itself is mounted vertically to an epoxy board. A piezoelectric shaker in the AFM head excites the tuning fork on resonance, and the voltage across the tuning fork is measured with lock-in techniques. In this configuration, the tip is sensitive to lateral forces, and remains at constant height above the sample [42]. This is in contrast to a vertical oscillation (see Figure 3.3a). Constant height above the sample is thought to be essential for TERS, because the enhancement is highly localized, with strong distance dependence. Tip fabrication involves etching gold or silver wire in HCl solutions under applied square electrical pulses of $3.5\,V$, to produce tips with $30\,nm$ radius [42]. The tips are then positioned with a micromanipulator and glued to the end of the tuning fork.

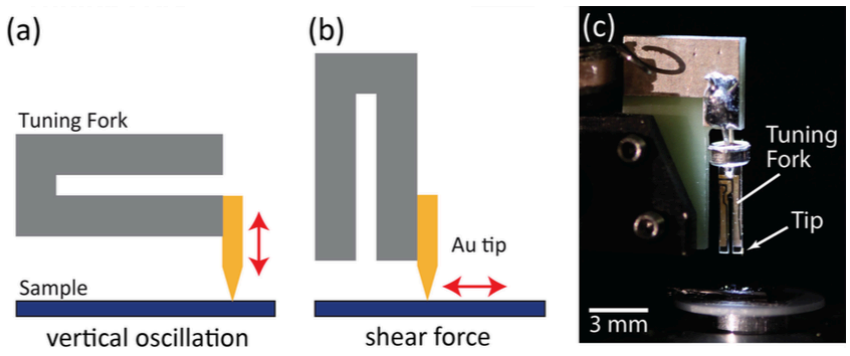

FIGURE 3.3: Schematics and photograph of tuning fork orientations for AFM applications. (a) tuning fork with glued tip in a vertical oscillation configuration; (b) tuning fork with glued tip in a horizontal oscillation configuration; (c) photograph of tuning fork-tip system used in the microscope at INRS-EMT. Taken from Ref. [42].

Not shown in Figure 3.2 are the external optics associated with the Raman excitation and measurement of the Raman spectrum. Figure 3.4 shows a schematic of the optics for the entire microscope. The excitation light source is one of three lasers. Despite only one laser being shown, a red, green and blue laser source exist. Based on work in the literature, studies on $LiFePO_4$ were done with exclusively with green lasers, so in all measurements the $532\,\mathrm{nm}$ green laser was used. The laser power is attenuated using a neutral density filter, expanded to match the entrance size of the side objective, and focused onto the AFM tip. Scattered light is collected by the same objective, and filtered to remove any reflected and Rayleigh scattered light. The remaining light is focused onto a pinhole, thereby removing any stray light that is not parallel to the optical axis. The light enters a Czerny-Turner spectrometer, which utilizes a diffraction grating to separate it into spectral components and a pair of parabolic mirrors to focus the light onto a CCD. The CCD is cooled by Peltier elements, to reduce thermal noise. Because the CCD has many pixels, the entire spectrum can be measured at once, or at least over a single window of integration time to achieve sufficient signal-to-noise ratio.

The microscope is located in a climate controlled room, surrounded by blackout curtains. This reduces fluctuations from changing temperature and stray light.

3.2.2 Atomic force microscope

A Digital Instruments Nanoscope III Multimode AFM was used to characterize the nanoplatelets deposited on template stripped gold substrates. Figure 3.5 shows a photograph of the Nanoscope. Mikromasch HQ:NSC15/No Al silicon cantilevers were used in the Nanoscope. Cantilever resonance frequency and spring constant were quoted as $325\,\mathrm{kHz}$ and $40\,\mathrm{N\,m^{-1}}$ respectively, and tip apex was quoted as $8\,\mathrm{nm}$. The cantilevers were loaded into the cantilever holder in the AFM head. The deflection system was aligned by steering the laser beam to the tip of the cantilever,

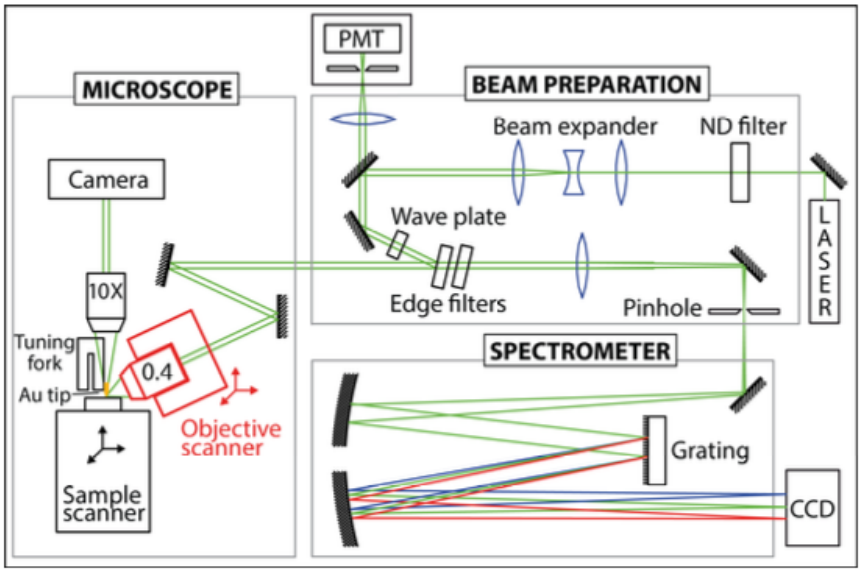

FIGURE 3.4: Diagram of the optical paths in a TERS measurement. The excitation beam power is reduced by an neutral density filter and expanded to match the entrance size of the objective. The scattered light is filtered to remove any Rayleigh light and a Czerny-Turner spectrometer separates the scattered light into component wavelengths. Taken from Ref. [42].

and centering the reflected beam on the photodiode. The AFM was operated in tapping mode, meaning a piezoelectric shaker excites the cantilever at its resonance frequency and the amplitude is monitored on the photodiode. The oscillating tip and the sample surface are brought into intermittent contact by coarsely lowering the tip using a stepper motor and then raising the sample using a piezoelectric scanner. As the tip gets closer to the surface, the repulsive interaction of the surface with the tip attenuates the amplitude of the tip oscillation. The amplitude, as measured on the photodiode, is kept constant by feedback electronics by modulating the height of the tip above the surface. In this manner, the surface topography is mapped as the tip is scanned laterally and the tip height is adjusted.

3.3 Materials for cantilever sensing studies

3.3.1 Cantilever fabrication

The solid LFP molten-state ingot discussed earlier in this chapter was evaluated as a possible cantilever material. In this attempt, the fabrication of a battery electrode cantilever was considered in a top-down manner, following the scheme in Fig. 2.12. For synthesis and other information about this material, see section 3.1.

For bottom-up (again following the scheme in Fig. 2.12) fabrication of a battery electrode cantilever, muscovite mica was chosen as the substrate material. Mica has been used with success previously as a cantilever material [117] and has been

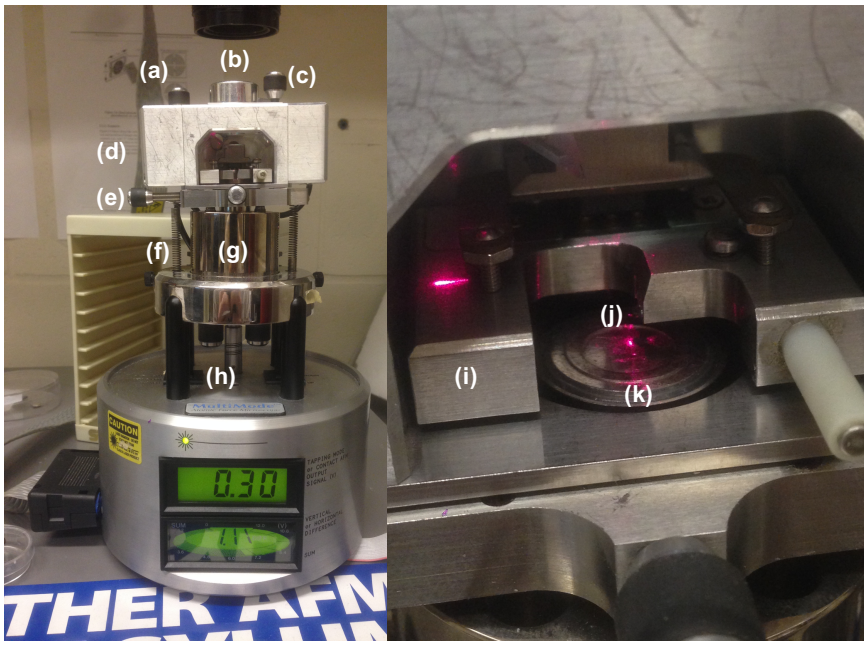

FIGURE 3.5: Photograph of Digital Instruments Nanoscope III Multimode AFM. (a) photodiode adjustment knob; (b) optical viewport; (c) laser adjustment knob; (d) AFM head; (e) xy-stage with coarse adjust screws; (f) springs; (g) piezoelectric scanner (inside column); (h) coarse approach motor and screws; (i) cantilever holder; (j) cantilever with tip; and (k) sample stage.

shown to be an inert substrate in electrochemical testing [118]. Furthermore, mica is optically transparent, meaning standard beam deflection can be implemented by allowing the laser to pass through the mica layer and reflect off the middle metallic layer. Sheets of $150\,\mu m$ thick, $25.4\,mm$ square V-1 grade muscovite mica sheets were obtained from SPI Industries. Figure 3.6 shows a photograph of one of these mica sheets. Some small imperfections can be seen near the cut edges, but overall are very high quality. Mica was split into approximately $50\,\mu m$ thick layers which were cut into $10\,mm$ x $1.5\,mm$ cantilevers using a wire saw.

Materials for the active layer were donated by collaborators at Hydro Quebec. Active materials included $Li[Ni_{1/3}Mn_{1/3}Co_{1/3}]O_2$, nanosized $LiFePO_4$ and a silicon carbon composite. Acetylene black (Denka Co.) was supplied for use as conductive diluent and polyvinylidene fluoride (PVDF) dispersed in n-methyl-2-pyrrolidone (NMP). The ratio of active material to conductive additive to binder, by weight, was 84:8:8, following the example of Ponrouch and Palacin [119]. Electrode slurries were mixed according to Ref. [119], specifically, 15 hours of magnetic stirring, interrupted every 5 hours for 10 minutes in an ultrasonic bath. After deposition of the slurry on metal coated mica cantilevers, the NMP was evaporated by heating in a furnace at $70\,^{\circ}C$ for two hours.

For electrolyte solvents, ethylene carbonate (EC) and propylene carbonate (PC) were selected. This choice was mainly influenced by related projects in which low

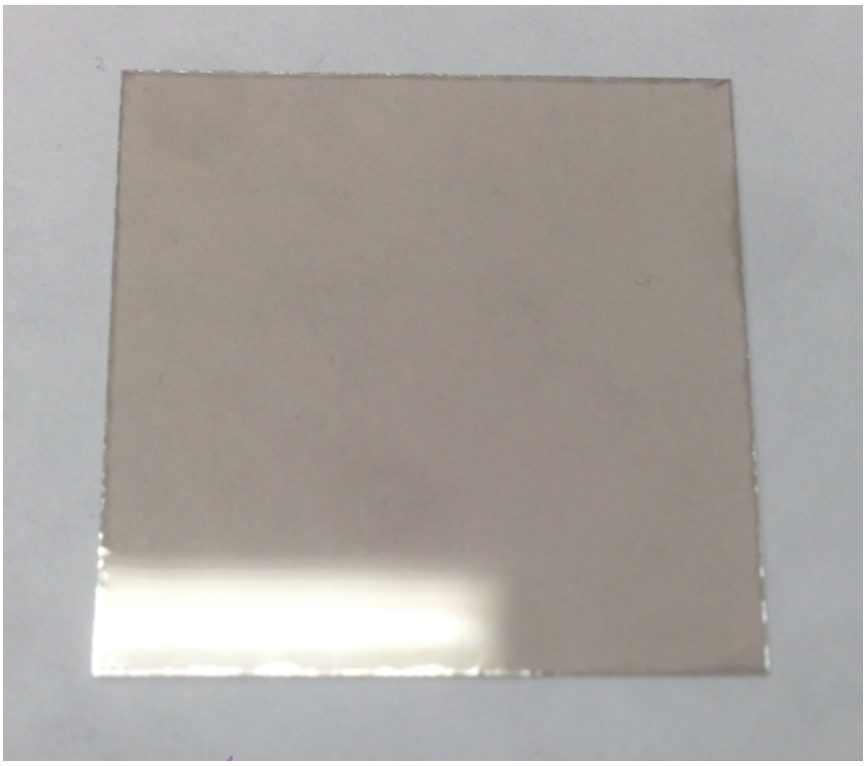

FIGURE 3.6: Photograph of a $25\,\mathrm{mm}$ square, $150\,\mu\mathrm{m}$ thick sheet of V-1 grade muscovite mica.

vapour pressure solvents are useful. Despite this other utility, they are perfectly acceptable solvents and still among the most common solvents used in commercial batteries, despite the fact that PC has fallen out of favour in graphite-containing batteries. 1M $LiPF_6$ was mixed into a 1:1 (by volume) mixture of EC/PC. As most Li-ion battery work is referenced versus the potential of the Li^+/Li redox couple, lithium metal was chosen as the material for both the counter and reference electrodes. Lithium metal is a common counter/reference electrode in the field and was recommended by collaborators at Hydro Quebec. Therefore, $3.2\,\mathrm{mm}$ thick lithium wire (99.8% purity) was obtained from Alfa Aesar, from which pieces of lithium could be cut to make electrodes.

As will be discussed in Chapter 5, circumstances arose that required the switch to an aqueous system. Following the work done by Wang *et al.* [120, 121], 1M Li_2SO_4 aqueous electrolyte was used, with a platinum wire counter electrode and a Ag/AgCl (sat. KCl) reference electrode that had been obtained for previous work.

All electrode and electrolyte materials sourced from Sigma Aldrich unless otherwise indicated.

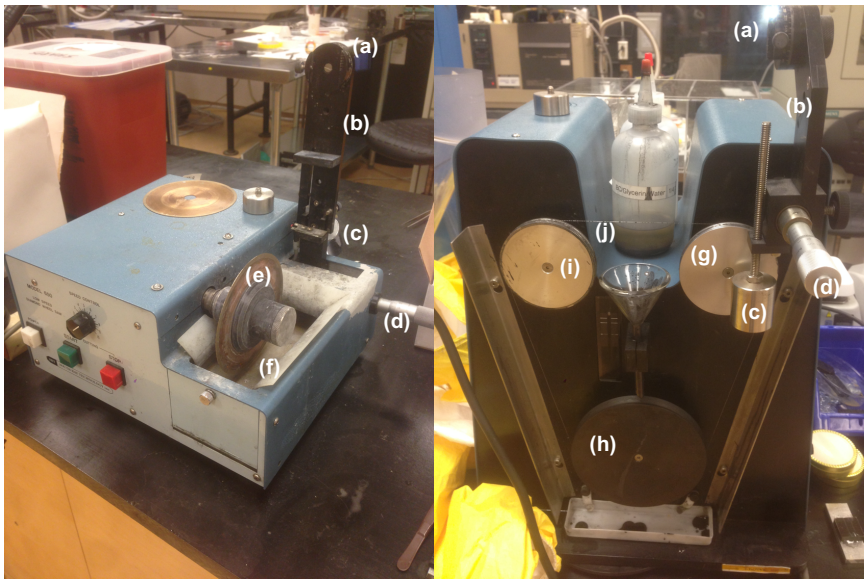

FIGURE 3.7: Photograph of South Bay diamond saw (left) and South Bay wire saw (right). (a) single- axis goniometer; (b) work arm; (c) counter weight; (d) micrometer; (e) diamond cutting wheel; (f) water bath, shown here without any water; (g) drive pulley; (h) tensioner pulley; (i) free pulley; and (j) stainless steel wire.

3.4 Instrumentation for cantilever sensing studies

3.4.1 Cutting and polishing tools

A South Bay Model 650 low speed diamond saw was used to cut cantilevers from both the solid ingot LFP and mica. Figure 3.7, left panel, shows a photograph of the diamond saw. The mica and LFP were mounted on graphite blocks in South Bay MWH135 mounting wax. The block, wax and sample are all heated using a heat gun to above the wax melting temperature and the wax applied. Once cooled to room temperature, the wax solidifies and holds the material to the block. The block is held in a single axis goniometer, by a set screw, at the end of the work arm. The work arm pivots to lower the sample onto the diamond coated cutting wheel. The base of the work arm is positioned using a micrometer. Counter weights on the work arm adjust the force with which the material is pushed into the cutting wheel. The cutting wheel rotates slowly and through a water bath. This provides gentle application of force, lower friction and a cleaner wheel, all of which contribute to reduce damage to the material during cutting. The wheel used is 4 inch in diameter, 0.012 inch thick.

A South Bay Model 810 abrasive slurry saw, or wire saw, was used to cut cantilevers from mica. Figure 3.7, right panel, shows a photograph of the wire saw. Mica samples were mounted in the same manner as with the diamond saw. It was learned the cuts were less destructive if mounting wax was also applied on top of the mica sheet, in addition to on the bottom. A 0.010 inch thick stainless-steel wire

loop is run through three pulleys. One pulley is motorized, one is suspended on a spring-loaded tensioner and the other is free turning. A screw controls the length of the tensioner spring which partially supports the weight of the pulley. The remainder of the weight of the pulley is supported by the wire, thereby setting the tension in the wire. The wire carries a slurry of boron carbide abrasive, glycerine and water, mixed at a weight ratio of 1:4:1. Each of the pulleys have grooved tracks for the wire that also facilitate circulation of the abrasive slurry. The work arm, positioned at its base with a micrometer, lowers the mica onto the wire, and as the motor driven pulleys rotate the wire, it carries the abrasive slurry across the surface of the mica. The movement of the abrasive slurry slowly and gently develops a cut.

A Universal Laser Systems X-660 laser cutter was also used to cut cantilevers from mica. The laser cutter operates by pulsing a focused $60\,\mathrm{W}$ infrared CO_2 laser to ablate the sample in a controlled manner. The laser head and focusing optics are mounted on a series of motorized rails that can move the laser head in two-dimensions over the work surface. The location and firing of the laser are determined by computer interpretation of a computer automated drawing (CAD), similar to the operation of an inkjet printer.

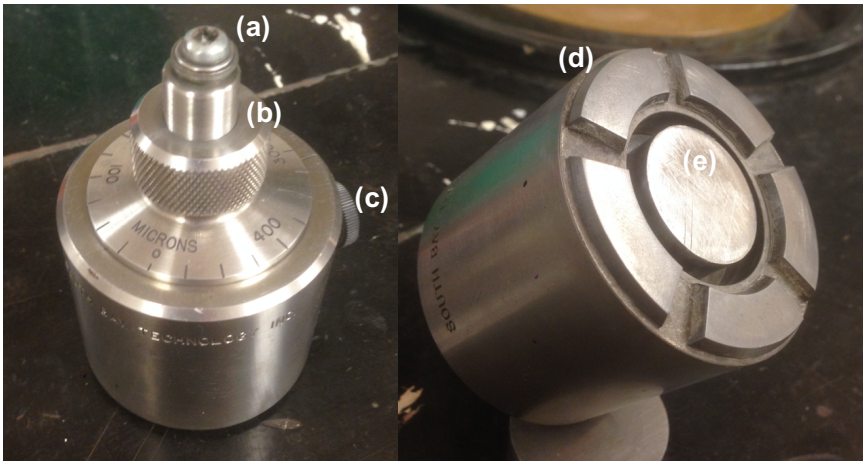

FIGURE 3.8: Photograph of South Bay lapping fixture. (a) sample mounting disk screw; (b) micrometer screw and dial; (c) set screw; (d) boron carbide feet; and (e) sample mounting disk.

The sections of LFP cut from the solid molten-state ingot needed to have their thickness reduced to function as a cantilever with a reasonable spring constant and stress sensitivity. A South Bay lapping fixture was used to achieve polishing with high precision control over the thickness. Figure 3.8 shows a photograph of the lapping fixture. The sample is mounted to the polishing disk with wax, as was done above with the cutting tools. The disk is attached to the end of a hollow micrometer screw by long screw that passes through the centre of the micrometer. The micrometer is used to extend the disk and sample a controlled amount beyond the durable boron carbide feet. This distance is locked in with a set screw. During polishing, only the exposed thickness of the sample can be polished, allowing precise control of the

final thickness of the sample. Polishing was done with aluminum oxide sandpapers of varying grit.

3.4.2 Metal film deposition

Positive electrodes in Li-ion batteries use aluminum as a current collector. Therefore, to function as battery electrode cantilevers, the cut mica cantilevers were coated with thin films of aluminum. To do this, the aluminum deposition was performed in an evaporator. Figure 3.9 shows the interior of the aluminum evaporator. Mica cantilevers were mounted to a glass microscope slide with Gel-Pak WF film, above the heating coil. The Gel-Pak film ensures ease of removing the cantilevers after the evaporation. Aluminum wire was wrapped around the heating coil, the evaporator bell jar was reinstalled and placed under high vacuum. By running a current through the heating coil, the temperature will reach the aluminum evaporation temperature. Because the evaporator is under high vacuum, evaporated aluminum atoms will have a long mean free path, and will not come into contact with other atoms before hitting the cantilevers. The aluminum then condenses on the exposed surface of the cantilever. For the mica cantilevers, the evaporation was run until approximately $200\,\mathrm{nm}$ of aluminum had accumulated.

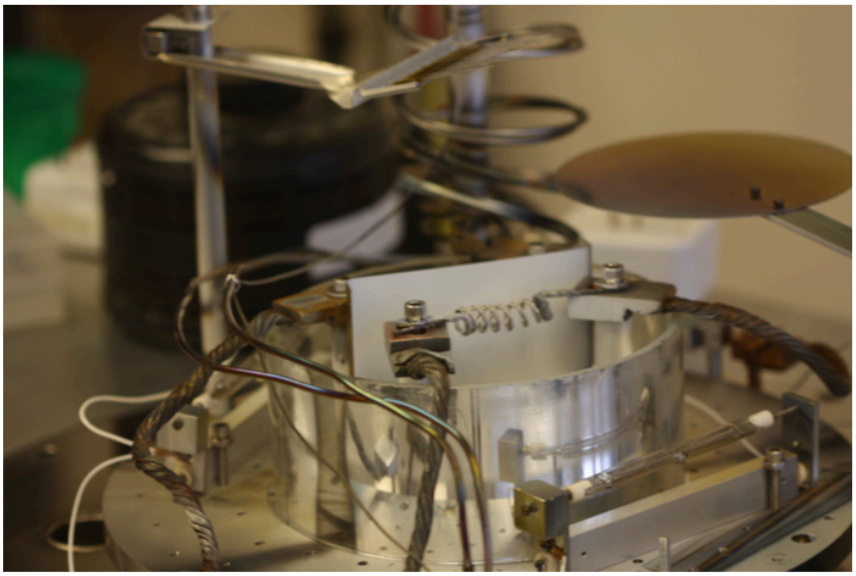

FIGURE 3.9: Photograph of the interior of aluminum evaporation chamber. A glass slide holder positions samples directly above a heating coil, onto which aluminum wire is wrapped. These interior components are contained inside a metal bell jar that is help under vacuum during the deposition. Taken from Ref. [122].

An Edwards AUTO 306 vacuum coater was also used to perform sputter deposition of aluminum onto the mica cantilevers. The mica cantilevers again were positioned on a glass slide with Gel-Pak film, which was then fixed to the sputtering table with screws and washers. Unlike evaporation, where atoms are heated until

they vaporize, sputtering uses gaseous ions to collide with a target of the deposition material. Impact of the gaseous ions causes the target atoms to isotropically eject from the target. Atoms that reach the sample surface, positioned opposite the target will coat the surface.

3.4.3 Spring constant measurement apparatus

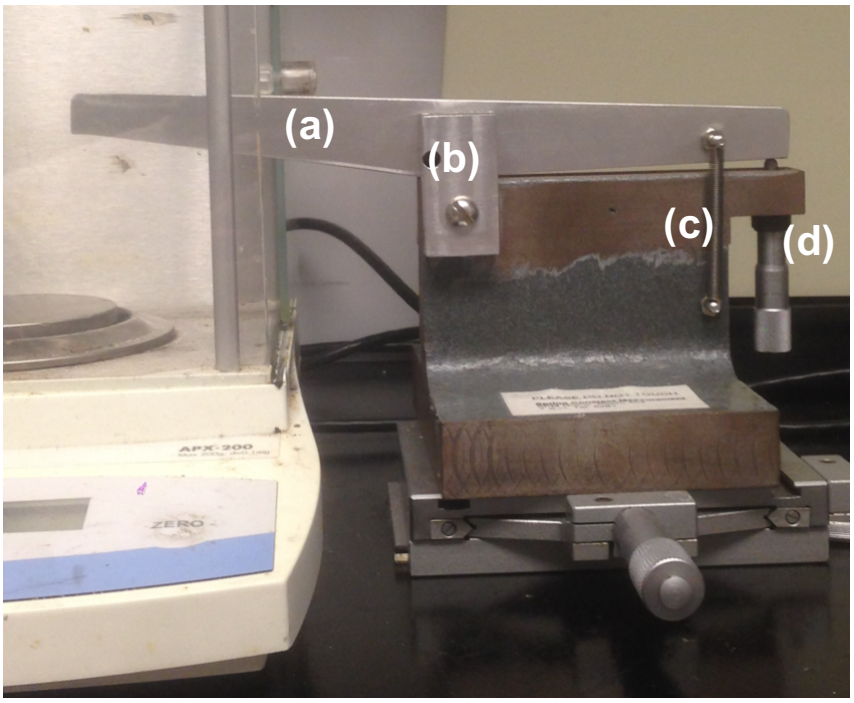

FIGURE 3.10: Apparatus for the determination of spring constant by Hooke's Law. (a) Lever arm; (b) pivot; (c) retaining spring; and (d) micrometer. The apparatus produces a known deflection in a cantilever. When the cantilever is mounted on a scale (shown on the left), the transduced force that corresponds to the deflection can be measured.

Figure 3.10 shows a photograph of a micrometer-manipulated lever arm designed for the purpose of producing small deflections in cantilevers. The lever arm is situated with one end free, one end pushing against the micrometer and a pivot in the middle. A pair of springs keeps the lever arm in contact with the micrometer at all times. When the cantilever is mounted on a support that is placed on a scale, the lever arm can produce a known deflection that is transduced to a force. The scale will measure this force, which, combined with the deflection can be used to estimate the spring constant of the cantilever, by Hooke's Law.

3.4.4 Deflection and electrochemistry measurements

An airtight electrochemical cell with optical access for a beam deflection system was designed to perform tests on the battery electrode cantilevers. The airtight requirement is due to the atmosphere sensitivity of non-aqueous lithium ion materials. Details of the design of this cell are discussed in greater detail in Chapter 5.

Figure 3.11 shows an image of this cell, in operation with a potentiostat and beam deflection system for electrochemical and stress measurements respectively. The battery electrode cantilever that resides inside the cell aligned with the laser and photodiode to facilitate deflection measurements, while it is in electrochemical contact with the counter and reference electrodes by way of the electrolyte and the externally connected potentiostat.

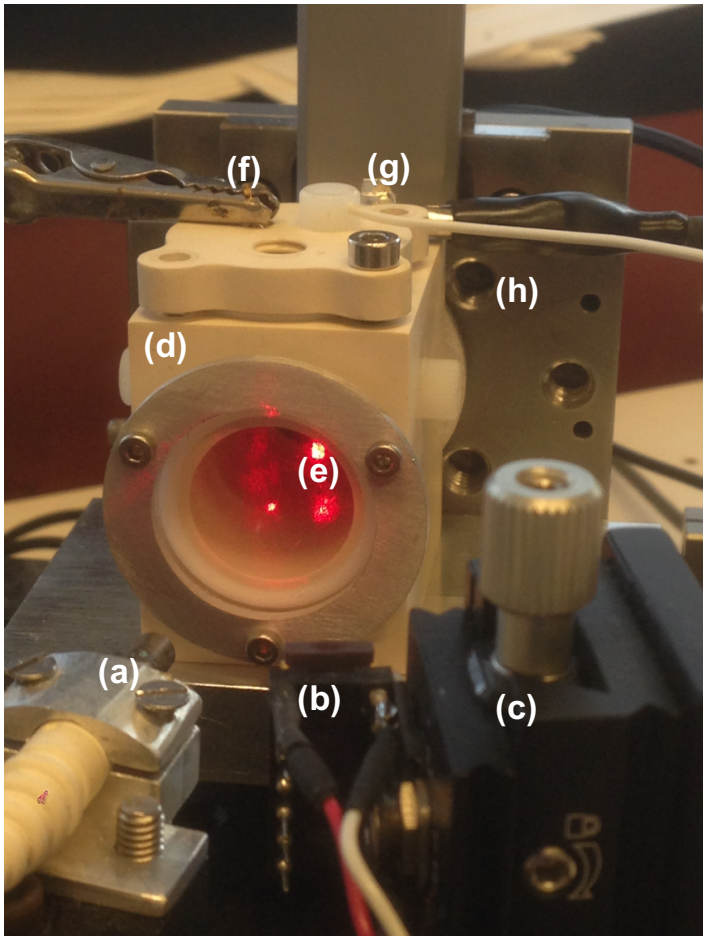

FIGURE 3.11: Apparatus for combined deflection and electrochemistry measurements. Deflection system comprised of (a) laser; (b) position sensitive photodiode; (c) three-axis translation stage controlling photodiode position. Electrochemical cell comprised of (d) chamber with optical access window; (e) a battery electrode cantilever, serving as the working electrode; (f) counter electrode; and (g) reference electrode. The electrochemical cell sits on (h) another three-axis translation stage to aid in alignment of the deflection system. Note that in this photograph, the cell is setup for measurements on an aqueous system.

In these experiments, an 8 channel, CH Instruments 1030A potentiostat is used. Figure 3.12 shows a circuit diagram of a potentiostat. It is operated simply by applying a potential at the counter electrode, and allowing current to flow between the working electrode and the counter electrode to change the potential of the working electrode. All potentials are measured relative to the reference electrode, which has a potential that is largely invariant over a large range of currents. In a three-electrode cell, the input impedance of the reference electrode is very large, so it is assumed to draw approximately no current. For these reasons, the potential of the reference is essentially constant.

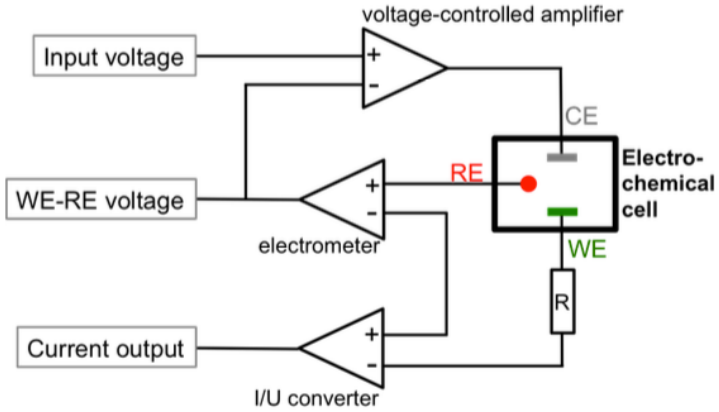

FIGURE 3.12: Circuit diagram of a potentiostat operating with a three-electrode electrochemical cell. The difference between input voltage and the voltage of the working electrode is applied to the counter electrode. Current flows between the counter electrode and the working electrode because of the potential difference between them. This current produces a voltage across the input resistance of the working electrode channel, which is converted to a measured current value. All potentials are measured relative to the reference electrode, which passes no current and therefore has constant potential. Taken from Ref. [106].

Chapter 4

Raman spectroscopy studies of $LiFePO_4$

4.1 Confocal Raman microscopy on $LiFePO_4$

Initial work in the study of the SEI by Raman spectroscopic techniques was Raman spectroscopy on virgin LFP. The rationale behind this being that, to measure the signal from a thin film that has grown on an electrode surface, one must know the signal from the electrode, to distinguish the signal solely from the film. Furthermore, initial experiments were perfect to compare with literature results to make sure that the techniques and materials were understood.

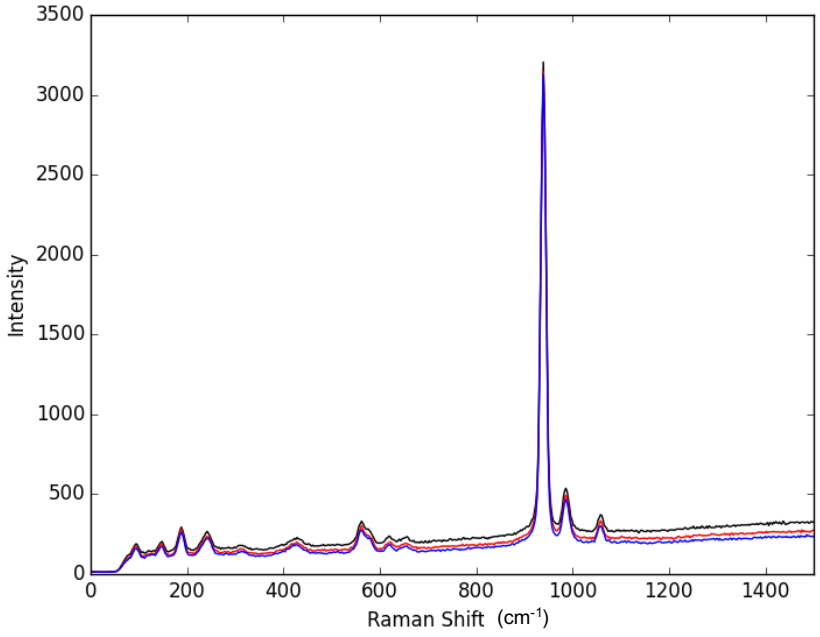

FIGURE 4.1: Raman spectra measured at three different points on the surface a polished piece of molten-state solid ingot $LiFePO_4$. The spectrum at each point is plotted in a different colour.

Figure 4.1 shows the measured Raman spectra on the polished molten-state solid

ingot $LiFePO_4$ introduced in Chapter 3. Using the work of Burba and Frech [49] as a reference from the literature, the measured spectra in Figure 4.1 behave exactly as expected. The tallest intensity band is reported at a Raman shift of $953\,\mathrm{cm}^{-1}$ with two nearby, but lower intensity bands at $999\,\mathrm{cm}^{-1}$ and $1071\,\mathrm{cm}^{-1}$. These bands, attributed to stretching modes of the PO_4^{3-}, are all clearly resolved in Figure 4.1 at essentially the same spectral location. Any small discrepancies in wavenumber can be easily reconciled because Raman scattering is strongly affected by the local atomic environment. A small difference in surface strain can cause changes in the Raman spectra of otherwise identical samples. Burba and Frech's measurements are performed on powdered LFP pressed into a pellet, while this measurement is performed on a solid ingot. Despite the differences in sample, there is no apparent difference in these three PO_4^{3-} stretching bands. At wavenumbers less than $700\,\mathrm{cm}^{-1}$ a number of low intensity scattering bands occur, which are all also measured by Burba and Frech.

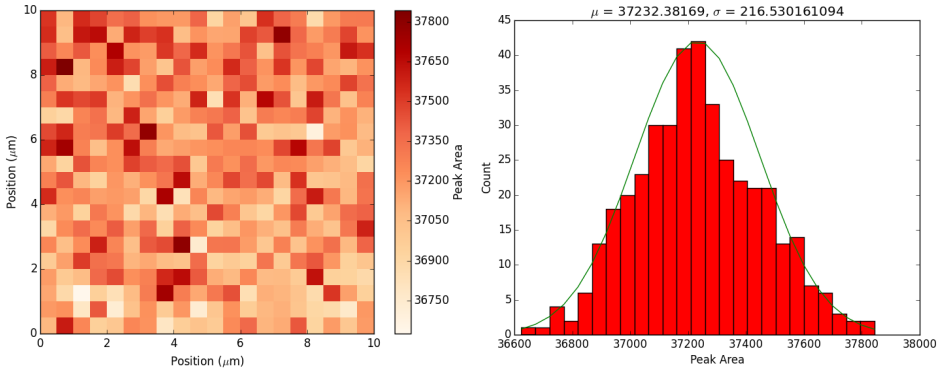

FIGURE 4.2: Raman map of the integrated intensity of the $953\,\mathrm{cm}^{-1}$ scattering peak from the surface of a molten-state solid ingot $LiFePO_4$ (left). Histogram of the distribution of peak areas in the Raman map, with a fitted Gaussian function.

Spectra of like those shown in Figure 4.1 were measured over a $10\,\mu\mathrm{m}$ x $10\,\mu\mathrm{m}$ area of the ingot surface, with a resolution of $500\,\mathrm{nm}$. The left panel of Figure 4.2 shows a map of the integrated intensity of the scattering peak located at $953\,\mathrm{cm}^{-1}$. As indicated by the scale bar, the variation amongst the pixels is relatively small, on the order of percent. There is no spatial ordering to the pixel colours either, suggesting the variations are not due to changes in local environment. The logical conclusion is therefore that any variation of the integrated peak across this surface is just an artifact due to measurement uncertainty or noise. Binning the distribution and plotting a histogram, shown in the right panel of Figure 4.2, reveals this to be true. The distribution is approximately Gaussian, indicating that the variation is not indicative of a change in the material over this $500\,\mathrm{nm}$ length scale. This makes sense because the material is thought to be of homogeneous composition. This result, while not particularly interesting is very useful in developing a foundation. Measurement of

the electrode surface should mean that delineation of Raman signals from the electrode and SEI would be possible.

4.2 Confocal Raman microscopy on Li_xFePO_4

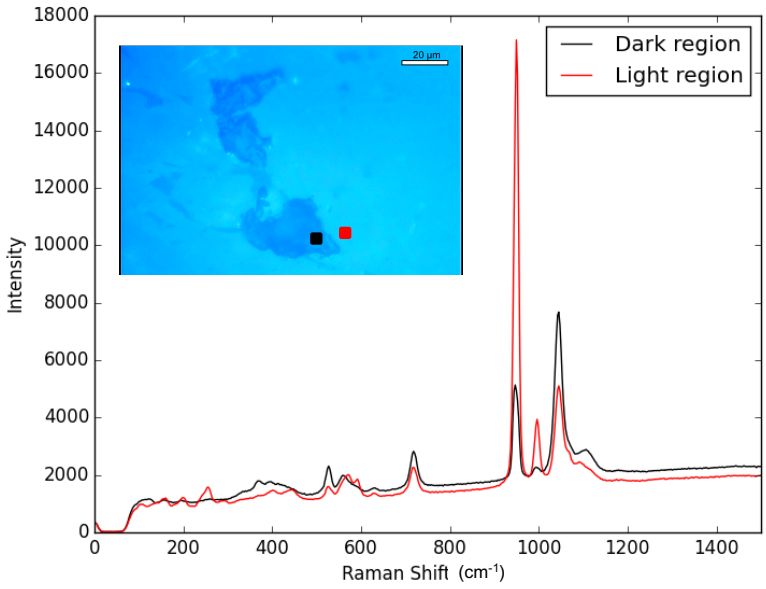

FIGURE 4.3: Raman spectra measured in optically different regions on a polished Li_xFePO_4 surface. The insert shows an optical image of the region of interest. The spectrum taken in the dark region, measured under the black dot in the insert, is plotted in black, while the spectrum taken in the lighter region, measured under the red dot in the insert, is plotted in red.

The follow up experiment to Raman mapping on $LiFePO_4$ was to perform the same measurements on a partially delithiated sample, Li_xFePO_4. In their measurements, Burba and Frech noted significant changes to the Raman spectra, particularly above $800\,\mathrm{cm}^{-1}$, as lithium was removed from Li_xFePO_4. In particular, they reported decreased intensity of the $953\,\mathrm{cm}^{-1}$ band, decreased intensity of the $999\,\mathrm{cm}^{-1}$ band and increased intensity of the $1071\,\mathrm{cm}^{-1}$ band. There is even observed peak splitting of the $1071\,\mathrm{cm}^{-1}$ band [49]. Figure 4.3 shows the Raman spectra from two visibly different regions on the Li_xFePO_4 surface, and an optical image indicating where the spectra were taken. The spectra for the lighter region, plotted in the red curve is very similar to the spectra shown in Figure 4.1. The characteristic phosphate stretching bands at $953\,\mathrm{cm}^{-1}$, $999\,\mathrm{cm}^{-1}$ and $1071\,\mathrm{cm}^{-1}$ are present, however the ratio of the peak heights indicates that the band at $1071\,\mathrm{cm}^{-1}$ is higher in Figure 4.2 than in Figure 4.1. There is also the emergence of a short, broad peak in the tail of the $1071\,\mathrm{cm}^{-1}$ peak. This is believed to be the $1124\,\mathrm{cm}^{-1}$ band measured by Burba and Frech, upon delithiation of LFP [49]. This comparison of the red curve in Figure 4.3 to Figure 4.1,

with references to literature, suggest that the light region where this spectrum was taken has less lithium concentration than $LiFePO_4$. That being said, as has already discussed, Raman spectra are sensitive to more factors than just local composition, so further testing to confirm the local lithium concentration would be useful.

The black spectrum in Figure 4.3 is taken in the darker region, indicated in the insert. Comparing it with the spectrum from the lighter region, there is significantly reduced intensity of both the $953\,\mathrm{cm}^{-1}$ and $999\,\mathrm{cm}^{-1}$ bands, while there is increased intensity from the $1071\,\mathrm{cm}^{-1}$ and $1124\,\mathrm{cm}^{-1}$ bands. Based on the results of Burba and Frech, these are the expected trends when reducing lithium content. That is, again, it appears by comparison of these spectra that the dark region may have lower lithium concentration than the adjacent light region.

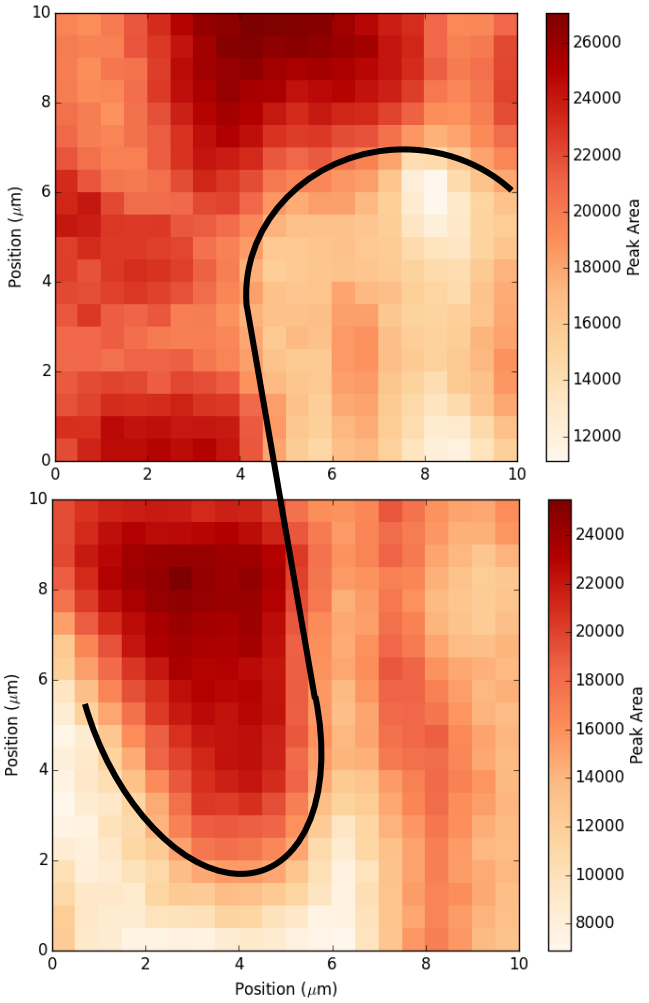

FIGURE 4.4: Raman maps of integrated peak area of the $953\,\mathrm{cm}^{-1}$ band, measured on the surface of polished, molten-state solid ingot Li_xFePO_4. The Raman maps cover adjacent areas and are lined up to accurately represent their real space orientation. The black curve is added to aid the eye in distinguishing the boundary of two apparent phases or domains.

This spatial variation in Raman spectra, perhaps due to variation of lithium concentration, naturally lends itself to performing spatial mapping of this sample surface. Figure 4.4 shows a pair of $10\,\mu\mathrm{m}$ x $10\,\mu\mathrm{m}$ Raman maps of integrated peak intensity of the $953\,\mathrm{cm}^{-1}$ band. The maps are acquired adjacent to each other, with $0.5\,\mu\mathrm{m}$ resolution. The positioning of the sample for these measurements was done very carefully and it should be stressed that these maps were taken next to each other. The boundary of one map merges almost perfectly into the next one. The location of these maps is different from the spectra in Figure 4.3. The region investigated here was of interest for correlation with other tests. There appear to be two distinct phases, one with large integrated intensity of the $953\,\mathrm{cm}^{-1}$ (the dark red region) and the other with lower intensity (pale orange region). A curve has been drawn to aid the reader in identifying the boundary of these apparent phases and illustrating the continuity of the phases from one map to the other.

The change in the $953\,\mathrm{cm}^{-1}$ band intensity would indicate the dark red region may be higher in lithium concentration, while the pale orange region would therefore have lower lithium concentration. All of the results reported here for this partially delithiated sample indicate that there are regions of varying lithium concentration, which seems perfectly reasonable. However, Raman scattering is sensitive to surface strains, contaminants, crystal orientation and many other factors. Without validation of the local concentrations by other techniques, any conclusions drawn about the lithium concentrations based on this work are speculative at most. That being said, the goal of this work was to use Raman spectroscopic techniques on spatially varying samples, and this demonstrates that, regardless of the cause of the spatial variation, reliable mapping of a surface can be done. Complementary work to confirm the local concentration could be performed in a number of ways, including atom probe, x-ray photoelectron spectroscopy (XPS) or Auger electron spectroscopy (AES).

4.3 Tip Enhanced Raman Spectroscopy on $LiFePO_4$

Given the success of performing confocal Raman microscopy on $LiFePO_4$ and Li_xFePO_4 samples, a TERS experiment was the next step. The sample prepared for TERS was LFP nanoplatelets on a template stripped gold surface. The small platelets would, in theory, allow the gold AFM tip to be very close to the gold substrate. In this case, phonon coupling in both gold materials can create further field enhancement and increase the occurrence of scattering events. This requires sub- monolayer coverage of the gold surface by the nanoplatelets. Figure 4.5 shows an AFM topography image, obtained in tapping mode, of the nanoplatelets on template stripped gold substrate, used to verify the sub-monolayer preparation. The features of interest are the two regions of raised topography in the bottom half of the image. The rightmost of these two is a single platelet, matching the expected thickness of approximately $15\,\mathrm{nm}$.

The other region contains a cluster of a few platelets. The height relative to the substrate is close to 30 nm, indicating that two layers of platelets exist. Furthermore, edges of at least two different platelets can be seen. From a TERS perspective, this sample is adequate. Ideal TERS conditions would be to find a single nanoplatelet, far from neighbouring particles. Even imaging on a few nanoplatelets would still be reasonable.

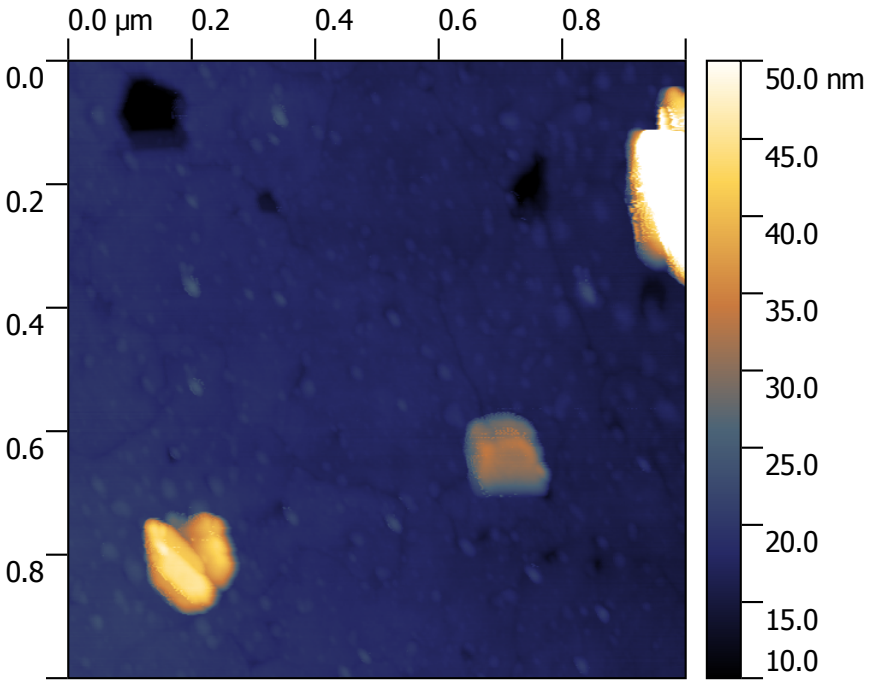

FIGURE 4.5: AFM topography image of etched colloidal $LiFePO_4$ nanoplatelets on a template stripped gold substrate, measured with Digital Instruments Nanoscope III. The colour scale is adjusted to prioritize contrast between the individual nanoplatelets and the substrate. The cluster in the top right therefore exceeds the colour scale.

An attempt was made to perform a tip-enhanced scattering measurement with the sample shown. With a suitable gold wire TERS tip, lateral force tuning fork AFM was performed to locate one of the nanoplatelets. Figure 4.6 shows the topography image obtained with a number of nanoplatelets found. The topography of the substrate and the edges of the nanoplatelets are less clearly resolved than in Figure 4.5. This is a result of using a tuning fork in lateral force mode, when compared to a cantilevered tip in tapping mode. Furthermore, the gold tips are susceptible to damage because they are very soft, which can reduce their imaging capabilities. Nevertheless, Figure 4.6 shows that individual nanoplatelets were able to be found on the substrate using AFM. Immediately following the acquisition of this image, a point spectrum on a platelet, followed by a two- dimensional mapping were attempted by TERS. Prior to performing AFM and searching for nanoplatelets, the Raman laser was aligned to the gold tip, where a LSPR was excited. When TERS was attempted after AFM, the LSPR was no longer excited and efforts to realign the laser to find a

LSPR were unsuccessful. As such, a TERS signal was unable to be obtained. Further attempts with new tips produced similar results, with the LSPR disappearing after AFM imaging. It is believed that the process of imaging with lateral force AFM damages the tip or at least modifies its shape. As discussed in Chapter 2, excitation of a LSPR is highly dependent on geometry, which would explain why damage to the tip would eliminate the LSPR.

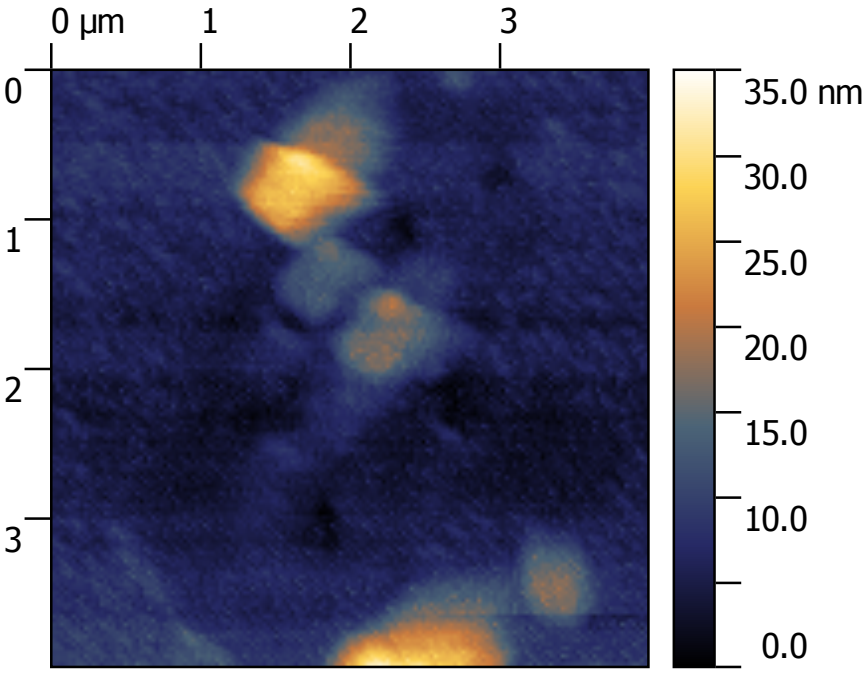

FIGURE 4.6: Lateral force AFM topography image of the $LiFePO_4$ nanoplatelets shown in Figure 4.5. This image was taken with the TERS-capable AFM at INRS-EMT.

Figure 4.7 shows another topography image of the LFP nanoplatelets obtained by lateral force tuning fork AFM. Structures that may be nanoplatelets are observed, however they exist in the image with considerable shadowing and/or smearing effects in the direction of the fast scan axis. This is caused by the fact that at the edge of a platelet, the AFM tip must quickly transition from the top of the platelet to the surface of the substrate. If the tip cannot do this much faster than the lateral speed of the scanner, it will gradually move down to the substrate as the scanner moves on. The tip can be thought of as gliding to the surface when it would ideally contact the surface immediately. This causes the shadowing effect. While this causes artifacts in the image, it can also indicate that damage is being caused to the tip. Consider the opposite scenario, of the tip scanning along the substrate and eventually reaching the edge of a nanoplatelet. It must lift off the substrate to the height of the nanoplatelet in a very short lateral distance. If it cannot do this faster than the scanner is moving, the tip will crash into the side of the nanoplatelet. It is believed the inability to control the tip position via the feedback systems is causing the tip

crash into raised topography and sustain damage. This is largely exacerbated by using lateral force imaging. With this problem, the ability of these tips to perform AFM is diminished, and in turn the damage seems to destroy any LSPR which prevents successful TERS measurements.

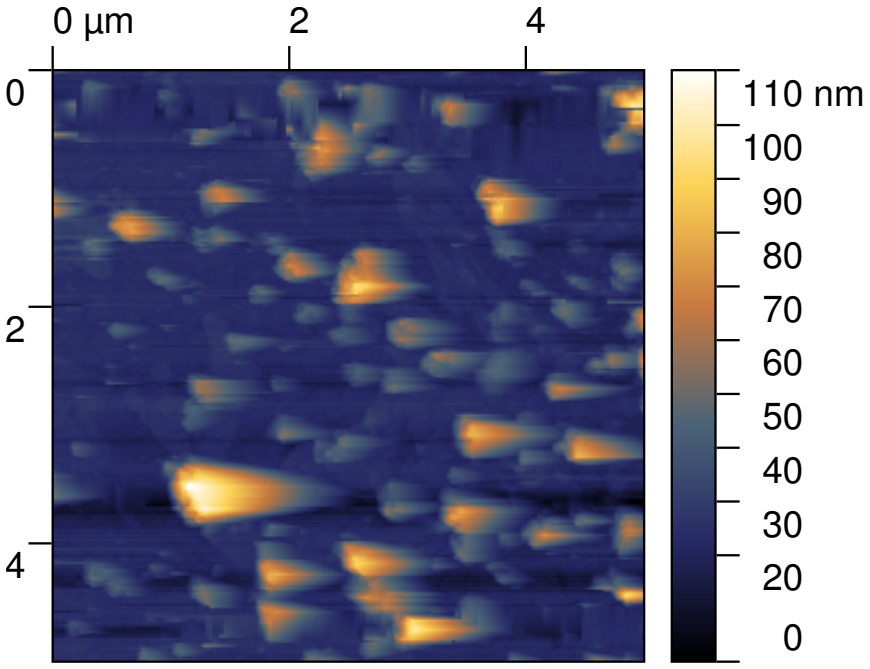

FIGURE 4.7: Lateral force AFM topography image of the $LiFePO_4$ nanoplatelets shown in Figure 4.5. This image was taken with the TERS-capable AFM at INRS-EMT

This is a continual challenge for those developing TERS microscopes and tips. The field enhancement from a LSPR is highly localized, meaning the tip must be very close to the sample utilize the enhanced field. For this reason, lateral force imaging is thought to be superior. Any deflection of the tip in a cantilevered system or one that measures normal forces would move the tip relative to the excitation laser, perhaps destroying the LSPR. Tapping mode with a cantilever is seemingly impractical for similar reasons. However, topography measurements are considerably easier with these AFM modes. The group at INRS-EMT is among the leading experts and pioneers of the TERS field. The success rate of their tip fabrication is less than 5%, where successful tips can show a localized surface plasmon response. The tips that can perform AFM or show a TERS signal are even fewer. The goal of this work with TERS was to eventually implement the technique in liquids for *in situ* imaging of SEI growth. Measurements in liquids with AFM, and implementing Raman spectroscopy in liquids are challenges in their own right. The unreliability experienced with TERS, over many attempts and many tips, indicates that the technique is currently too immature for it to be used in the manner originally intended for this project. Development of tip fabrication processes is required, and perhaps integration within the microscope should be revisited. Much of this work is beyond

the scope of this project, and the goal of performing *in situ* TERS was abandoned. Once better *ex situ* reliability has been demonstrated, there is no reason why *in situ* TERS should not be achievable. It will however be in the future after many years of work, beyond the length of this project.

Chapter 5

Development of battery electrode cantilevers

5.1 Fabrication of cantilevers from $LiFePO_4$ ingot

Initial attempts to fabricate a cantilever sensor from a battery material used the molten-state solid $LiFePO_4$ introduced in section 3.1.1. The idea was that a piece of ingot could be cut and thinned to produce a cantilever with reasonable spring constant. This would be a few millimeters in lateral dimensions and up to a couple of hundred microns in thickness. A $0.5\,\mathrm{mm}$ slice was cut from the ingot using the diamond saw, following methods in section 3.4.1. The slice was then polished to gradually decrease the thickness. It was estimated that achieving a thickness of $150\,\mu\mathrm{m}$ or less was required to produce cantilevers with a spring constant that was low enough to provide sufficient stress sensitivity.

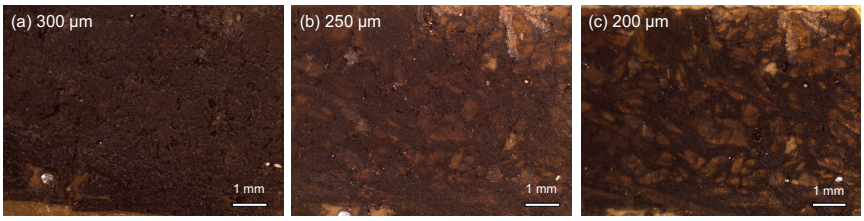

FIGURE 5.1: Stereo microscope images of a polished slice of molten-state solid ingot $LiFePO_4$ taken at different thicknesses.

Figure 5.1 shows stereo microscope images of the LFP at various thicknesses. The series of images illustrates that as the sample was thinned, structural integrity was compromised. Even before mounting the sample on the polishing disk, it was observed that the sample was very brittle. Figure 5.1a shows that the sample is porous and polycrystalline, with easily observable grains. The yellowish appearance of many of the grains in Figure 5.1b is due to the fact that these areas have been thinned enough that the mounting wax used beneath the sample is visible. That is, the porosity and thinness of some grains was such that very little material remained in those particular areas, or they were thin enough to become transparent. This occurred to an even greater extent once the thickness was reduced to $200\,\mu\mathrm{m}$,

as shown in Figure 5.1c. Despite not reaching the target thickness, this sample was removed from the polishing block at this point to attempt cutting into rectangular cantilevers. Removal of the polished sample was performed by dissolving the wax with trichloroethylene. Chemical means of removal was thought to be the gentlest option available. When the wax dissolved, it was realized that it had been providing significant structural reinforcement. What was left of the LFP was essentially crumbled or almost a powder with very large particles. It was realized that the brittle, porous and polycrystalline nature of the ingot did not lend itself to being cut into a cantilever. If single crystal LFP of a few millimeters size could be obtained, this approach would be more successful.

5.2 Fabrication of mica cantilevers

5.2.1 Diamond saw cutting

A diamond saw was used to cut mica sheets into rectangular cantilevers. Previous work by other students suggested that mica is too fragile to be cut by a diamond saw while preserving lamination of the layers and leaving clean edges. Nevertheless, diamond saw cutting was performed to test the technique in this work, and to set a baseline from which to improve using other cutting methods. Figure 5.2 shows a stereo microscope image of a mica slide cut by diamond saw. The left edge in panel (a) was an edge that was cut by the manufacturer, while the right edge was cut by the diamond saw. Delamination of the layers, evidenced by the bubble-looking features that propagate inward from the edge, is far more pronounced at the edge cut by the diamond saw.

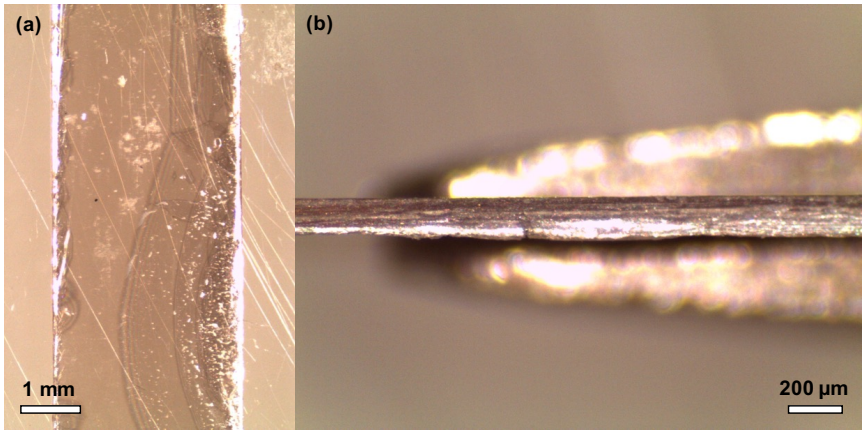

FIGURE 5.2: Stereo microscope images of mica sheet cut by diamond saw. Image (a) shows a view normal to the surface. The edge on the right is cut by the diamond saw, while the left edge is cut by the manufacturer using a punch. Image (b) shows an edge-on view of the cut made by the diamond saw.

Delamination of the layers is troublesome because it reduces the mechanical integrity of the cantilever. When the mica bends, typically the internal bonding between the layers overcomes the rigidity of the individual layers. As such, the layers remain together and the mica bends as a whole. When partial delamination has occurred, the collective strength of the bonds between the layers is weakened. Bending the mica then typically causes some layers to bend, but some of the surface layers remain straight. This pulls the layers apart even further and worsens the delamination. It is also liable to produce incorrect transduction of force or stress when the mica is used as a cantilever. Figure 5.2b shows an edge-on view of the cut made by the diamond saw. The layers of the mica are visibly splayed and the bottom of the edge has a ripple to it. This is further evidence of the delamination. As suspected, the diamond saw is not gentle enough to cut the mica without causing significant damage, beyond the point where it can still be a good cantilever.

5.2.2 CO_2 laser cutting

Infrared laser cutting is a non-contact cutting technique. It was believed that contact cutting methods may be too harsh to properly cut mica into cantilevers, and that laser cutting may provide even better results than wire saw cutting (see section 5.2.3). With even low laser powers, it was found that the laser essentially destroyed the mica. With 10% power of a maximum $60\,\mathrm{W}$ pulsed laser, samples would catch fire during the cutting procedure and by the end of the process were significantly charred. Figure 5.3 shows the best results that were obtained, using the lowest laser power (1%) that is programmable in the laser cutter control software. Despite being the best results, they are wholly inadequate. The two opaque stripes in the image are where the laser passed over the surface. The laser ablated region did not penetrate entirely through the mica sheet, so the cut rectangles are held together by an incredibly thin mica layer. At the edges of the cuts, there is material build up, almost as if material in the cut region was pushed outward. Most troubling, however, is the damage to the mica in the regions where the laser did not pass over the surface.

This region is no longer optically transparent, but has gained some reflective and refractive characteristics, while the surface topography appears crumpled. It is believed that is due to the fact that the focusing optics in the laser cutter cannot produce a small enough spot size for the small dimensions being cut. Discussions with Erika Janitz, a PhD student at McGill and an expert in infrared laser ablation, revealed that laser ablation is highly non-linear and the energy threshold for ablation is very sudden. If a laser profile is Gaussian, the portion of the profile that has sufficient intensity to ablate the mica may only be a narrow section at the centre of the beam. This would mean that the majority of the laser profile is not capable of ablation, and in essence there are large regions that will only heat up the sample. Because mica is an insulator, it cannot dissipate this heat. Excessive heating will deform the layers and may cause the damage shown in Figure 5.3. This laser cutter has a $610\,\mathrm{mm}$ x $915\,\mathrm{mm}$ lateral working area and is designed to cut parts much larger

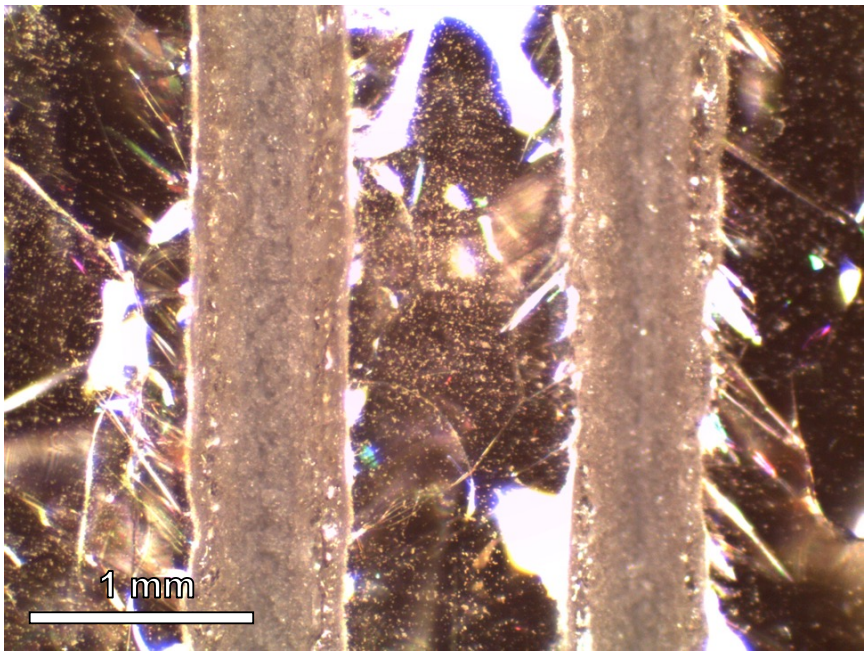

FIGURE 5.3: Stereo microscope image of mica cut by infrared CO_2 laser. Note that the cut did not entirely go through the mica sheet.

than $1\,\mathrm{mm}$ wide cantilevers. For a larger part, made of thicker and more robust materials, a poorly focused beam is of little consequence. There will be less chance for damage and the extent of the damaged region, if it exists at all, is likely to be only 1% of the size of the part or smaller. Upgrading the optics on the laser cutter was briefly investigated, but after receiving a number of quotes and no guarantee the upgrades would satisfy the needs of this project, it was decided to utilize another technique.

5.2.3 Wire saw cutting

Use of wire saw cutting to fabricate mica cantilevers was initially investigated prior to laser cutting. Wire cutting is gentler, but slower when compared to cutting with a diamond saw. Figure 5.4 shows stereo microscope images of a mica cantilever cut by the wire saw that was amongst the initial set of results. The most striking feature of these images is that the mica cantilever, which is normally transparent, is opaque and black. Furthermore Figure 5.4b shows that the cantilever edges have been severely delaminated and the cantilever has even undergone some bending. For many of the same reasons discussed in section 5.2.1, this was completely unacceptable for a useful cantilever. However, it was found through considerable trial and error that with preparation and technique improvements, these undesirable effects could be eliminated.

The blackening and the delamination in Figure 5.4 are due to the same cause. The wire saw makes cuts by using a wire to carry an abrasive boron carbide slurry across the surface of the mica. If the sample mounts and work arm of the saw are set up

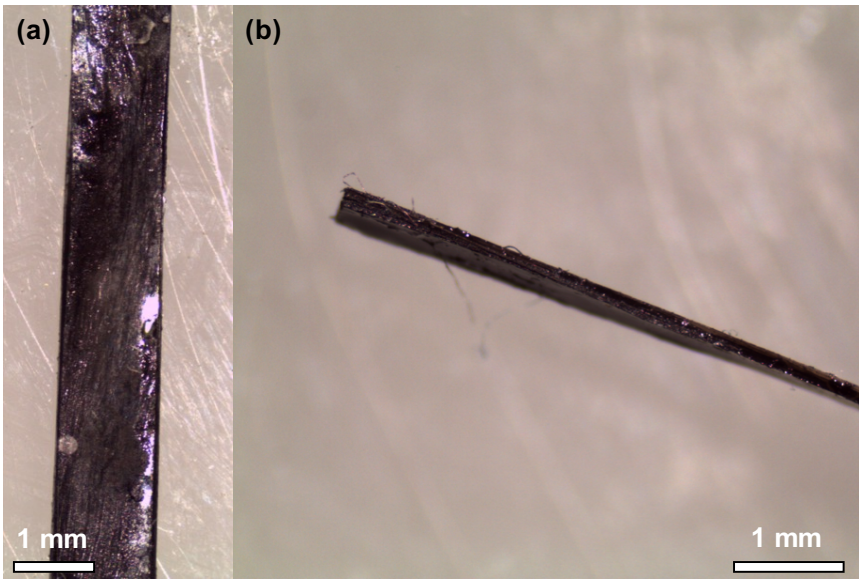

FIGURE 5.4: Stereo microscope image of mica cut by wire saw. Image (a) shows a view normal to the surface. Image (b) shows an edge-on view of the cut made by the diamond saw.

so that the surface of the mica is not perfectly parallel to the wire when they make contact, there will be out-of-plane forces acting on the mica. If the angle between the wire and the mica surface is large enough, the cut takes longer and therefore there is considerable rubbing of the wire against the mica layers in a direction that has out-of-plane components. This continual rubbing exfoliates the mica layers at the edge, causing them to delaminate. This exfoliation creates space for the boron carbide slurry to move between the layers at the edges, and eventually penetrate throughout, given enough time and delamination.

The solutions to this problem is two-fold. Firstly, the sample block, where the mica is mounted, is shimmed to ensure the wire and the mica surface are as parallel as possible. Even with this extra step, the cut still progresses from one edge of the mica to the other, so there are small angles between the mica and the wire that are unavoidable. To prevent damage, when the mica is mounted to the sample block, instead of applying mounting wax only to the backside of the mica, the mica is fully encased in wax. This constrains the layers, preventing them from moving, and minimizing any edge exfoliation. Figure 2.5 shows a stereo microscope image of a mica cantilever cut with these precautions taken. Comparing the left and right edges, which are cut by the manufacturer and the wire saw respectively, their quality is very similar. Neither show much if any delamination around the edges. The cantilever surface appears imperfect, because there is white speckling and streaks. These are due to wax residue and scratches on the microscope stage below, respectively. The residue was removed before metal coating.

Fully encasing the mica in wax was the breakthrough that allowed cutting of the mica without significantly damaging it, however, it does have some drawbacks.

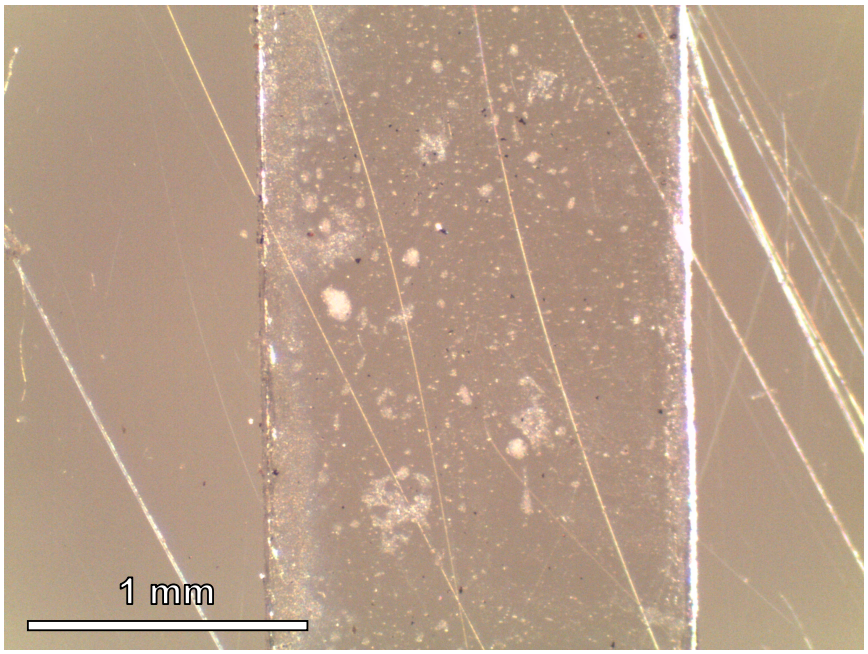

FIGURE 5.5: Stereo microscope image of a mica cantilever cut by wire saw, while fully encased in mounting wax. The left edge is a manufacturer cut edge, made by punching, while the right edge is cut by wire saw. The speckling on the surface of the mica is simply residue of mounting wax, and white streaks are on the microscope sample stage.

The wax used to encase the mica was selected because it is very hard, and would therefore provide the most rigid hold on the layers. This results in added material that is even harder than the mica that has to be cut through. The mica cantilevers are only $50\,\mu\mathrm{m}$ thick, while the top layer of wax is close to a millimetre thick in places. This extends the amount of time spent making a single cut. Before covering with wax, cuts would take a matter of minutes, but after, a single cut could take up to two hours. The layer of wax on top of the mica had unpredictable and uncontrollable topography. The melted wax would wet the surface if it was hot enough, but the primary means of spreading it over the surface was under the flow of air from a heat gun. The wax surface was therefore created with a number of peaks and valleys. The first effect of this was to change the path of the wire when cutting. Often times the wire would shift slightly to fit around the larger bumps on the wax surface. All of the cantilevers cut still appeared to be rectangular, but their widths would vary noticeably despite the space between cuts being set precisely by a micrometer. The second effect is related to the time duration of cuts. In regions with thicker wax, cuts would take longer (i.e. up to two hours) but in regions with a thin covering of wax, cuts could be as fast as 20 minutes. This led the necessity of constantly checking progress, which ends up being wasted time if a cut takes two hours.

5.3 Effect of geometry and metal layer on cantilever spring constant

The spring constant of a cantilever essentially determines its stress sensitivity according to Eq. 2.11. All three geometrical parameters of a rectangular cantilever play a role in the resultant spring constant, as shown in Eq. 2.10. One of the advantages of mica is that geometry is easily controllable for spring constant tuning. The lateral dimensions can be controlled during the cutting process, and the thickness can be controlled by cleaving molecular layers off. Figure 5.6 shows a graph of the measured spring constant versus the width for a complete batch of mica cantilevers, cut from a single cleaved sheet. The width is plotted because it is the only parameter that significantly varies among the cantilevers. The reason for this variation is discussed in section 5.2.3. The spring constant is expected to depend linearly on width, and the plotted line in Figure 5.6 represents the predicted value based on the geometry of the cantilevers. Two measurements of spring constant were made, before and after being coated with a metal current collector. A third measurement would have been made after coating with the battery material slurry, but it was found that the test required physical contact with the battery material which caused damage to it. The spring constants are on the order of single N/m. The distributions of spring constants both before and after coating are essentially scattered. There is no trend in width that follows a similar slope to the predicted line. Furthermore, if coating with metal significantly changed the elastic properties of the cantilever, it would be expected that the spring constants for before and after coating would have some vertical offset in Figure 5.6. The fact that the two distributions are intermingled and visually indistinguishable, indicates that the metal coating does not cause significant changes to the spring constant. This is expected because the thickness of the metal is on the order of $100\,\mathrm{nm}$, while the thickness of the cantilever is $50\,\mu\mathrm{m}$.

One of the reasons for the scatter in the measured values, even at nearly identical widths, is limitations of the measurement. It is sometimes difficult to position the lever used in spring constant measurements exactly at the end of the cantilever, in the centre, applying force directly downward. There are cases where the lever slips ever so slightly against the surface of the cantilever which would produce inaccurate deflection measurements. Lastly, the scale used to measure the force would not read a constant value, even beyond waiting for 5 minutes. The reading on the scale slowly, but regularly drifts for a long time. The best solution to this was to take measurements at a consistent time interval after applying the deflection, but this does not truly eliminate the problem.

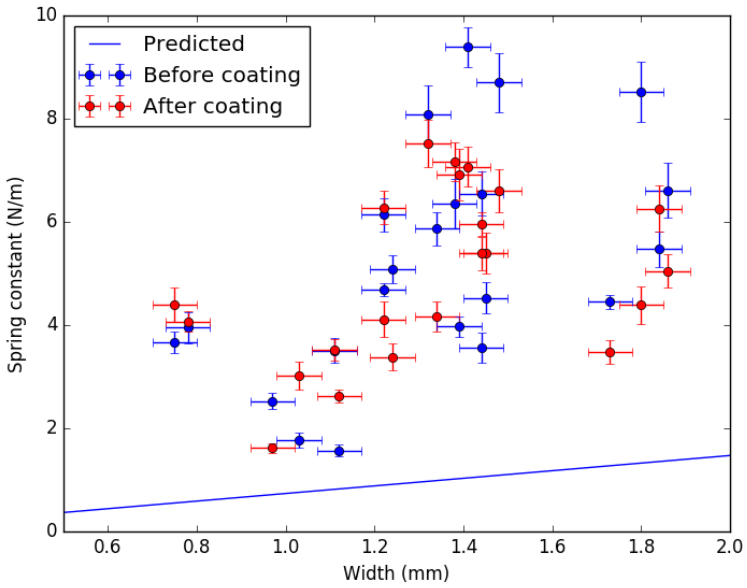

FIGURE 5.6: Measured spring constant as a function of width for mica cantilevers before and after coating with a metal layer. The line represents the predicted value based on the geometry of the cantilevers and the Young's modulus of mica, according to Eq. 2.10.

5.4 Design of an airtight cell for electrochemically induced stress measurements

An airtight electrochemical cell was required to test battery materials that are oxygen and water sensitive. The cell needed to be easily assembled in a glove box, while providing electrical and optical access to the battery electrode cantilever contained within. Figure 5.7 shows a schematic of the cell that was designed. The design was undertaken in collaboration with Andreas Spielhofer. The design showcased in Figure 5.7 was the final result of a number of iterations. The main body and cantilever holder are made of polyether ether ketone (PEEK). PEEK was chosen because it is electrically insulating and inert towards most chemicals. Electrical insulation is required because there are a number of feed through wires that must not short circuit. A metal or otherwise conducting body would increase the chance of a short occurring. The cantilever holder has a copper clamp that serves as both the mechanical structure that holds the fixed end of the cantilever, as well as electrical contact to the cantilever. The cantilever holder is secured to the body with four stainless steel screws, and is fastened over a polytetrafluoroethylene (PTFE) ring that creates a seal. Glass microscope slides are cut down to a reasonable size and serve as optical windows into the cell. They are fastened using four stainless steel screws that anchor an aluminum retaining ring. The ring presses the glass evenly into a PTFE ring, thus creating a seal. Homemade feedthroughs for all connections were designed for easy and economical fabrication. The design utilizes nylon screws with a small hole

drilled through the centre of the screw. A wire or thin plastic tube feeds through this hole and secured on both ends using Eccobond 286 epoxy. The epoxy conveniently holds the wire or tube but also seals the drilled hole. The threads of the screws on these feedthroughs are wrapped with PTFE tape.

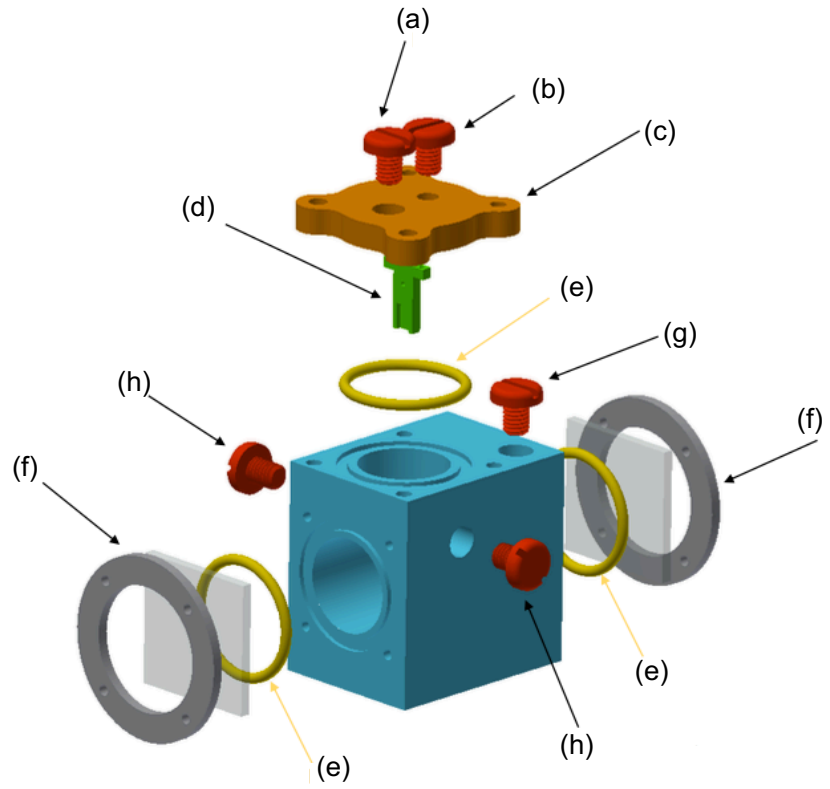

FIGURE 5.7: Schematic of the airtight cell for combined electrochemistry and stress deflection measurements. Pieces are: (a) nylon screw with feedthrough wire for cantilever; (b) nylon screw with feedthrough plastic tube for argon outlet; (c) base of cantilever holder; (d) cantilever holder (not shown is copper clamp); (e) polytetrafluoroethylene o-ring seal; (f) Glass slide with aluminum retaining ring for optical access; (g) nylon screw with feedthrough plastic tube for argon inlet; (h) nylon screw with feedthrough wire for counter/reference electrodes. The main body of the cell, cantilever holder and cantilever holder base are made of polyether ether ketone. Schematic adapted from Andreas Spielhofer.

5.5 Electrochemistry and deflection measurements

Combined measurements of electrochemistry and stress-induced deflection were attempted. Initially, the experiment was to be attempted using 1M $LiPF_6$ electrolyte in EC/PC and lithium metal counter and reference electrodes. This required assembly of the electrochemical cell be completed under an inert atmosphere to avoid reaction of lithium metal and the electrolyte with oxygen and water, namely, an argon-filled

glovebox. Unfortunately, the glovebox and the vacuum pump that serviced the box sustained damage during other activities that compromised the atmosphere inside the box. To continue with measurements, a switch was made to an aqueous electrolyte. Due to unfamiliarity with aqueous battery measurements, the desire was to simply reproduce some of the results from Wang *et al*. [120], using a battery electrode cantilever, while measuring deflection.

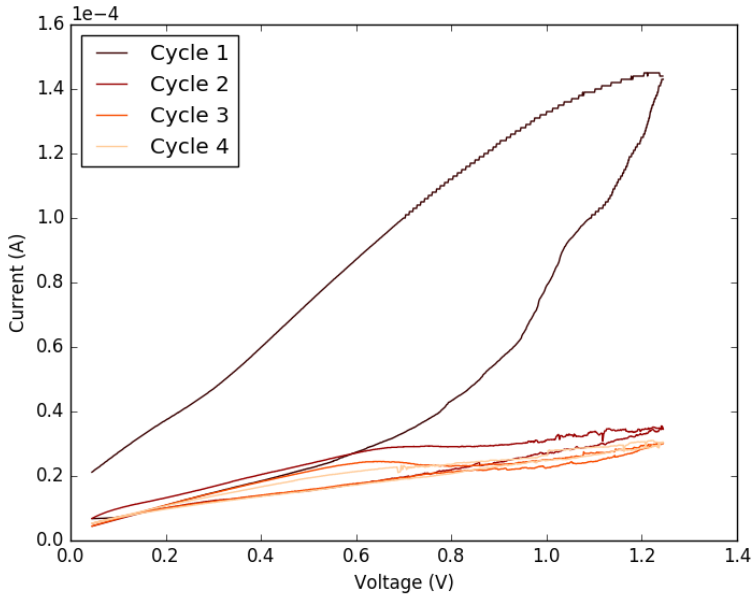

FIGURE 5.8: Cyclic voltammogram of a $LiFePO_4$ coated battery electrode cantilever in 1M Li_2SO_4. Potential was scanned from $0.045\,V$ to $1.245\,V$ at a rate of $5\,mV\,s^{-1}$. Potentials versus an Ag/AgCl pseudo-reference.

Figure 5.8 shows the electrochemistry from one of these very attempts to reproduce the work of Wang *et al*. This cantilever was coated with LFP as the active component in the battery material layer. The CV shown in Figure 5.8 does not resemble any literature results for LFP. Further evidence of something wrong is that the current is positive throughout the entire CV. This indicates that the reaction measured is only occurring in the forwards direction. During the positive direction of the scan, the forward reaction should begin at sufficient overpotential, and consume reactants until their concentration runs out. The charge transfer associated with this forward reaction causes the positive current. As the potential scans towards negative values, that product gets converted back to reactant if the backwards reaction can occur. This should produce a negative current, because charge transfer occurs in the opposite direction. Because no negative currents are measured, the reaction occurring is irreversible, or the potential window is not wide enough to activate the reverse reaction. The potential window, $45\,mV$ to $1.245\,V$ versus Ag/AgCl pseudo-reference, is the range chosen by Wang *et al*. because this corresponds to the potential range seen by the positive electrode in a Li-ion battery, although normally referenced to Li^+/Li.

Widening the potential window therefore makes no sense in the context of batteries. The potential window used in this work, versus Ag/AgCl pseudo-reference exactly matches that used in the work by Wang *et. al.*, also referenced to Ag/AgCl pseudo-reference. Given that LFP can react reversibly in aqueous electrolyte in batteries, and that reversible reaction is not observed here, it seems that lithium is not being removed from the LFP and another reaction is occurring. The large signal that is seen on the first cycle is greatly diminished in subsequent cycles. This indicates that, for this reaction, reactants are running out, or are becoming inaccessible, as would be the case with some kind of surface passivation. It is not believed to be due to depletion of the electrolyte because repeated tests with fresh battery electrode cantilevers in the same electrolyte yielded similar results.

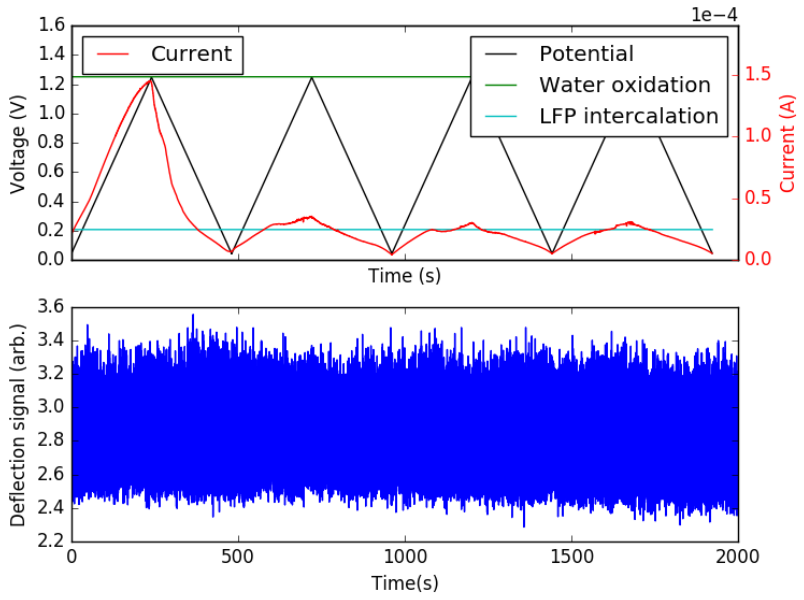

FIGURE 5.9: The top panel shows voltage (versus Ag/AgCl pseudo-reference) and current plotted as a function of time for the cyclic voltammogram of an $LiFePO_4$ battery electrode cantilever shown in Figure 5.8. Redox potentials for the oxidation water in aqueous Li_2SO_4 solution (at pH = 7)[123] and intercalation of Li in $LiFePO_4$ are also shown for reference. The bottom panel shows the simultaneously acquired deflections signal. The deflection signal is a scaled photodiode voltage.

Despite the fact that the observed electrochemistry did not match expected results from the literature, deflection was also measured. Figure 5.9 shows the potential, current and deflection signal as a function of time for the CV shown in Figure 5.8. The potential shown is simply the CV potential waveform. The horizontal lines indicates the potential at which intercalation of lithium into $LiFePO_4$ should occur, and oxidation of water at pH = 7 should occur. The onset of current does not correlate with the times that the applied potential crosses the intercalation potential, which is another indication that desired insertion and removal of lithium is

not occurring. The linear form of the current matches the linearly varying potential waveform, which indicates a large resistive current contribution to the signal.

The deflection signal appears to consist of only noise, or at least there is no signal correlated with the CV that is above the noise floor. Testing with many other cantilevers revealed the same results. A possible cause is that the reaction occurring does not produce a stress response, or the cantilever is too stiff to transduce the stress that is produced. In other words, the cantilever may not be sensitive enough. The deflection signal shown in a Figure 5.9 is the photodiode voltage scaled by a factor that should correspond to linear deflection. The scaling factor is not calibrated for these cantilevers and would require recalibration every experiment because they have slightly different geometries, spring constants and require slightly different alignment of the deflection system. This would, however, be worth pursuing if the deflection signal of any of the cantilevers had shown any response.

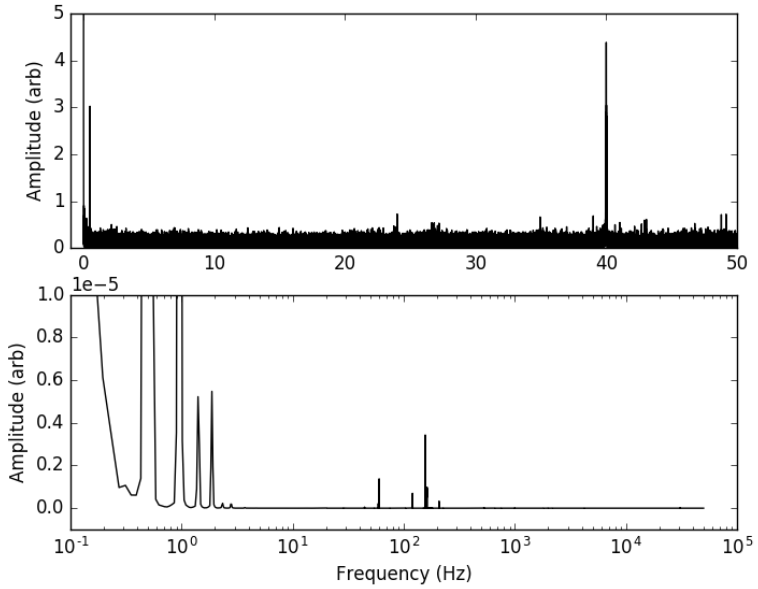

FIGURE 5.10: The top panel shows the absolute values of the Fourier transform of the deflection signal in Figure 5.9. Frequency is plotted on a linear scale. Data was collected at $100\,\mathrm{Hz}$ sampling rate. The bottom panel shows the noise spectrum of the system, measured by a response analyzer. Frequency is plotted on a logarithmic scale

To confirm that the deflection signal contained only noise, Fourier analysis of the measured data was performed. The top panel of Figure 5.10 shows the Fourier amplitudes in the data, while the bottom panel shows the noise spectrum of the cantilever and deflection system as measured by a response analyzer. In both, the most predominant feature is low frequency, $1/f$ noise. The peaks at low frequency are believed to be due to the data acquisition electronics and, in the case of the noise spectrum, the interaction of those electronics with the mechanical vibrations. Line noise is also observed at multiples of $60\,\mathrm{Hz}$ in the noise spectrum. Despite the noise,

it should not be terribly limiting if an actual stress response was measured. The noise corresponds to variations of single millivolts on photodiode segments that are measuring single volts. Furthermore, low-pass filtering techniques would help reduce the measured noise. Only the DC response is important in these measurements, as one CV takes $480\,\mathrm{s}$, most frequencies greater than a few Hz could be rejected.

While the deflection did not yield any meaningful result, further work was done to determine why measured CVs did not match literature results. Cantilevers were made with both $LiFePO_4$ and $Li[Ni_{1/3}Mn_{1/3}Co_{1/3}]O_2$ (NMC) coatings. They were expected to have different responses, in that LFP should cycle reversibly, while NMC has been shown to be unstable in aqueous electrolyte [120].

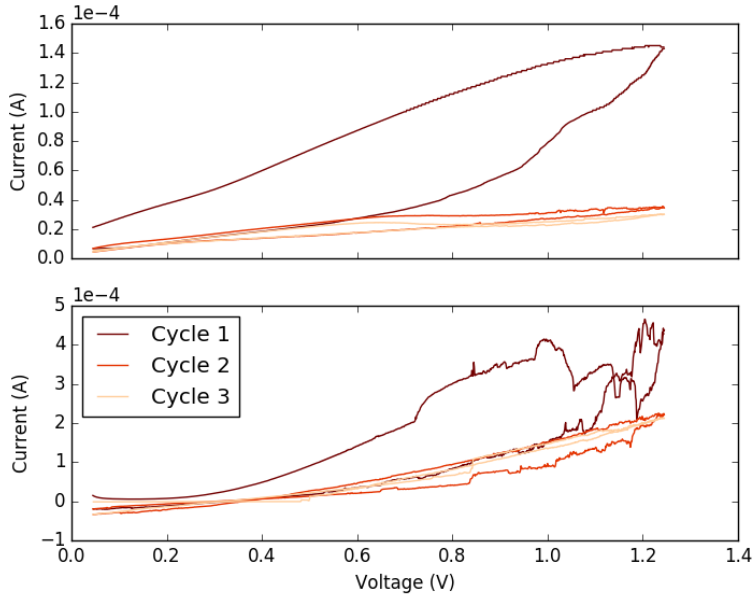

FIGURE 5.11: Cyclic voltammograms of $LiFePO_4$ (top) and $Li[Ni_{1/3}Mn_{1/3}Co_{1/3}]O_2$ (bottom) coated battery electrode cantilevers in 1M Li_2SO_4. Potential was scanned from $45\,\mathrm{mV}$ to $1.245\,\mathrm{V}$ at a rate of $5\,\mathrm{mV\,s^{-1}}$. Potentials versus Ag/AgCl pseudo-reference.

Figure 5.11 shows two CV, comparing a LFP coated cantilever to a NMC coated cantilever. Neither of these matches the CV found in the literature. Furthermore, the CV show essentially the same behaviour. While the current measured from the NMC cantilever is noisier, perhaps due to an electrical contact issue, both show a similar shaped first cycle. Further cycles show greatly diminished currents, but the current is always positive. It seems that reactions with LFP and NMC, which are known to be different, are not happening at all. The common features between the cantilevers are the mica, the aluminum current collector and the non-active components of the electrode slurry (polyvinylidene fluoride and acetylene black), one or more of which must be responsible for the observed electrochemistry.

Figure 5.12 shows micrographs of a battery electrode cantilever taken after electrochemical measurements. Figure 5.12a shows a stereo microscope image. The most

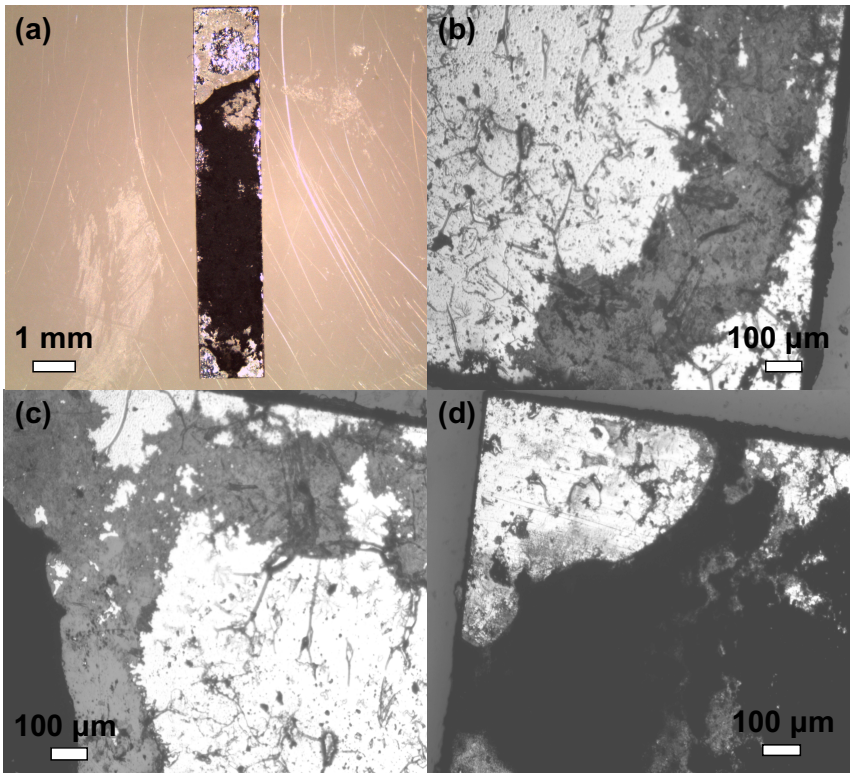

FIGURE 5.12: Images of a battery electrode cantilever taken after electrochemical testing taken by (a) stereo microscope and (b-d) optical microscope. An overhead light source is used so bright areas are aluminum, black areas are battery electrode material and grey is mica.

noticeable feature is that there is damage to the aluminum layer and the mica, which should be completely covered in aluminum, is visible. This is confirmed by the optical microscope images. The greater magnification shows that the delamination of the aluminum occurs even under the battery material. In particular, in Figure 5.12d, it appears that delamination of the aluminum has caused part of the battery material layer to detach with it. This is an extreme case of delamination, but this was observable to an extent in most cantilevers that were tested. To get a handle on this damage to the aluminum layer, three different cantilevers were put through the same electrochemical procedure, and their resistance was measured before and after. The cantilevers were made from mica with an aluminum thin film, as shown throughout this section, $50\,\mu\mathrm{m}$ SiO_2 glass with an aluminum thin film, from a previous project, and household aluminum foil. Figure 5.13 shows the CV for each of these aluminum-containing cantilevers. The thin film aluminum coated mica and glass show essentially the same shape to the CV. A single peak occurs in the first cycle, centred at approximately $0.4\,\mathrm{V}$ versus Ag/AgCl pseudo-reference. After this peak, the current response is flat. Strangely enough though, this constant current response occurs at a positive current for unknown reason. A current flow of zero would have been expected. The CV of the aluminum foil also shows a peak at $0.4\,\mathrm{V}$ during the first cycle, and diminished current response after that. In all cases, the

currents measured are positive. That is, there is no reversal of this reaction of the aluminum. The discrepancy in current behaviour after the first cycle between the thin film aluminum coated materials and the aluminum foil may have to do with integrity of the film and surface compared to the foil. If the thin film materials can delaminate, fresh surfaces are exposed. Delamination was not observed with foil. As mentioned, before and after electrochemistry was performed, DC resistance of the films was measured. Before electrochemistry, all samples had resistance on the order of $1\,\Omega$. The resistance of the aluminum foil was unchanged after performing electrochemistry, however the resistance both of the thin film aluminum coated cantilevers was $>10\,\mathrm{M}\Omega$. Similar changes in resistance were observed in cantilevers coated with battery material.

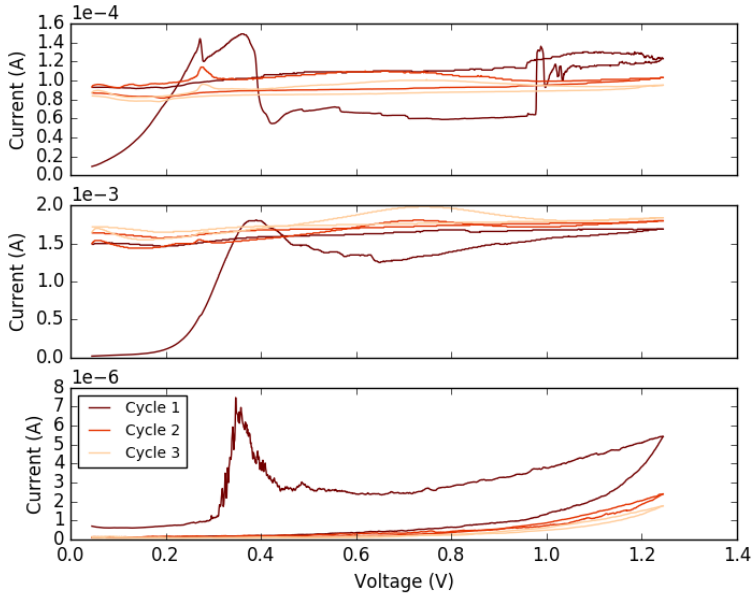

FIGURE 5.13: Cyclic voltammograms of mica coated with aluminum (top) and glass coated with aluminum (middle) and aluminum foil (bottom) cantilevers in 1M Li_2SO_4. Potential was scanned from $45\,\mathrm{mV}$ to $1.245\,\mathrm{V}$ at a rate of $5\,\mathrm{mV\,s^{-1}}$. Potentials versus Ag/AgCl pseudo-reference.

Taking all of these results into consideration, it is believed that aluminum is reacting in the aqueous environment, over the potential window selected, evidenced by the CV in Figure 5.13 and the inability to reproduce reactions with battery materials from the literature. The reaction seems to mechanically disturbs the aluminum enough that it loses adhesion to the surface it was deposited on. This causes delamination of parts of the film, as shown in Figure 5.12. It is also believed that microscopically, the thin film aluminum may detach and break up into isolated domains, explaining why conductivity was lost after electrochemistry. Not only is adhesion of the current collector critical to establishing electrical contact with battery material, it is also necessary for stress transduction. Stress on or within the battery material

layer results in in-plane forces that are transmitted to the mica substrate via the metal layer. If the metal layer cannot remain adhered it cannot transmit this force. Li and Church[123] performed linear and cyclic voltammetry of aluminum in Li_2SO_4 solutions. Firstly, they determined that in these solutions, the onset of oxygen evolution is 1.25 V vs. Ag/AgCl at pH = 7. This is higher than the expected value for pure water (approximately 1 V vs. Ag/AgCl). These results agree with those by Wang *et. al.*[120], who showed that potentials of less than 1.25 V vs. Ag/AgCl can be used without oxygen evolution. During all of the CV experiments in this work, gas bubble formation in solution was not observed. All experiments stayed below the prescribed limit of 1.25 V vs. Ag/AgCl. It is therefore believed that gas evolution on the cantilever was not present and therefore not the cause of the damage to the Al current collector. Furthermore, Li and Church show that in CV experiments, a large first cycle current is observed during anodic polarization, and subsequent cycles are essentially featureless. It was suggested that this was due to passivation of the surface, possibly with LiOH[123].

The inability to perform the correct electrochemistry and measure a corresponding deflection is believed to be due to reactions of the metal current collector layer in these battery electrode cantilevers. In an aqueous environment, it appears that another conducting layer should be used. Gold was quickly tested as a candidate, but it also reacts, even leaving brown residue in the electrolyte. Platinum seems like the next logical choice, as it is known for being inert. Alternatively, aluminum is known to be stable as a current collector in non-aqueous battery chemistries. The use of these cantilevers in a 1M $LiPF_6$ electrolyte solution, assembled in an inert environment, as originally intended, still seems highly likely to work, pending access to an inert atmosphere glovebox. The design of these cantilevers and use of mica as a substrate constitute a very simple sensor that can be used to study battery materials, and presumably many other electrochemical systems. Despite the difficulties presented in this section, the potential for future work is high, and changes required to achieve successful results should be minimal.

Chapter 6

Conclusions

Two techniques were assessed for the study of lithium ion battery materials with the eventual goal of performing *in situ* study of the solid electrolyte interphase that is formed on the electrode surfaces. The first was combined tip-enhanced Raman spectroscopy and atomic force microscopy to measure local chemistry and morphology with sub-wavelength resolution. Confocal Raman microscopy was performed on polished $LiFePO_4$ and Li_xFePO_4 surfaces as the first step towards *in situ* TERS measurements. Raman spectra obtained on $LiFePO_4$ showed agreement with literature spectra and showed spatial homogeneity over a $10\,\mu m$ x $10\,\mu m$ region on the $LiFePO_4$ surface. Measurements on partially delithiated Li_xFePO_4 showed changes in Raman spectra from the fully lithiated sample, as well as spatial variation within the same sample. Raman mapping on Li_xFePO_4 was used to identify two different phases or domains. Analysis of the spectra from each region may indicate contrast was caused by changes in lithium concentrations, but without a more direct measurement of the local lithium concentrations in the identical area, this is unconfirmed. Samples of sub-monolayer $LiFePO_4$ nanoplatelets deposited on template stripped gold substrates were assembled for the purpose of performing TERS experiments. Repeated TERS experiments were unable to produce a Raman signal. This is thought to be largely due to the unreliable nature of fabricating gold tips that can produce a localized surface plasmon resonance. Further difficulties arise because AFM is required to locate the samples on which TERS is to be performed, but the implementation of these gold tips with lateral force tuning fork AFM and poor feedback control cause damage to the tips during imaging. This damage seems to also contribute to the inability to generate a surface plasmon resonance at the tip. Due to difficulties with *ex situ* TERS measurements, the pursuit of *in situ* TERS was abandoned until the field shows sufficient progress.

The outlook for TERS as a technique is still positive. Raman spectroscopy and AFM have both been used *in situ*, to measure phenomena in lithium ion batteries. Combing the two techniques and achieving TERS is really only limited by understanding of how tip fabrication affects the localized surface plasmon resonance and how to reliably fabricate a tip that will produce a resonance, while being robust enough to perform AFM topography scans. Additionally, consideration of tuning fork versus cantilevered tips and imaging mode (tapping mode, lateral force mode,

etc.) may provide a breakthrough, however, such discussions are ongoing across the entire scanning probe field and in many cases, it is unclear which approach is optimal.

The second technique investigated was cantilever sensing. The application of cantilever sensing to battery materials has rarely been attempted and upon undertaking this work, there was an absence of this particular application in the scientific literature. To develop this technique, a battery electrode cantilever was fabricated, using a muscovite mica sheet as an elastic substrate, a deposited metal layer as a current collector and a layer deposited from a slurry of electrode active material. The base of these battery electrode cantilevers, the mica layer, were cut into $10\,\mathrm{mm}$ x $1.5\,\mathrm{mm}$ rectangles from $50\,\mu\mathrm{m}$ mica sheets using a variety of techniques, of which carefully performed wire saw cutting was found to be superior. An airtight electrochemical chamber with windows was fabricated to facilitate electrochemistry with moisture sensitive components, such as lithium-ion battery materials, while providing optical access for a laser beam deflection system to measure stress-induced bending of the cantilever. Due to unfortunate circumstances, the usage of non-aqueous electrolytes and lithium metal was not possible, so measurements were attempted in aqueous conditions. While it was expected that the electrode materials would be unstable while charging in aqueous electrolyte, it was found that the current collector used, aluminum for positive electrode materials, was reacting with the electrolyte. The reaction of the current collector caused it to delaminate from the mica surface, and destroyed the electrical conductivity across the cantilevers. Unfortunately, there was no measurable stress response to this reaction, so all deflection experiments were unsuccessful.

The battery electrode cantilevers developed were designed to closely model commercial lithium ion electrodes. That means they were designed to be implemented with non-aqueous electrolytes and lithium metal counter/reference electrodes, in an airtight electrochemical cell. Given an inert environment with sufficiently low concentrations of oxygen and water in which to prepare the electrochemical cell, the cantilever should work very well. The spring constant of the cantilevers can be easily controlled by changing the dimensions of the mica, by cutting and/or cleaving layers. This means that their sensitivity can be tuned measure to high stress or low stress events. Cantilever sensing in this format is still a technique with considerable potential and certainly worth further development. To pursue this work further in an aqueous environment, the use of aluminum as a current collector is clearly an issue. The proposed solution is to replace aluminum with a material that is conductive, yet inert when exposed to these potentials and reactants. Platinum, despite its expense, is thought to be a good candidate.

Both of the techniques studied in this work show promise for being viable means of studying lithium ion battery materials. They are both capable of *in situ* study which in the field of lithium ion batteries is invaluable. As the electrode and electrolyte formulations used at the cutting edge of the lithium ion battery field become

increasingly complicated, determining the internal mechanisms that control battery performance will become more difficult, yet more important. These techniques, although undoubtedly requiring more research and development, are poised to be useful tools in provide that understanding.

Bibliography

[1] Jeff Tsao, Nate Lewis, and George Crabtree. *Solar FAQs*. Tech. rep. 2006. URL: http://www.cleanenergysa.com/wp-content/uploads/2016/07/Solar-FAQs.pdf.

[2] M. Iqbal. "A study of Canadian diffuse and total solar radiation data - I Monthly average daily horizontal radiation". In: *Solar Energy* 22.1 (1979), pp. 81–86. DOI: 10.1016/0038-092X(79)90063-X. URL: http://linkinghub.elsevier.com/retrieve/pii/0038092X7990063X.

[3] Magnus Korpaas, Arne T. Holen, and Ragne Hildrum. "Operation and sizing of energy storage for wind power plants in a market system". In: *International Journal of Electrical Power & Energy Systems* 25.8 (2003), pp. 599–606. ISSN: 01420615. DOI: 10.1016/S0142-0615(03)00016-4. URL: http://linkinghub.elsevier.com/retrieve/pii/S0142061503000164.

[4] D. Prandle. "Simple theory for designing tidal power schemes". In: *Advances in Water Resources* 7.1 (1984), pp. 21–27. ISSN: 03091708. DOI: 10.1016/0309-1708(84)90026-5. URL: http://linkinghub.elsevier.com/retrieve/pii/0309170884900265.

[5] J.P. Barton and D.G. Infield. "Energy Storage and Its Use With Intermittent Renewable Energy". In: *IEEE Transactions on Energy Conversion* 19.2 (2004), pp. 441–448. ISSN: 0885-8969. DOI: 10.1109/TEC.2003.822305. URL: http://ieeexplore.ieee.org/document/1300713/.

[6] Joern Hoppmann et al. "The economic viability of battery storage for residential solar photovoltaic systems – A review and a simulation model". In: *Renewable and Sustainable Energy Reviews* 39 (2014), pp. 1101–1118. ISSN: 13640321. DOI: 10.1016/j.rser.2014.07.068. URL: http://linkinghub.elsevier.com/retrieve/pii/S1364032114005206.

[7] Bruce Dunn, Haresh Kamath, and Jean-Marie Tarascon. "Electrical Energy Storage for the Grid: A Battery of Choices". In: *Science* 334.6058 (2011). URL: http://science.sciencemag.org/content/334/6058/928.full.

[8] Sergio Manzetti and Florin Mariasiu. "Electric vehicle battery technologies: From present state to future systems". In: *Renewable and Sustainable Energy Reviews* 51 (2015), pp. 1004–1012. ISSN: 13640321. DOI: 10.1016/j.rser.2015.07.010. URL: http://linkinghub.elsevier.com/retrieve/pii/S1364032115006577.

[9] M Noel. "Role of carbon host lattices in Li-ion intercalation/de-intercalation processes". In: *Journal of Power Sources* 111.2 (2002), pp. 193–209. ISSN: 03787753. DOI: 10.1016/S0378-7753(02)00308-7. URL: http://www.sciencedirect.com/science/article/pii/S0378775302003087.

[10] K. Mizushima et al. "LixCoO2 (0<x<-1): A new cathode material for batteries of high energy density". In: *Materials Research Bulletin* 15.6 (1980), pp. 783–789. ISSN: 00255408. DOI: 10.1016/0025-5408(80)90012-4. URL: http://linkinghub.elsevier.com/retrieve/pii/0025540880900124.

[11] E. Peled. "The Electrochemical Behavior of Alkali and Alkaline Earth Metals in Nonaqueous Battery Systems—The Solid Electrolyte Interphase Model". en. In: *Journal of The Electrochemical Society* 126.12 (1979), p. 2047. ISSN: 00134651. DOI: 10.1149/1.2128859. URL: http://jes.ecsdl.org/content/126/12/2047.abstract.

[12] Pallavi Verma, Pascal Maire, and Petr Novák. "A review of the features and analyses of the solid electrolyte interphase in Li-ion batteries". In: *Electrochimica Acta* 55.22 (2010), pp. 6332–6341. ISSN: 00134686. DOI: 10.1016/j.electacta.2010.05.072. URL: http://www.sciencedirect.com/science/article/pii/S0013468610007747.

[13] J. C. Burns et al. "Evaluation of Effects of Additives in Wound Li-Ion Cells Through High Precision Coulometry". In: *Journal of The Electrochemical Society* 158.3 (2011), A255. ISSN: 00134651. DOI: 10.1149/1.3531997. URL: http://jes.ecsdl.org/cgi/doi/10.1149/1.3531997.

[14] K. Zaghib et al. "LiFePO4: From molten ingot to nanoparticles with high-rate performance in Li-ion batteries". In: *Journal of Power Sources* 195.24 (2010), pp. 8280–8288. ISSN: 03787753. DOI: 10.1016/j.jpowsour.2010.07.010. URL: http://linkinghub.elsevier.com/retrieve/pii/S0378775310011535.

[15] R. Spotnitz. "Simulation of capacity fade in lithium-ion batteries". In: *Journal of Power Sources* 113.1 (2003), pp. 72–80. ISSN: 03787753. DOI: 10.1016/S0378-7753(02)00490-1. URL: http://www.sciencedirect.com/science/article/pii/S0378775302004901.

[16] Rachid Yazami. "Surface chemistry and lithium storage capability of the graphite–lithium electrode". In: *Electrochimica Acta* 45.1-2 (1999), pp. 87–97. ISSN: 00134686. DOI: 10.1016/S0013-4686(99)00195-4. URL: http://www.sciencedirect.com/science/article/pii/S0013468699001954.

[17] Hugues Duncan, Yaser Abu-Lebdeh, and Isobel J. Davidson. "Study of the Cathode–Electrolyte Interface of LiMn[sub 1.5]Ni[sub 0.5]O[sub 4] Synthesized by a Sol–Gel Method for Li-Ion Batteries". In: *Journal of The Electrochemical Society* 157.4 (2010), A528. ISSN: 00134651. DOI: 10.1149/1.3321710. URL: http://jes.ecsdl.org/content/157/4/A528.full.

[18] Doron Aurbach et al. "Common Electroanalytical Behavior of Li Intercalation Processes into Graphite and Transition Metal Oxides". In: *Journal of The Electrochemical Society* 145.9 (1998), p. 3024. ISSN: 00134651. DOI: 10.1149/1.1838758. URL: http://jes.ecsdl.org/cgi/doi/10.1149/1.1838758.

[19] E. Peled. "Advanced Model for Solid Electrolyte Interphase Electrodes in Liquid and Polymer Electrolytes". en. In: *Journal of The Electrochemical Society* 144.8 (1997), p. L208. ISSN: 00134651. DOI: 10.1149/1.1837858. URL: http://jes.ecsdl.org/content/144/8/L208.abstract.

[20] D. D. MacNeil, D. Larcher, and J. R. Dahn. "Comparison of the Reactivity of Various Carbon Electrode Materials with Electrolyte at Elevated Temperature". In: *Journal of The Electrochemical Society* 146.10 (1999), p. 3596. ISSN: 00134651. DOI: 10.1149/1.1392520. URL: http://jes.ecsdl.org/cgi/doi/10.1149/1.1392520.

[21] H. H. Lee, C. C. Wan, and Y. Y. Wang. "Thermal Stability of the Solid Electrolyte Interface on Carbon Electrodes of Lithium Batteries". In: *Journal of The Electrochemical Society* 151.4 (2004), A542. ISSN: 00134651. DOI: 10.1149/1.1647568. URL: http://jes.ecsdl.org/cgi/doi/10.1149/1.1647568.

[22] Guorong V. Zhuang, Yufeng Chen, and Philip N. Ross. "The Reaction of Lithium with Dimethyl Carbonate and Diethyl Carbonate in Ultrahigh Vacuum Studied by X-ray Photoemission Spectroscopy". In: *Langmuir* 15.3 (1999), pp. 1470–1479. ISSN: 0743-7463. DOI: 10.1021/la980454y. URL: http://pubs.acs.org/doi/abs/10.1021/la980454y.

[23] Thomas Marks et al. "A Guide to Li-Ion Coin-Cell Electrode Making for Academic Researchers". In: *Journal of The Electrochemical Society* 158.1 (2011), A51. ISSN: 00134651. DOI: 10.1149/1.3515072. URL: http://jes.ecsdl.org/cgi/doi/10.1149/1.3515072.

[24] Zhonghua Lu et al. "Synthesis, Structure, and Electrochemical Behavior of Li[Ni[sub x]Li[sub 1/3-2x/3]Mn[sub 2/3-x/3]]O[sub 2]". In: *Journal of The Electrochemical Society* 149.6 (2002), A778. ISSN: 00134651. DOI: 10.1149/1.1471541. URL: http://jes.ecsdl.org/cgi/doi/10.1149/1.1471541.

[25] Zhaohui Chen and J. R. Dahn. "Effect of a ZrO[sub 2] Coating on the Structure and Electrochemistry of Li[sub x]CoO[sub 2] When Cycled to 4.5 V". In: *Electrochemical and Solid-State Letters* 5.10 (2002), A213. ISSN: 10990062. DOI: 10.1149/1.1503202. URL: http://esl.ecsdl.org/cgi/doi/10.1149/1.1503202.

[26] Doron Aurbach et al. "Design of electrolyte solutions for Li and Li-ion batteries: a review". In: *Electrochimica Acta* 50.2-3 (2004), pp. 247–254. ISSN: 00134686. DOI: 10.1016/j.electacta.2004.01.090. URL: http://linkinghub.elsevier.com/retrieve/pii/S0013468604006413.

[27] D. Y. Wang et al. "A Systematic Study of Electrolyte Additives in Li[Ni1/3Mn1/3Co1/3]O2 (NMC)/Graphite Pouch Cells". In: *Journal of the Electrochemical Society* 161.12 (2014), A1818–A1827. ISSN: 0013-4651. DOI: 10.1149/2.0511412jes. URL: http://jes.ecsdl.org/cgi/doi/10.1149/2.0511412jes.

[28] H. Bryngelsson et al. "How dynamic is the SEI?" In: *Journal of Power Sources* 174.2 (2007), pp. 970–975. ISSN: 03787753. DOI: 10.1016/j.jpowsour.2007.06.050. URL: http://www.sciencedirect.com/science/article/pii/S0378775307013353.

[29] Kristina Edström, Marie Herstedt, and Daniel P. Abraham. "A new look at the solid electrolyte interphase on graphite anodes in Li-ion batteries". In: *Journal of Power Sources* 153.2 (2006), pp. 380–384. ISSN: 03787753. DOI: 10.1016/j.jpowsour.2005.05.062. URL: http://www.sciencedirect.com/science/article/pii/S037877530500738X.

[30] S. Francis Amalraj and Doron Aurbach. "The use of in situ techniques in R&D of Li and Mg rechargeable batteries". In: *Journal of Solid State Electrochemistry* 15.5 (2011), pp. 877–890. ISSN: 1432-8488. DOI: 10.1007/s10008-011-1324-9. URL: http://link.springer.com/10.1007/s10008-011-1324-9.

[31] R. Aroca et al. "Vibrational Spectra and Ion-Pair Properties of Lithium Hexafluorophosphate in Ethylene Carbonate Based Mixed-Solvent Systems for Lithium Batteries". en. In: *Journal of Solution Chemistry* 29.10 (2000), pp. 1047–1060. ISSN: 1572-8927. DOI: 10.1023/A:1005151220893. URL: http://link.springer.com.proxy3.library.mcgill.ca/article/10.1023/A{\%}3A1005151220893.

[32] Takayuki Doi et al. "Electrochemical AFM study of LiMn2O4 thin film electrodes exposed to elevated temperatures". In: *Journal of Power Sources* 180.1 (2008), pp. 539–545. ISSN: 03787753. DOI: 10.1016/j.jpowsour.2008.02.054. URL: http://www.sciencedirect.com/science/article/pii/S0378775308003911.

[33] Soon-Ki Jeong et al. "AFM study of surface film formation on a composite graphite electrode in lithium-ion batteries". In: *Journal of Power Sources* 119-121 (2003), pp. 555–560. ISSN: 03787753. DOI: 10.1016/S0378-7753(03)00288-X. URL: http://www.sciencedirect.com/science/article/pii/S037877530300288X.

[34] Collin R. Becker et al. "In situ atomic force microscopy of lithiation and delithiation of silicon nanostructures for lithium ion batteries". In: *ACS Nano* 7.10 (2013), pp. 9173–9182. ISSN: 19360851. DOI: 10.1021/nn4037909.

[35] Doron Aurbach, Maxim Koltypin, and Hanan Teller. "In Situ AFM Imaging of Surface Phenomena on Composite Graphite Electrodes during Lithium Insertion". In: *Langmuir* 18.23 (2002), pp. 9000–9009. ISSN: 0743-7463. DOI: 10.1021/la020306e. URL: http://dx.doi.org/10.1021/la020306e.

[36] Doron Aurbach. "The Application of Atomic Force Microscopy for the Study of Li Deposition Processes". en. In: *Journal of The Electrochemical Society* 143.11 (1996), p. 3525. ISSN: 00134651. DOI: 10.1149/1.1837248. URL: http://jes.ecsdl.org/content/143/11/3525.abstract.

[37] Doron Aurbach. "In Situ Micromorphological Studies of Li Electrodes by Atomic Force Microscopy in a Glove Box System". en. In: *Electrochemical and Solid-State Letters* 2.1 (1999), p. 16. ISSN: 10990062. DOI: 10.1149/1.1390719. URL: http://esl.ecsdl.org/content/2/1/16.abstract.

[38] Adolf Smekal. "Zur Quantentheorie der Dispersion". In: *Die Naturwissenschaften* 11.43 (1923), pp. 873–875. ISSN: 0028-1042. DOI: 10.1007/BF01576902. URL: http://link.springer.com/10.1007/BF01576902.

[39] C. V. Raman and K. S. Krishnan. "A New Type of Secondary Radiation". In: *Nature* 121 (1928), pp. 501–502. DOI: 10.1038/121501c0. URL: http://www.nature.com/nature/journal/v121/n3048/abs/121501c0.html?foxtrotcallback=true.

[40] C. V. Raman and K. S. Krishnan. "The Optical Analogue of the Compton Effect". In: *Nature* 121 (1928), p. 711. DOI: 10.1038/121711a0. URL: https://www.nature.com/nature/journal/v121/n3053/abs/121711a0.html.

[41] C. V. Raman and K. S. Krishnan. "A Change of Wave-length in Light Scattering". In: *Nature* 121 (1928), pp. 619–629. DOI: 10.1038/121619b0. URL: https://www.nature.com/nature/journal/v121/n3051/abs/121619b0.html.

[42] Mischa Nicklaus. "Tip-Enhanced Raman Spectroscopy for Nanoelectronics". Ph.D. Thesis. Universite du Quebec Institut National de la Recherche Scientifique, 2013.

[43] YunWei Charles Cao, Rongchao Jin, and Chad A. Mirkin. "Nanoparticles with Raman spectroscopic fingerprints for DNA and RNA detection." In: *Science* 297.5586 (2002), pp. 1536–1540. ISSN: 00368075. DOI: 10.1126/science.297.5586.1536. URL: http://science.sciencemag.org/content/297/5586/1536.full.

[44] Jan-Christoph Panitz and Petr Novák. "Raman microscopy as a quality control tool for electrodes of lithium-ion batteries". In: *Journal of Power Sources* 97-98 (2001), pp. 174–180. ISSN: 03787753. DOI: 10.1016/S0378-7753(01)00679-6. URL: http://www.sciencedirect.com/science/article/pii/S0378775301006796.

[45] Fiona C. Clarke et al. "Chemical Image Fusion. The Synergy of FT-NIR and Raman Mapping Microscopy To Enable a More Complete Visualization of Pharmaceutical Formulations". In: *Analytical Chemistry* 73.10 (2001), pp. 2213–2220. DOI: 10.1021/AC001327L. URL: http://pubs.acs.org/doi/abs/10.1021/ac001327l.

[46] Minoru Inaba et al. "In Situ Raman Study on Electrochemical Li Intercalation into Graphite". In: *Journal of The Electrochemical Society* 142.1 (1995), p. 20. ISSN: 00134651. DOI: 10.1149/1.2043869.

[47] Takashi Itoh et al. "In situ Raman spectroscopic study of LixCoO2 electrodes in propylene carbonate solvent systems". In: *Journal of Power Sources* 68.2 (1997), pp. 333–337. ISSN: 03787753. DOI: 10.1016/S0378-7753(97)02539-1. URL: http://www.sciencedirect.com/science/article/pii/S0378775397025391.

[48] Weiwei Huang and Roger Frech. "In Situ Roman Studies of Graphite Surface Structures during Lithium Electrochemical Intercalation". In: *Journal of The Electrochemical Society* 145.3 (1998), p. 765. ISSN: 00134651. DOI: 10.1149/1.1838343. URL: http://jes.ecsdl.org/cgi/doi/10.1149/1.1838343.

[49] Christopher M. Burba and Roger Frech. "Raman and FTIR Spectroscopic Study of Li[sub x]FePO[sub 4] (0<x<1)". In: *Journal of The Electrochemical Society* 151.7 (2004), A1032. ISSN: 00134651. DOI: 10.1149/1.1756885. URL: http://link.aip.org/link/JESOAN/v151/i7/pA1032/s1{\&}Agg=doi.

[50] Masayuki Morita et al. "A Raman spectroscopic study of organic electrolyte solutions based on binary solvent systems of ethylene carbonate with low viscosity solvents which dissolve different lithium salts". en. In: *Journal of the Chemical Society, Faraday Transactions* 94.23 (1998), pp. 3451–3456. ISSN: 09565000. DOI: 10.1039/a806278a. URL: http://pubs.rsc.org/en/content/articlehtml/1998/ft/a806278ahttp://xlink.rsc.org/?DOI=a806278a.

[51] Zhaoxiang Wang et al. "Ion Association and Solvation Studies of LiClO[sub 4]/Ethylene Carbonate Electrolyte by Raman and Infrared Spectroscopy". In: *Journal of The Electrochemical Society* 145.10 (1998), p. 3346. ISSN: 00134651. DOI: 10.1149/1.1838810.

[52] Robert Kostecki et al. “Interfacial studies of a thin-film Li2Mn4O9 electrode”. In: *Electrochimica Acta* 45.1 (1999), pp. 225–233. ISSN: 00134686. DOI: 10.1016/S0013-4686(99)00206-6.

[53] Robert Kostecki and Frank McLarnon. “Degradation of LiNi0.8Co0.2 O 2 Cathode Surfaces in High-Power Lithium-Ion Batteries”. en. In: *Electrochemical and Solid-State Letters* 5.7 (2002), A164–A166. ISSN: 1944-8775. DOI: 10.1149/1.1482199. URL: http://esl.ecsdl.org/content/5/7/A164.full.

[54] Robert Kostecki and Frank McLarnon. “Microprobe study of the effect of Li intercalation on the structure of graphite”. In: *Journal of Power Sources* 119 (2003), pp. 550–554. ISSN: 03787753. DOI: 10.1016/S0378-7753(03)00287-8.

[55] Robert Kostecki and Frank McLarnon. “Local-Probe Studies of Degradation of Composite LiNi[sub 0.8]Co[sub 0.15]Al[sub 0.05]O[sub 2] Cathodes in High-Power Lithium-Ion Cells”. en. In: *Electrochemical and Solid-State Letters* 7.10 (2004), A380. ISSN: 10990062. DOI: 10.1149/1.1793771. URL: http://esl.ecsdl.org/content/7/10/A380.full.

[56] Jinglei Lei, Frank Mclarnon, and Robert Kostecki. “In Situ Raman Microscopy of Individual LiNi0.8Co0.15Al0.05O2 Particles in a Li-Ion Battery Composite Cathode”. In: *Journal of Physical Chemistry B* 109 (2005), pp. 952–957.

[57] M. Maccario et al. “Raman and FTIR Spectroscopy Investigations of Carbon-Coated Li[sub x]FePO[sub 4] Materials”. In: *Journal of The Electrochemical Society* 155.12 (2008), A879. ISSN: 00134651. DOI: 10.1149/1.2977961. URL: http://jes.ecsdl.org/cgi/doi/10.1149/1.2977961.

[58] Jagjit Nanda et al. “In situ Raman microscopy during discharge of a high capacity silicon-carbon composite Li-ion battery negative electrode”. In: *Electrochemistry Communications* 11.1 (2009), pp. 235–237. ISSN: 13882481. DOI: 10.1016/j.elecom.2008.11.006. URL: http://linkinghub.elsevier.com/retrieve/pii/S1388248108005213.

[59] Masaki Matsui, Kaoru Dokko, and Kiyoshi Kanamura. “Dynamic behavior of surface film on LiCoO2 thin film electrode”. In: *Journal of Power Sources* 177.1 (2008), pp. 184–193. ISSN: 03787753. DOI: 10.1016/j.jpowsour.2007.10.078. URL: http://www.sciencedirect.com/science/article/pii/S0378775307023695.

[60] Yin Zhang et al. “A simple solvothermal route to synthesize graphene-modified LiFePO4 cathode for high power lithium ion batteries”. In: *Journal of Power Sources* 210 (2012), pp. 47–53. ISSN: 03787753. DOI: 10.1016/j.jpowsour.2012.03.007.

[61] Yu He et al. “Shape evolution of patterned amorphous and polycrystalline silicon microarray thin film electrodes caused by lithium insertion and extraction”. In: *Journal of Power Sources* 216 (2012), pp. 131–138. ISSN: 03787753. DOI: 10.1016/j.jpowsour.2012.04.105.

[62] G. Binnig, C. F. Quate, and Ch. Gerber. “Atomic Force Microscope”. In: *Physical Review Letters* 56.9 (1986), pp. 930–933. ISSN: 0031-9007. DOI: 10.1103/PhysRevLett.56.930. URL: https://link.aps.org/doi/10.1103/PhysRevLett.56.930.

[63] Bert Voigtländer. *Scanning Probe Microscopy: Atomic Force Microscopy and Scanning Tunneling Microscopy*. Heidelberg: Springer, 2015, p. 9. ISBN: 978-3-662-45239-4. DOI: 10.1007/978-3-662-45240-0.

[64] M. Nonnenmacher, M. P. O’Boyle, and H. K. Wickramasinghe. “Kelvin probe force microscopy”. In: *Applied Physics Letters* 58.25 (1991), pp. 2921–2923. ISSN: 0003-6951. DOI: 10.1063/1.105227. URL: http://aip.scitation.org/doi/10.1063/1.105227.

[65] O. Gröning et al. “Field emission from DLC films”. In: *Applied Surface Science* 111 (1997), pp. 135–139. ISSN: 01694332. DOI: 10.1016/S0169-4332(96)00713-1. URL: http://linkinghub.elsevier.com/retrieve/pii/S0169433296007131.

[66] U. Hartmann. “Magnetic Force Microscopy”. In: *Annual Review of Materials Science* 29.1 (1999), pp. 53–87. ISSN: 0084-6600. DOI: 10.1146/annurev.matsci.29.1.53. URL: http://www.annualreviews.org/doi/10.1146/annurev.matsci.29.1.53.

[67] D. F. Ogletree, Robert W. Carpick, and M. Salmeron. “Calibration of frictional forces in atomic force microscopy”. In: *Review of Scientific Instruments* 67.1996 (1996), p. 3298. ISSN: 00346748. DOI: 10.1063/1.1147411. URL: http://aip.scitation.org/doi/abs/10.1063/1.1147411http://link.aip.org/link/RSINAK/v67/i9/p3298/s1{\&}Agg=doi.

[68] Minoru Inaba et al. “Electrochemical Scanning Tunneling Microscopy Observation of Highly Oriented Pyrolytic Graphite Surface Reactions in an Ethylene Carbonate-Based Electrolyte Solution”. In: *Langmuir* 12.6 (1996), pp. 1535–1540. ISSN: 0743-7463. DOI: 10.1021/la950848e. URL: http://dx.doi.org/10.1021/la950848e.

[69] Minoru Inaba et al. “Electrochemical scanning tunneling microscopy analysis of the surface reactions on graphite basal plane in ethylene carbonate-based solvents and propylene carbonate”. In: *Journal of Power Sources* 68.2 (1997), pp. 221–226. ISSN: 03787753. DOI: 10.1016/S0378-7753(96)02555-4. URL: http://www.sciencedirect.com/science/article/pii/S0378775396025554.

[70] Minoru Inaba et al. "STM study on graphite/electrolyte interface in lithium-ion batteries: solid electrolyte interface formation in trifluoropropylene carbonate solution". In: *Electrochimica Acta* 45.1-2 (1999), pp. 99–105. ISSN: 00134686. DOI: 10.1016/S0013-4686(99)00196-6. URL: http://www.sciencedirect.com/science/article/pii/S0013468699001966.

[71] Minoru Inaba et al. "Electrochemical STM observation of LiMn2O4 thin films prepared by pulsed laser deposition". In: *Journal of Power Sources* 81-82 (1999), pp. 554–557. ISSN: 03787753. DOI: 10.1016/S0378-7753(99)00215-3. URL: http://www.sciencedirect.com/science/article/pii/S0378775399002153.

[72] Soon-Ki Jeong et al. "Surface Film Formation on Graphite Negative Electrode in Lithium-Ion Batteries: AFM Study in an Ethylene Carbonate-Based Solution". en. In: *Journal of The Electrochemical Society* 148.9 (2001), A989. ISSN: 00134651. DOI: 10.1149/1.1387981. URL: http://jes.ecsdl.org/content/148/9/A989.full.

[73] Soon-Ki Jeong et al. "Surface Film Formation on a Graphite Negative Electrode in Lithium-Ion Batteries: Atomic Force Microscopy Study on the Effects of Film-Forming Additives in Propylene Carbonate Solutions". In: *Langmuir* 17.26 (2001), pp. 8281–8286. ISSN: 0743-7463. DOI: 10.1021/la015553h. URL: http://dx.doi.org/10.1021/la015553h.

[74] Soon-Ki Jeong et al. "Interfacial reactions between graphite electrodes and propylene carbonate-based solutions: Electrolyte-concentration dependence of electrochemical lithium intercalation reaction". In: *Journal of Power Sources* 175.1 (2008), pp. 540–546. ISSN: 03787753. DOI: 10.1016/j.jpowsour.2007.08.065. URL: http://www.sciencedirect.com/science/article/pii/S0378775307016485.

[75] Minoru Inaba, Soon-Ki Jeong, and Zempachi Ogumi. "In Situ Scanning Probe Microscopy of Interfacial Phenomena in Batteries". In: *Interface* 20.3 (2011), pp. 55–59. URL: https://www.electrochem.org/dl/interface/fal/fal11/fal11{_}p055-059.pdfhttp://www.electrochem.org/dl/interface/if{_}curr{_}iss.htm.

[76] Yair Cohen and Doron Aurbach. "The use of a special work station for in situ measurements of highly reactive electrochemical systems by atomic force and scanning tunneling microscopes". In: *Review of Scientific Instruments* 70.12 (1999), p. 4668. ISSN: 00346748. DOI: 10.1063/1.1150130. URL: http://scitation.aip.org/content/aip/journal/rsi/70/12/10.1063/1.1150130.

[77] Yaron S. Cohen, Yair Cohen, and Doron Aurbach. "Micromorphological Studies of Lithium Electrodes in Alkyl Carbonate Solutions Using in Situ Atomic Force Microscopy". In: *The Journal of Physical Chemistry B* 104.51 (2000), pp. 12282–

12291. ISSN: 1520-6106. DOI: 10.1021/jp002526b. URL: http://dx.doi.org/10.1021/jp002526b.

[78] J.S Gnanaraj et al. "The effect of pressure on the electroanalytical response of graphite anodes and LiCoO2 cathodes for Li-ion batteries". In: *Journal of Electroanalytical Chemistry* 516.1 (2001), pp. 89–102. ISSN: 15726657. DOI: 10.1016/S0022-0728(01)00663-5.

[79] I Isaev et al. "A new approach for the preparation of anodes for Li-ion batteries based on activated hard carbon cloth with pore design". In: *Journal of Power Sources* 119 (2003), pp. 28–33. ISSN: 03787753. DOI: 10.1016/S0378-7753(03)00119-8.

[80] Maxim Koltypin et al. "The study of lithium insertion–deinsertion processes into composite graphite electrodes by in situ atomic force microscopy (AFM)". In: *Electrochemistry Communications* 4.1 (2002), pp. 17–23. ISSN: 13882481. DOI: 10.1016/S1388-2481(01)00264-8. URL: http://www.sciencedirect.com/science/article/pii/S1388248101002648.

[81] Yaron S. Cohen and Doron Aurbach. "Surface films phenomena on vanadium-pentoxide cathodes for Li and Li-ion batteries: in situ AFM imaging". In: *Electrochemistry Communications* 6.6 (2004), pp. 536–542. ISSN: 13882481. DOI: 10.1016/j.elecom.2004.03.014. URL: http://www.sciencedirect.com/science/article/pii/S1388248104000669.

[82] Robert Kostecki and Frank McLarnon. "Nanometer-scale electrochemical lithography on the spinel oxide LiMn[sub 2]O[sub 4]". In: *Applied Physics Letters* 76.18 (2000), p. 2535. ISSN: 00036951. DOI: 10.1063/1.126400. URL: http://scitation.aip.org/content/aip/journal/apl/76/18/10.1063/1.126400http://link.aip.org/link/APPLAB/v76/i18/p2535/s1{\&}Agg=doi.

[83] F. Kong et al. "In situ studies of SEI formation". In: *Journal of Power Sources* 97-98 (2001), pp. 58–66. ISSN: 03787753. DOI: 10.1016/S0378-7753(01)00588-2. URL: http://www.sciencedirect.com/science/article/pii/S0378775301005882.

[84] Y. Matsuo, Robert Kostecki, and F. McLarnon. "Surface Layer Formation on Thin-Film LiMn[sub 2]O[sub 4] Electrodes at Elevated Temperatures". In: *Journal of The Electrochemical Society* 148.7 (2001), A687. ISSN: 00134651. DOI: 10.1149/1.1373658. URL: http://jes.ecsdl.org/cgi/doi/10.1149/1.1373658.

[85] Ivan T. Lucas, Elad Pollak, and Robert Kostecki. "In situ AFM studies of SEI formation at a Sn electrode". In: *Electrochemistry Communications* 11.11 (2009), pp. 2157–2160. ISSN: 13882481. DOI: 10.1016/j.elecom.2009.09.019. URL: http://www.sciencedirect.com/science/article/pii/S1388248109004561.

[86] Dario Alliata et al. "Electrochemical SPM investigation of the solid electrolyte interphase film formed on HOPG electrodes". In: *Electrochemistry Communications* 2.6 (2000), pp. 436–440. ISSN: 13882481. DOI: 10.1016/S1388-2481(00)00056-4. URL: http://www.sciencedirect.com/science/article/pii/S1388248100000564.

[87] Dario Alliata et al. "Anion intercalation into highly oriented pyrolytic graphite studied by electrochemical atomic force microscopy". In: *Electrochemistry Communications* 1.1 (1999), pp. 5–9. ISSN: 13882481. DOI: 10.1016/S1388-2481(98)00005-8. URL: http://www.sciencedirect.com/science/article/pii/S1388248198000058.

[88] F.P. Campana et al. "In situ atomic force microscopy study of dimensional changes during Li+ ion intercalation/de-intercalation in highly oriented pyrolytic graphite". In: *Electrochemistry Communications* 7.1 (2005), pp. 107–112. ISSN: 13882481. DOI: 10.1016/j.elecom.2004.11.015. URL: http://www.sciencedirect.com/science/article/pii/S1388248104003091.

[89] F.P. Campana et al. "In situ atomic force microscopy study of exfoliation phenomena on graphite basal planes". In: *Electrochemistry Communications* 10.10 (2008), pp. 1590–1593. ISSN: 13882481. DOI: 10.1016/j.elecom.2008.08.026. URL: http://www.sciencedirect.com/science/article/pii/S1388248108003913.

[90] L. Y. Beaulieu et al. "Colossal Reversible Volume Changes in Lithium Alloys". In: *Electrochemical and Solid-State Letters* 4.9 (2001), A137. ISSN: 10990062. DOI: 10.1149/1.1388178.

[91] L. Y. Beaulieu et al. "A system for performing simultaneous in situ atomic force microscopy/optical microscopy measurements on electrode materials for lithium-ion batteries". In: *Review of Scientific Instruments* 72.8 (2001), pp. 3313–3319. ISSN: 00346748. DOI: 10.1063/1.1388214.

[92] L. Y. Beaulieu et al. "The Electrochemical Reaction of Lithium with Tin Studied By In Situ AFM". In: *Journal of The Electrochemical Society* 150.4 (2003), A419. ISSN: 00134651. DOI: 10.1149/1.1556595.

[93] L. Y. Beaulieu et al. "Reaction of Li with Alloy Thin Films Studied by In Situ AFM". In: *Journal of The Electrochemical Society* 150.11 (2003), A1457. ISSN: 00134651. DOI: 10.1149/1.1613668.

[94] Xiaojian Zhu et al. "Direct observation of lithium-ion transport under an electrical field in LixCoO2 nanograins." en. In: *Scientific reports* 3 (2013), p. 1084. ISSN: 2045-2322. DOI: 10.1038/srep01084. URL: http://www.nature.com/srep/2013/130117/srep01084/full/srep01084.html.

[95] Sanjay Ramdon and Bharat Bhushan. "Nanomechanical characterization and mechanical integrity of unaged and aged Li-ion battery cathodes". In: *Journal of Power Sources* 246 (2014), pp. 219–224. ISSN: 03787753. DOI: 10.1016/j.jpowsour.2013.07.078. URL: http://www.sciencedirect.com/science/article/pii/S037877531301269X.

[96] Mitsunori Kitta, Masanori Kohyama, and Hiroshi Onishi. "True atomic-scale imaging of a spinel Li4Ti5O12(111) surface in aqueous solution by frequency-modulation atomic force microscopy". In: *Applied Physics Letters* 105.11 (2014), p. 111606. ISSN: 0003-6951. DOI: 10.1063/1.4896137. URL: http://scitation.aip.org/content/aip/journal/apl/105/11/10.1063/1.4896137.

[97] Sergei V. Kalinin and Anna N. Morozovska. "Electrochemical strain microscopy of local electrochemical processes in solids: mechanism of imaging and spectroscopy in the diffusion limit". In: *Journal of Electroceramics* 32.1 (2013), pp. 51–59. ISSN: 1385-3449. DOI: 10.1007/s10832-013-9819-7. URL: http://link.springer.com/10.1007/s10832-013-9819-7.

[98] Nina Balke et al. "Decoupling electrochemical reaction and diffusion processes in ionically-conductive solids on the nanometer scale." In: *ACS Nano* 4.12 (2010), pp. 7349–57. ISSN: 1936-086X. DOI: 10.1021/nn101502x. URL: http://dx.doi.org/10.1021/nn101502x.

[99] Qian Nataly Chen et al. "Delineating local electromigration for nanoscale probing of lithium ion intercalation and extraction by electrochemical strain microscopy". In: *Applied Physics Letters* 101.6 (2012), p. 063901. ISSN: 00036951. DOI: 10.1063/1.4742933. URL: http://scitation.aip.org/content/aip/journal/apl/101/6/10.1063/1.4742933.

[100] Hugues-Yanis Amanieu et al. "Electrochemical strain microscopy time spectroscopy: Model and experiment on LiMn2O4". In: *Journal of Applied Physics* 118.5 (2015), p. 055101. ISSN: 0021-8979. DOI: 10.1063/1.4927747. URL: http://scitation.aip.org/content/aip/journal/jap/118/5/10.1063/1.4927747.

[101] Sergey Yu. Luchkin et al. "Li transport in fresh and aged LiMn2O4 cathodes via electrochemical strain microscopy". In: *Journal of Applied Physics* 118.7 (2015), p. 072016. ISSN: 0021-8979. DOI: 10.1063/1.4927816. URL: http://scitation.aip.org/content/aip/journal/jap/118/7/10.1063/1.4927816.

[102] Ahmadreza Eshghinejad et al. "Scanning thermo-ionic microscopy for probing local electrochemistry at the nanoscale". In: *Journal of Applied Physics* 119.20 (2016), p. 205110. ISSN: 0021-8979. DOI: 10.1063/1.4949473. URL: http://scitation.aip.org/content/aip/journal/jap/119/20/10.1063/1.4949473.

[103] A. J. McQuillan, P. J. Hendra, and M. Fleischmann. "Raman spectroscopic investigation of silver electrodes". In: *Journal of Electroanalytical Chemistry* 65.2 (1975), pp. 933–944. ISSN: 03681874. DOI: 10.1016/0368-1874(75)85167-7. URL: http://linkinghub.elsevier.com/retrieve/pii/0368187475851677.

[104] Raoul M. Stöckle et al. "Nanoscale chemical analysis by tip-enhanced Raman spectroscopy". In: *Chemical Physics Letters* 318.1-3 (2000), pp. 131–136. ISSN: 00092614. DOI: 10.1016/S0009-2614(99)01451-7. URL: http://linkinghub.elsevier.com/retrieve/pii/S0009261499014517.

[105] M. A. Young, J. A. Dieringer, and R. P. Van Duyne. "Plasmonic Materials for Surface-Enhanced and Tip-Enhanced Raman Spectroscopy". In: *Tip Enhancement*. 2007. Chap. 1, pp. 1–39. ISBN: 9780444520586. DOI: 10.1016/B978-044452058-6/50002-5. URL: http://www.sciencedirect.com/science/article/pii/B9780444520586500025.

[106] Ann-Lauriene Haag. "Potential-Driven Surface Stress of a Cantilever-Based Sensor". Ph.D. McGill University, 2016.

[107] R Shuttleworth. "The Surface Tension of Solids". In: *Proceedings of the Physical Society. Section A* 63.5 (1950), pp. 444–457. ISSN: 0370-1298. DOI: 10.1088/0370-1298/63/5/302. URL: http://stacks.iop.org/0370-1298/63/i=5/a=302?key=crossref.a7d9b3331d8e1a0eadff29036c89607d.

[108] Lasse Makkonen. "Misinterpretation of the Shuttleworth equation". In: *Scripta Materialia* 66.9 (2012), pp. 627–629. ISSN: 13596462. DOI: 10.1016/j.scriptamat.2012.01.055. URL: http://linkinghub.elsevier.com/retrieve/pii/S1359646212000826.

[109] Dominik Kramer. "Dependence of surface stress, surface energy and surface tension on potential and charge". In: *Physical chemistry chemical physics* 10.1 (2008), pp. 168–177. ISSN: 1463-9076. DOI: 10.1039/B710065E. URL: http://xlink.rsc.org/?DOI=B710065E.

[110] G Gerald Stoney. "The Tension of Metallic Films Deposited by Electrolysis". In: *Proceedings of the Royal Society of London. Series A, Containing Papers of a Mathematical and Physical Character* 82.553 (1909), pp. 172–175. ISSN: 09501207. URL: http://www.jstor.org/stable/92886.

[111] J. P. Cleveland et al. "A nondestructive method for determining the spring constant of cantilevers for scanning force microscopy". In: *Review of Scientific Instruments* 64.2 (1993), pp. 403–405. ISSN: 0034-6748. DOI: 10.1063/1.1144209. URL: http://aip.scitation.org/doi/10.1063/1.1144209.

[112] M. N. Obrovac and V. L. Chevrier. "Alloy Negative Electrodes for Li-Ion Batteries M.N. Obrovac". In: *Chemical Reviews* 114.23 (2014), pp. 11444–11502. ISSN: 0009-2665. DOI: 10.1021/cr500207g. URL: http://pubs.acs.org/doi/abs/10.1021/cr500207g.

[113] T. R. Ferguson and M. Z. Bazant. "Nonequilibrium Thermodynamics of Porous Electrodes". In: *Journal of the Electrochemical Society* 159.12 (2012), A1967–A1985. ISSN: 0013-4651. DOI: 10.1149/2.048212jes. URL: http://jes.ecsdl.org/cgi/doi/10.1149/2.048212jes.

[114] K Zaghib et al. "Electronic, Optical, and Magnetic Properties of LiFePO4: Small Magnetic Polaron Effects". In: (2007). DOI: 10.1021/CM0710296. URL: http://pubs.acs.org/doi/abs/10.1021/cm0710296.

[115] Aaron Mascaro et al. "Measuring Spatially Resolved Collective Ionic Transport on Lithium Battery Cathodes Using Atomic Force Microscopy". In: *Nano Letters* 17.7 (2017), pp. 4489–4496. ISSN: 1530-6984. DOI: 10.1021/acs.nanolett.7b01857. URL: http://pubs.acs.org/doi/abs/10.1021/acs.nanolett.7b01857.

[116] Andrea Paolella et al. "Etched Colloidal LiFePO4 Nanoplatelets toward High-Rate Capable Li-Ion Battery Electrodes". In: *Nano letters* 14.12 (2014), pp. 6828–6835. URL: http://pubs.acs.org.proxy3.library.mcgill.ca/doi/abs/10.1021/nl504093w.

[117] D J Oliver et al. "One-to-one spatially matched experiment and atomistic simulations of nanometre-scale indentation". In: *Nanotechnology* 25.2 (2014), p. 025701. ISSN: 0957-4484. DOI: 10.1088/0957-4484/25/2/025701. URL: http://stacks.iop.org/0957-4484/25/i=2/a=025701?key=crossref.f39c9528f76a36d4dbb9c55cc31595d0.

[118] Mayumi Maeda, Henry S. White, and D.J. McClure. "Electrochemical behavior and surface structure of Pt thin film electrodes deposited on molecularly smooth mica". In: *Journal of Electroanalytical Chemistry and Interfacial Electrochemistry* 200.1-2 (1986), pp. 383–387. ISSN: 00220728. DOI: 10.1016/0022-0728(86)90072-0. URL: http://linkinghub.elsevier.com/retrieve/pii/0022072886900720.

[119] Alexandre Ponrouch and M. Rosa Palacín. "On the impact of the slurry mixing procedure in the electrochemical performance of composite electrodes for Li-ion batteries: A case study for mesocarbon microbeads (MCMB) graphite and Co3O4". In: *Journal of Power Sources* 196.22 (2011), pp. 9682–9688. ISSN: 03787753. DOI: 10.1016/j.jpowsour.2011.07.045. URL: http://linkinghub.elsevier.com/retrieve/pii/S0378775311013838.

[120] Yong-gang Wang et al. "Hybrid Aqueous Energy Storage Cells Using Activated Carbon and Lithium-Ion Intercalated Compounds". In: *Journal of The Electrochemical Society* 153.8 (2006), A1425. ISSN: 00134651. DOI: 10.1149/1.2203772. URL: http://jes.ecsdl.org/cgi/doi/10.1149/1.2203772.

[121] Yong-gang Wang and Yong-yao Xia. "Hybrid Aqueous Energy Storage Cells Using Activated Carbon and Lithium-Intercalated Compounds". In: *Journal of The Electrochemical Society* 153.2 (2006), A450. ISSN: 00134651. DOI: 10.1149/1.2140678. URL: http://jes.ecsdl.org/cgi/doi/10.1149/1.2140678.

[122] Tyler Enright. "Design and application of combined AFM-SICM for the investigation of lithium charging events". M.Sc. McGill University, 2014.

[123] Shengyi Li and Benjamin C. Church. "Electrochemical stability of aluminum current collector in aqueous rechargeable lithium-ion battery electrolytes". In: *Journal of Applied Electrochemistry* 47 (2017), pp. 839–853. DOI: 10.1007/s10800-017-1081-2. URL: https://link.springer.com/content/pdf/10.1007/s10800-017-1081-2.pdf.